

Nanoscale Control of Gap-plasmon Enhanced Optical Processes

2015

Chatdanai Lumdee
University of Central Florida

Find similar works at: <http://stars.library.ucf.edu/etd>

University of Central Florida Libraries <http://library.ucf.edu>

STARS Citation

Lumdee, Chatdanai, "Nanoscale Control of Gap-plasmon Enhanced Optical Processes" (2015). *Electronic Theses and Dissertations*. Paper 1385.

This Doctoral Dissertation (Open Access) is brought to you for free and open access by STARS. It has been accepted for inclusion in Electronic Theses and Dissertations by an authorized administrator of STARS. For more information, please contact lee.dotson@ucf.edu.

**NANOSCALE CONTROL OF GAP-PLASMON ENHANCED
OPTICAL PROCESSES**

by

CHATDANAI LUMDEE
B.E. Chulalongkorn University, Thailand, 2010

A dissertation submitted in partial fulfillment of the requirements
for the degree of Doctor of Philosophy
in College of Optics and Photonics, CREOL,
at the University of Central Florida
Orlando, Florida

Fall Term
2015

Major Professor: Pieter G. Kik

© 2015 Chatdanai Lumdee

ABSTRACT

Surface plasmon resonances of metal nanostructures have been studied intensely in recent years. The strong plasmon-mediated electric field enhancement and field confinement well beyond the diffraction limit has been demonstrated to improve the performance of optical devices including ultrasensitive sensors, light emitters, and optical absorbers. A plasmon resonance mode of particular recent interest is the *gap plasmon* resonance that occurs on closely spaced metallic structures. In contrast to plasmon resonances supported by isolated metal nanostructures, coupled nanostructures provide additional spectral and spatial control over the plasmon resonance response. For example, the resonance frequencies of metal nanoparticle dimers depend strongly on the gap size between the nanoparticles. Gap plasmons can produce local electric field enhancement factors that are several orders of magnitude stronger and more confined than surface plasmon resonances of isolated plasmonic nanospheres. The reliance of gap plasmons on few-nanometer separation between nanostructures makes it difficult to prepare gap-plasmon supporting structures with predictable resonance frequency and field enhancement. A structure that avoids this challenge is the film-coupled nanoparticle (NP). Similar to nanoparticle dimers, a nanoparticle on a supporting metallic film (or NP-on-a-mirror) can offer a strong coupling between the particle and its local environment, in this case the supporting film instead of adjacent nanoparticles, enabling strongly confined gap-plasmon modes. The NP-on-a-mirror geometry has been shown to produce reproducible gap plasmon resonances in a chemically and thermally robust, easy to fabricate structure.

In this Thesis, we first present a scheme for controlling the gap plasmon resonance frequency of single gold nanoparticles using aluminum oxide coated metal films. We demonstrate experimentally and numerically that the gap-plasmon resonance of single gold nanoparticles can be tuned throughout the visible range by controlling the aluminum oxide thickness via anodization. In a separate study of Au NP on Al₂O₃ coated gold films it is shown that the oxide coating improves the stability of the structure under intense laser irradiation. An combined experimental and numerical analysis of the spectral response of Au NP on rough Au films shows that a film roughness of a few nanometer can affect the gap plasmon resonance in the absence of an oxide spacer layer. A photoluminescence study of single gold nanoparticles on an Al₂O₃ coated gold film shows that the gap-plasmon resonance of this type of plasmonic structure can increase gold photoluminescence by more than four orders of magnitude. Related numerical simulations reveal that the local photoluminescence enhancement of a gold nanoparticle on an Al₂O₃ coated gold film can be as high as one million near the particle-film junction. Finally, a new plasmonic sensing element was proposed based on our findings in the previous chapters. This proposed *hole-in-one* structure offers several attractive features including an easily optically accessible gap plasmon mode, while maintaining a relatively simple fabrication method.

Taken together, the research presented in this Thesis demonstrates how the resonance frequency, field enhancement, mode polarization, structural stability, and structure reliability can be controlled at the nanoscale. The knowledge gained in the course of this work could lead to further development of nanophotonic devices that utilize extremely confined optical fields and precisely controlled resonance frequencies.

ACKNOWLEDGMENTS

First of all I would like to express my utmost gratitude to the most influential person in my PhD study, the person who has not only been my academic advisor but also a great mentor and a role model I look up to, Dr. Pieter G. Kik. I am very fortunate that he accepted me to join his NanoPhotonics and Near-field Optics Group when I first got into CREOL in Fall 2010. Since then I have gotten involved in many interesting nanophotonic research projects. Above all, I am deeply thankful for his incredible patience. He had taught me everything from operating equipment in the lab, looking at data with a critical eye, preparing manuscripts, and many others which I cannot list all here. In addition, his enthusiasm and encouragement help support me in many occasions to complete the projects without losing spirit. It is all thanks to him that I have grown as a scientist.

I would like to acknowledge my dissertation committee members, Dr. Aristide Dogariu, Dr. Qun Huo, and Dr. Stephen Kuebler. Their questions, comments, feedback, and encouragement are highly appreciated.

In addition, I would like to thank my friends and colleagues in the NanoPhotonics and Near-field Optics Group. Special thank goes to Dr. Seyfollah Toroghi whom I spend the most of my PhD time with in our office. I am thankful for him taking his time teaching me techniques and tricks related to numerical simulations, and for sharing his wisdom in both the scientific world and in life. I would also like to thank Dr. Binfeng Yun and Yu-Wei Lin who worked in the group during my time at CREOL. They both shared their knowledge in several aspects of science, especially Dr. Yun who helped me set up experiments and co-authored three of my peer-reviewed articles. I would also like to send an additional note to thank Yu-Wei for recommending me where

to find tasty food in the area and for keeping in touch after he graduated. Additionally, I would like to thank the alumni who were here before I joined the team, but who have directly and indirectly contributed to my research success. Special thanks to Dr. Oleksandr Savchyn for teaching me about research and the equipment in our labs during his last few months in the group, and Dr. Amitabh Ghoshal and Dr. Min Hu for their work that served as the foundation of my projects.

I also would like to thank Dr. Beatriz Roldan Cuenya and her students, Dr. Farzad Behafarid, Mahdi Ahmadi, and Hemma Mistry for their help in characterizing several of our samples, for the discussions on their interesting projects, and for giving me the opportunity to shortly join their team to conduct an experiment at Brookhaven National Laboratory.

I am also thankful to CREOL faculty and staff members for their support in both academic and administrative aspects. The combination has made my life at CREOL a wonderful experience. Special thanks to Erdem Erden, Kumel Kagawala, Esat Kondakci, Matthew Mills, and Ali Miri for countless times of letting me to stay in their offices for a long conversation, or sometimes just relaxing.

I am grateful to have friends who we share interests and spend time having fun and doing recreational activities together. Among those, I would like to thank the Badminton Club and Thai Student Association at the University of Central Florida, and Thai Student Association at the University of Florida.

To close this section, I would like to send my deepest gratitude to my family. Without them, I would not be where I am.

TABLE OF CONTENTS

LIST OF FIGURES	xi
1. INTRODUCTION	1
1.1. Theory: Plasmon Resonance, Field Enhancement, Scattering and Absorption	1
1.2. Surface Plasmon Resonance Tuning.....	5
1.3. Applications of Localized Surface Plasmons	14
1.4. This Thesis	19
2. POST-FABRICATION VOLTAGE CONTROLLED RESONANCE TUNING OF NANOSCALE PLASMONIC ANTENNAS.....	22
2.1. Introduction.....	22
2.2. Experiment and Simulation.....	24
2.3. Results and Discussion	26
2.4. Summary	37
3. WIDE-BAND SPECTRAL CONTROL OF GOLD NANOPARTICLE PLASMON RESONANCES ON THERMALLY AND CHEMICALLY ROBUST SENSING PLATFORM	39
3.1. Introduction.....	39
3.2. Experiment and Simulation.....	41
3.3. Results and Discussion	44
3.4. Summary	59

4. EFFECT OF SURFACE ROUGHNESS ON SUBSTRATE-TUNED GOLD NANOPARTICLE GAP PLASMON RESONANCES.....	60
4.1. Introduction.....	60
4.2. Experiment and Simulation.....	61
4.3. Results and Discussion	63
4.4. Summary	73
5. GAP-PLASMON ENHANCED GOLD NANOPARTICLE PHOTOLUMINESCENCE	74
5.1. Introduction.....	74
5.2. Experiment and Simulation.....	76
5.3. Results and Discussion	79
5.4. Summary	93
6. NORMAL INCIDENCE EXCITATION OF SIDEWALL GAP-PLASMONS ON GOLD NANOPARTICLES IN A CYLINDRICAL NANOHOLE	94
6.1. Introduction.....	94
6.2. Experiment and Simulation.....	99
6.3. Results and Discussion	102
6.4. Summary	113
7. SUMMARY AND OUTLOOK.....	115
APPENDIX A: SUPPORTING INFORMATION FOR CHAPTER 2	118
A.1. Spectral Measurements	119
A.2. Particle Size Variation	120
APPENDIX B: SUPPORTING INFORMATION FOR CHAPTER 3	123

B.1. Conversion of Hyperspectral Images to False-color RGB Representation.....	124
B.2. Simulation of Single-particle Scattering Spectra and Electric Field Distributions.....	125
B.3. Laser Spot Size Determination using Nanoparticle-mediated Beam Sampling.....	128
APPENDIX C: SUPPORTING INFORMATION FOR CHAPTER 5	130
C.1. Scattering Spectrum from Different Gold Nanoparticles.....	131
C.2. Spectral Shape of the Particle-related Photoluminescence	132
C.3. Photoluminescence Enhancement Spectrum from Different Gold Nanoparticles	133
APPENDIX D: SUPPORTING INFORMATION FOR CHAPTER 6	135
D.1. Microscopy Images from Different Steps of Sample Preparation	136
D.2. Darkfield and SEM Images, Scattering Spectra, and Transmission Spectra of Additional HiO Structures	137
APPENDIX E: LIST OF PUBLICATIONS	141
REFERENCES	143

LIST OF FIGURES

Figure 1-1: Simplified model for the electric field calculation inside and around a metal nanoparticle	2
Figure 1-2: Electric field enhancement inside (a) a nanosphere made of different metals in air and (b) a gold nanosphere in different host media. (c) Dielectric functions of four metals from Ref. [4].	7
Figure 1-3: Near-field coupling between metal nanoparticles in a nanoparticle array at the resonance conditions under two incident electric field polarizations, (a) the incident electric field is perpendicular to the nanoparticle array resulting in a blue-shift and (b) the incident electric field is parallel to the particle chain resulting in a red-shift.....	10
Figure 1-4: Simulated distribution of the electric field enhancement factor at the resonance frequency in air of (a) a 60 nm diameter gold nanoparticle on an aluminum film with a 4 nm Al_2O_3 coating and (b) two gold nanoparticles separated by a distance of 4 nm.	14
Figure 2-1: Darkfield microscopy images of 60 nm diameter gold nanoparticles on an Al substrate prior anodization (a) and (b), and after anodization at different voltages (c) to (e). Scanning electron microscopy images of Au nanoparticles before (f) and after (g) anodization.	28
Figure 2-2: (a) Scattering spectra from a single Au nanoparticle for different anodization voltages. The corresponding oxide thicknesses are shown in parentheses. The inset shows the measured Al_2O_3 thickness as a function of anodization voltage. The sample structure is shown schematically. (b) Calculated scattering spectra of 60 nm Au nanoparticles on an Al_2O_3 coated	

aluminum film as a function of Al_2O_3 thickness d corresponding to the thickness values in panel (a). The sample structure is shown schematically. 30

Figure 2-3: (a) Measured z-polarized plasmon resonance wavelength and (b) the corresponding peak scattering signal of 60 nm diameter Au nanoparticles on an oxidized Al film as a function of Al_2O_3 thickness. The lines represent the results from numerical simulations. The error bars on the simulated data represent predicted signal variation due to the known colloid size dispersion. 33

Figure 2-4: Schematic representation of (a) darkfield illumination of a supported Au nanoparticle on an oxidized aluminum film, (b) the particle polarization and image charge distribution resulting from x-polarized excitation and (c) from z-polarized excitation, and (d) a color image of the observed dark-field microscopy image of a Au particle on the native oxide layer on the Al film 35

Figure 3-1: (a)-(e) Real-color dark-field microscopy images of gold nanoparticles on gold substrates with Al_2O_3 coating thickness 0, 1.3, 1.5, 2.2, and 3.4 nm, respectively. (f)-(j) False-color images of these same nanoparticles obtained using a hyperspectral camera taken in the range 500 - 800 nm. The color bar shows the wavelength representation used in figures (f)-(j). 46

Figure 3-2: (a)-(e) Measured scattering spectra from single gold nanoparticles on gold substrates without an Al_2O_3 spacer layer and with 1.3, 1.5, 2.2, and 3.4 nm Al_2O_3 spacer layer, respectively. The shaded region on each plot represents the confidence intervals of the measurement and the black curve shows a typical scattering spectrum. The green arrow indicates the plasmon resonance wavelength of gold nanoparticles in colloidal solution. The insets in (a) show spectral images obtained from the same particle by collecting wavelength bands

545 - 555 nm and 695 - 705 nm. (f)-(j) Calculated scattering spectra of 60 nm gold nanoparticles on gold films coated with 0 nm, 1.5 nm, 2 nm, 3 nm, and 4 nm of Al_2O_3 , respectively. The blue curves in (f)-(j) show the simulated scattering spectrum assuming the presence of a 0.75 nm thick organic coating on the gold nanoparticle..... 49

Figure 3-3: Calculated scattering spectrum of a 60 nm diameter Au nanoparticle coated with a 0.75 nm thick organic layer on a gold film. Insets show corresponding electric field snapshots at 550 nm and 690 nm under TE and TM illumination respectively, shown on the same relative scale..... 52

Figure 3-4: Measured and simulated scattering peak wavelength (a) and peak intensity (b) of single gold nanoparticles on a gold film with different Al_2O_3 coating thicknesses. 53

Figure 3-5: (a)-(e) Normalized scattering spectra of single gold nanoparticles on gold films coated with 0 nm, 1.3 nm, 1.5 nm, 2.2 nm, and 3.4 nm Al_2O_3 layers, respectively. The red and black curves represent the spectra before and after one minute of laser illumination at $\sim 100 \text{ W/mm}^2$, respectively. (f)-(j) Calculated scattering spectra of gold nanoparticles with (black line) and without (red line) a 0.1 nm organic shell on gold films with 0 nm, 1.5 nm, 2 nm, 3 nm, and 4 nm Al_2O_3 coating, respectively. The black and red dashed lines in (f) correspond to the same particle with a 0.6 nm and 0.5 nm organic coating, respectively..... 55

Figure 4-1: (a) A darkfield microscopy image of gold nanoparticles on a gold film. The insets show a magnified view of two representative particles. (b) Peak-normalized single particle scattering spectra from randomly selected gold nanoparticles. 64

Figure 4-2: (a) AFM image of a gold film thermally evaporated on glass. (b) Example surface geometry near a liquid-deposited gold nanoparticle deposited on top of the surface shown in (a). (c) Normalized gap size histogram from over 1,200 possible particle locations. 66

Figure 4-3: Schematic of a representative simulation geometry and relevant parameters showing (a) a top view without a gold nanoparticle showing three protrusions, (b) a side view along the dashed line in (a) with a deposited gold nanoparticle present, and (c) a perspective view of the final structure. 68

Figure 4-4: Normalized scattering spectra of a gold nanoparticle (a) on a flat gold film and (b) on a corrugated gold surface with $d = 0$ (dashed line) and $d = 0.39$ nm (solid line). The field-plots show two-dimensional electric field distributions at the main resonance peak of the spectra as indicated by the green arrows. 70

Figure 4-5: (a) Contour graph of the scattering spectra of gold nanoparticles with different sizes on a flat gold film. (b) Contour graph of the scattering spectra of an 80 nm diameter gold nanoparticle on a rough surface as a function of air gap size d . The black dashed line represents the average resonance energy from the experiment and the two grey dashed lines span 2σ on each side. The black squares mark the main peak positions and the solid lines show empirical fits to the peak position. The blue circles represent experimentally expected spectral positions and variations based on numerical simulations. 72

Figure 5-1: (a) Dark field microscopy image of 80 nm diameter gold nanoparticles on an Al_2O_3 coated gold film. (b and c) Measured and simulated scattering spectra of the gold

nanoparticle highlighted in (a). (d and e) The simulated distribution of the electric field magnitude under illumination at respectively 550 nm and at 652 nm TM at an angle of incidence of 77°... 81

Figure 5-2: (a) The experimental configuration for single-particle photoluminescence spectroscopy. (b and c) Snapshots of the simulated electric field distributions respectively under 532 nm and at 633 nm excitation at a 35° angle of incidence. 83

Figure 5-3: Photoluminescence spectra collected under 532 nm excitation (a) and 633 nm excitation (b) from areas containing a gold nanoparticle (bright green and bright red lines) and no gold nanoparticle (dark green and dark red lines). The insets schematically show that a gold nanoparticle adds PL signal at the particle resonance wavelength (red arrows) to the weak background PL. 85

Figure 5-4: The measured (a) and calculated (b) photoluminescence enhancement spectra g_{PL} for a gold nanoparticle excited with 532 nm (green solid lines) and 633 nm (red solid lines) laser lines. The black dashed lines show the measured and calculated peak-normalized scattering spectra of the particle. 87

Figure 5-5: (a and c) Measured scattering and photoluminescence spectra of a film-coupled gold nanoparticle. The dashed green lines mark the photon energy corresponding to 532 nm excitation. The horizontal red arrows indicate the gap plasmon resonance energy. (b) The Au band structure around the X point near the Fermi level, adapted from Ref. [172]. The vertical green and red arrows show $e-h$ excitation at 532 nm followed by plasmon enhanced recombination at an $e-h$ energy separation that matches the gap plasmon resonance energy. 90

Figure 6-1: (a) Illustration of a HiO structure consisting of a Au NP inside a NH in an Al film on a glass substrate with the NP touching the oxidized Al sidewall. Analyte molecules (purple ellipsoids) can diffuse to the gap-plasmon resonance hot-spot (orange) close to the Al surface where they can be detected. (b) Fabrication process of the HiO structures using nanosphere lithography. (c and d) SEM images of two HiO structures, taken at a stage angle of 45° and at normal incidence respectively. The scale bar in the SEM images represents 100 nm. 98

Figure 6-2: (a) Darkfield microscopy images of a representative sample region after nanosphere lithography (a) before and (b) after Au NP deposition. (c–f) SEM images of a nanohole, a Au nanoparticle, and two HiO structures, respectively. The scale bar represents 100 nm. (g) Scattering spectra of the NH, Au NP on Al, and HiO structure marked by the arrows in (b). 104

Figure 6-3: (a) Darkfield microscopy image of the NH (top), Au NP (middle), and HiO structure (bottom) from Fig. 2(b). (b) Darkfield microscopy image of the same structures but with a linear analyzer inserted in the collection path of the microscope. (c) Matching SEM image of the structures. The images in (a–c) are ~2.5 μm wide. (d) Scattering spectra of the HiO structure collected at two analyzer angles, approximately parallel and perpendicular to the symmetry axis (dashed white line) indicated respectively by the dark and light magenta double arrows in the SEM image of the HiO structure in the inset. The scale bar in the inset is 100 nm. The polar plot shows the peak scattering intensity of the HiO structure as a function of analyzer angle..... 107

Figure 6-4: (a and b) Measured and simulated transmission spectra of a HiO structure and an isolated NH. The measured spectra were obtained from the HiO structure and NH in Al marked by the magenta and green arrows in the transmission microscopy image inset. (c and d) Simulated

distribution of the electric field enhancement factor of a HiO structure under normal incidence plane wave excitation at the main resonance frequency. The field cuts correspond to (c) a plane along the surface at the height where the Au NP touches the oxidized Al sidewall and (d) a plane normal to the surface along the symmetry axis of the HiO structure. The polar plot in (b) shows the electric field enhancement factor in the NP-oxide junction region of the HiO structure as a function of excitation angle along (red curve) and normal to (blue curve) the HiO symmetry axis, and of a Au NP on an Al film (gray curve)..... 110

Figure A-1: Darkfield scattering spectra including (a) the raw signal obtained from an area containing a single nanoparticle (I_{NP}) and the raw signal collected from a nearby region without a nanoparticle (I_{REF}), (b) the peak-normalized, dark-current corrected reference spectrum (I_{IN}), and (c) the resulting single particle scattering spectrum before background correction (I_{SC}). 120

Figure A-2: Calculated scattering spectra of the gold nanoparticles with different diameters on an aluminum film with (a) 4 nm and (b) 16 nm aluminum oxide surface layer. 121

Figure A-3: Peak scattering wavelength vs. nanoparticle diameter for samples with a 4 nm and 16 nm aluminum oxide layer thickness. The dashed lines represent the anticipated experimental particle size variation. 122

Figure B-1: (a) The color response functions used to generate false-color scattering images with the corresponding color scale. (b-d) image information corresponding to the blue, green, and red color channels with adjusted brightness, respectively. (e) The final false color image based on the three color channels shown in (b-d). 125

Figure B-2: Simulation structure used to calculate single particle scattering spectra. ... 126

Figure B-3: Calculated scattering spectrum of a 60 nm diameter Au nanoparticle coated with a 0.75 nm thick organic layer on a gold film (red line) as well as the separate contributions from x-, y- and z- oriented dipole moments (green, orange, and blue curves, respectively)..... 127

Figure B-4: Rayleigh scattering signal versus nanoparticle position relative to the center of the laser spot (red squares). The blue curve represents a Gaussian fit to the measurement, showing a FWHM of 2.2 μm 129

Figure C-1: Measured single nanoparticle scattering spectra of three different gold nanoparticles on an Al₂O₃ coated Au film on glass..... 131

Figure C-2: Background subtracted photoluminescence from three gold nanoparticles showing a small offset between the peak positions of the 532 nm and 633 nm excited NP-mediated photoluminescence spectra. The spectra under 532 nm excitation were scaled to facilitate comparison with the 633 nm excited spectra..... 133

Figure C-3: Photoluminescence enhancement spectra at 532 nm and 633 nm excitation from three different gold nanoparticles on a gold film. The scattering spectrum of these particles are scaled and overlaid to facilitate comparison between scattering and photoluminescence enhancement spectra. 134

Figure D-1: (a) Fabrication process of the HiO structures using nanosphere lithography. (b) Darkfield microscopy image of the sample after fabrication step (i), showing scattering from polystyrene beads. (c and d) darkfield microscopy images taken from the same sample area after fabrication step (ii) and (iii), respectively. The Al caps in (c) were removed revealing nanoholes in (d). (e and f) Corresponding transmission microscopy images of (c and d)..... 136

Figure D-2: (a) Darkfield microscopy image of a nanohole (top), a HiO structure (middle, marked by the magenta arrow), and a Au NP (bottom). (b) Darkfield microscopy image of the same structures but with a linear analyzer inserted in the collection path of the microscope. (c) Matching SEM image of the structures. The images in (a–c) are ~2.5 μm wide. (d) Scattering spectra of the HiO structure collected at two analyzer angles, indicated respectively by the dark and light magenta double arrows in the SEM image of the HiO structure in the inset. The scale bar in the inset is 100 nm. (e) Transmission spectra of the HiO structure and a nearby nanohole... 138

Figure D-3: (a) Darkfield microscopy image of a HiO structure (top, marked by a magenta arrow), and two nanoholes. Unlike most of the HiO structures observed in the experiment, this HiO has dried near the center of the nanohole which results in a different spectral response and relatively weak polarization dependence. (b) Darkfield microscopy image of the same structures but with a linear analyzer inserted in the collection path of the microscope. (c) Matching SEM image of the structures. The images in (a–c) are ~2.5 μm wide. (d) Scattering spectra of the HiO structure collected at two analyzer angles, indicated respectively by the dark and light magenta double arrows in the SEM image of the HiO structure in the inset. The scale bar in the inset is 100 nm. (e) Transmission spectra of the HiO structure 140

1. INTRODUCTION

Localized Surface Plasmon Resonances (LSPR) of metal nanoparticles are a collective oscillation of electrons in response to the oscillatory electric field of the incoming electromagnetic wave. At the plasmon resonance frequency this electron oscillation can produce significant electric field enhancement inside and near the surface of the metal nanoparticles. Researchers have continuously studied surface plasmon resonances in order to understand, control, and make use of these enhanced electric fields. The resonance condition depends on several factors including material, shape, size, and the local environment of nanostructures. In this chapter, we introduce the fundamental background on surface plasmon resonances of metal nanoparticles, scattering and absorption coefficients, field enhancement, applications, and conclude with an outline of the content covered in this Thesis.

1.1. Theory: Plasmon Resonance, Field Enhancement, Scattering and Absorption

In order to understand plasmon resonances on metal nanoparticles, it is helpful to consider the electric field enhancement associated with plasmon resonance. The simplest model for calculating electric fields on metal nanoparticles considers an isolated spherical nanoparticle embedded in an isotropic medium under illumination with an incident plane wave. The materials are assumed non-magnetic and the size of the particle is assumed to be much smaller than the incident wavelength, resulting in a homogeneous response inside the particle. These conditions correspond to the quasi-electrostatic approximation. Figure 1.1 shows a schematic drawing of the model with a plane wave traveling in the x-direction. The parameter a , r , E_0 , $\epsilon(\omega)$, and $\epsilon_m(\omega)$ are

the nanoparticle radius, the distance from the particle center, the incident electric field, the nanoparticle dielectric function, and the medium dielectric function, respectively.

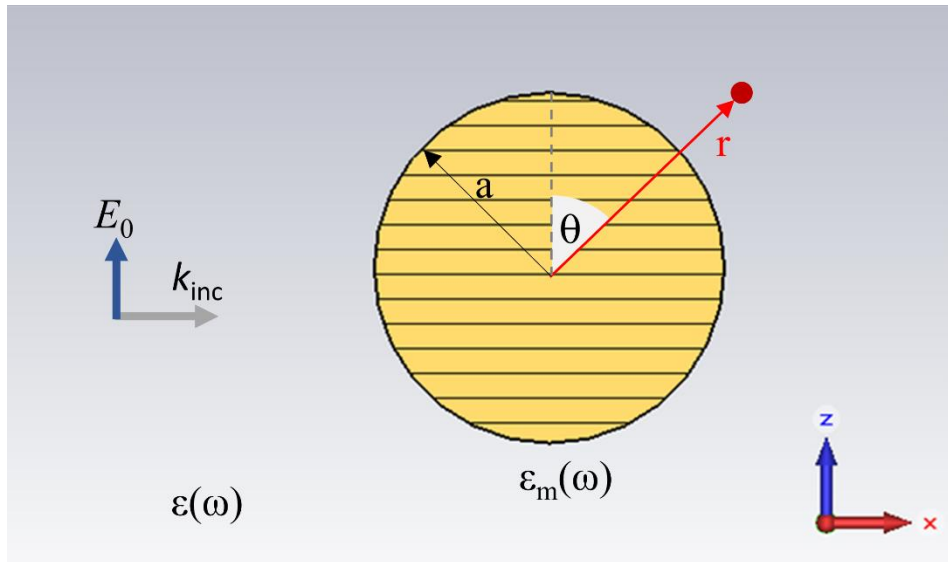


Figure 1-1: Simplified model for the electric field calculation inside and around a metal nanoparticle

When the metallic nanoparticle is exposed to an oscillatory electric field, free electrons in the particle will move and oscillate. The oscillation amplitude and the frequency response depend on the incident electric field strength and the properties of the nanoparticle. To find the resulting electric fields one must solve Laplace's equation for the system shown in Figure 1.1 with a constant E_0 in the quasi-electrostatic limit and using proper boundary conditions. The electric field far from the nanosphere $E_{r \rightarrow \infty}$ should converge to the applied field strength E_0 , the tangential electric fields should be continuous at the particle surface, i.e. $E_{t,\text{in}} = E_{t,\text{out}}$, and the normal electric displacement should be continuous at the nanosphere surface for $r = a$, i.e. $\epsilon(\omega)E_{n,\text{in}} = \epsilon_m(\omega)E_{n,\text{out}}$. These requirements result in the following internal and external potential distributions [1-3]:

$$\Phi_{in} = -\frac{3\epsilon_m(\omega)}{\epsilon(\omega) + 2\epsilon_m(\omega)} E_0 r \cos\theta \quad (1-1)$$

$$\Phi_{out} = -E_0 r \cos\theta + E_0 a^3 \frac{\epsilon(\omega) - \epsilon_m(\omega)}{\epsilon(\omega) + 2\epsilon_m(\omega)} \frac{\cos\theta}{r^2} \quad (1-2)$$

where Φ_{in} and Φ_{out} are the potential inside and outside the nanosphere, respectively. The electric fields are then acquired using $\mathbf{E} = -\nabla\Phi$,

$$\mathbf{E}_{in} = \frac{3\epsilon_m(\omega)}{\epsilon(\omega) + 2\epsilon_m(\omega)} E_0 \hat{\mathbf{z}} \quad (1-3)$$

$$\mathbf{E}_{out} = E_0 \hat{\mathbf{z}} + 3E_0 \frac{a^3}{r^3} \frac{\epsilon(\omega) - \epsilon_m(\omega)}{\epsilon(\omega) + 2\epsilon_m(\omega)} \left\{ \sin\theta \cos\phi \hat{\mathbf{x}} + \sin\theta \sin\phi \hat{\mathbf{y}} + (\cos^2\theta - 1/3) \hat{\mathbf{z}} \right\} \quad (1-4)$$

where E_0 , E_{in} , and E_{out} are the incident electric field, the electric field inside, and the electric field outside the nanosphere, respectively. The angle θ is the angle between the vector \mathbf{r} and the z-axis as shown in Figure 1.1. The angle ϕ is an angle between the projection of the vector \mathbf{r} onto the x-y plane and the x-axis. It can be seen that E_{in} and E_{out} can become much stronger than E_0 when $\epsilon(\omega) + 2\epsilon_m(\omega) \approx 0$. This condition corresponds to the resonant excitation of dipolar electron motion, and the corresponding frequency at this condition is referred to as the localized (dipolar) plasmon resonance frequency. Please note the second term in Eq. (1-4) is inversely proportional to r^3 and is the main contribution to the electric field near the surface of the nanosphere. This *near-field* contribution is very strong when r is small and gets weaker rapidly when r increases.

In order to study the plasmon resonance response of a nanostructure, a direct observation of the local electric fields around the nanostructure would be ideal. Directly probing local electric fields is not trivial. It requires accurately positioning a well-calibrated probe such as a fluorophore or Raman active molecule in the vicinity of the particle of interest and monitoring the change in the response of the probe. On the other hand, if the local electric field is known it could be used to characterize an unknown probe. This relationship would be discussed in more detail in the plasmon resonances in sensing applications section.

The simplest way to observe the plasmon resonance of a nanostructure is by monitoring its absorption or scattering coefficient. Absorbed and scattered power by a nanostructure can be calculated using the law of power conservation and the Poynting vector theorem. For a small nanosphere with the internal and external electric fields as shown in Eq. (1-3) and Eq. (1-4), the absorption and scattering efficiencies can be written as:

$$Q_{abs} = 4(k_0 n a) \text{Im} \left\{ \frac{\epsilon(\omega) - \epsilon_m(\omega)}{\epsilon(\omega) + 2\epsilon_m(\omega)} \right\} \quad (1-5)$$

$$Q_{scat} = \frac{8}{3} (k_0 n a)^4 \left| \frac{\epsilon(\omega) - \epsilon_m(\omega)}{\epsilon(\omega) + 2\epsilon_m(\omega)} \right|^2 \quad (1-6)$$

where k_0 and n are the wavenumber in vacuum and the refractive index of the surrounding medium, respectively. The two quantities represent, respectively, the ratio of the optical absorption and scattering cross-section (σ) to the physical cross-section of the nanosphere (πa^2).

It can be seen from these equations that absorption and scattering of a nanosphere are enhanced at the resonance frequency. This allows an indirect observation of plasmon resonances of metal nanostructures using a relatively simple equipment such as an optical microscope.

1.2. Surface Plasmon Resonance Tuning

The equations presented in the preceding section demonstrate that at the plasmon resonance frequency one can obtain a strong electric field enhancement near a nanostructure, defined as the ratio of the local electric field to the incident electric field e.g. E_{in}/E_0 in Eq. (1-3) and E_{out}/E_0 in Eq. (1-4). This field enhancement is useful in several areas of optics and photonics. To maximize the utility of field enhancement for a certain purpose, it is important that the plasmonic nanostructure under investigation has its resonance frequency close to the working frequency of interest. As a result, the study of controlling plasmon resonance frequencies of plasmonic nanostructures has been a very active topic of research in the scientific community. In the simplest example of a small nanosphere, the resonance frequency ω_{res} follows from the previously discussed requirement $\epsilon(\omega) + 2\epsilon_m(\omega) \rightarrow 0$. In this idealized case it is obvious that the resonance frequency will shift depending on the dielectric function of the nanosphere and of the host medium. Outside the simplifying approximations discussed above the resonance frequency can also be controlled using particle size, shape, and coupling between nanostructures, as discussed in the following sections.

1.2.1. Effect of dielectric function

As discussed above, the dielectric function of nanostructures and host media directly affects the dipolar plasmon resonance frequency of a nanostructure. To illustrate this on the basis of realistic dielectric functions, Figure 1.2(a) and Figure 1.2(b) show a plot of the electric field enhancement factors inside four metal nanospheres (aluminum, silver, gold, and copper) in air, and a plot of the electric field enhancement inside a gold nanosphere in different host media, respectively. The electric field enhancement factors are calculated using Eq. (1-3) and the dielectric function of metals are taken from literature and plotted in Figure 1.2(c) [4]. General observations in Figure 1.2(a) are that the resonance wavelength blueshifts in a nanosphere made of a material with higher plasma frequency and the resonance strength or the enhancement factor is higher when the imaginary part of the dielectric function of the material at the resonance wavelength is low. In Figure 1.2(b), it can be seen that the resonance wavelength of a gold nanosphere redshifts and the resonance strength increases when the refractive index of the host medium increases. The increase in the resonance field enhancement is due in part to the fact that the resonance wavelength moves to a wavelength where the imaginary part of gold dielectric function is lower. Based on the results in Figure 1.2 it can be seen that both the resonance wavelength and resonance strength of a nanostructure can be designed by proper selection of the particle and host materials, limited by the availability of materials with the desired dielectric function.

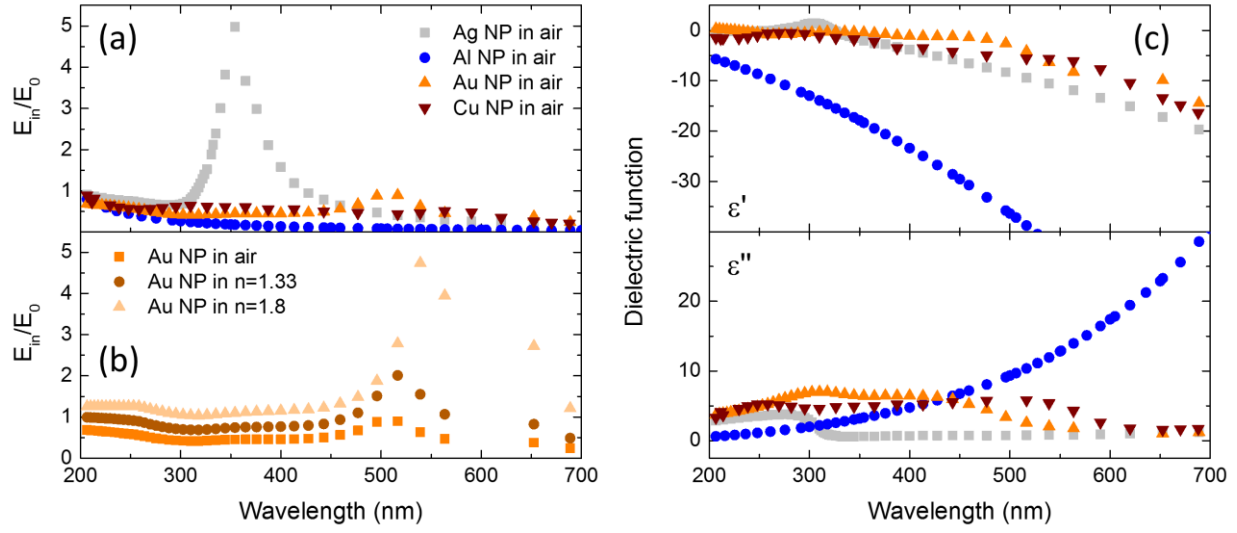


Figure 1-2: Electric field enhancement inside (a) a nanosphere made of different metals in air and (b) a gold nanosphere in different host media. (c) Dielectric functions of four metals from Ref. [4].

1.2.2. Effect of nanoparticle size and shape

The surface plasmon resonance wavelength of a metal nanostructure is sensitive to both size and shape of the particle. As previously discussed, the analytical solutions provided in Section 1.1 assume the quasi-electrostatic limit, meaning that the particle must be much smaller than the excitation wavelength and the skin depth of the material. Under these conditions all points inside the particle will respond to the field simultaneously. However as the nanoparticle gets smaller than the electron mean free path in that metal (40-50 nm for Ag and Au) [5], surface scattering has been found to introduce a significant amount of additional damping which increases the plasmon resonance linewidth. Early work in 1965 by Doremus provided experimental proof of such an

effect in small silver nanoparticles [6]. For larger nanoparticles ($a \approx \lambda_{\text{incident}}$ where $\lambda_{\text{incident}}$ is the wavelength of an incident electromagnetic wave), different parts of the particle will experience different phases of the incident electric field, making phase retardation an important parameter. The retardation will broaden the resonance linewidth. Resonance peak shifts and peak broadening of gold nanoparticle plasmon resonances were observed in size dependent studies [7]. Additionally the phase retardation also enables excitation of higher order resonance modes [8].

The shape of nanoparticles is another parameter that affects the surface plasmon resonance wavelength. For example, ellipsoidal metal nanoparticles in the quasi-static limit can show two or three plasmon resonance peaks for a spheroids and an ellipsoids, respectively. Each peak represents the response due to excitation with the electric field polarization along a principal axis of the particle [2]. Early work in this field focused on the origin of the difference between the optical properties of a metal nanoparticle and that of the bulk material. In the 1950s a model that considered the film to be a two-dimensional set of rotating ellipsoids was developed to explain the observations [9, 10]. The work by Hunderi and Myers in 1973 showed that the peak in their absorption spectrum of disordered silver films, when modeled as a film containing arrays of silver spheroids, can be understood as a superimposed effect of two peaks corresponding to the two axes of the embedded spheroids [11]. The same phenomenon has been reported in the alkali metals [12]. In 1989, a thorough analysis was performed in Na clusters, showing respectively one peak and three peaks in the absorption spectra of spherical and ellipsoidal Na clusters [13]. In 2003 Felidj *et al.* reported the plasmon resonance tuning of e-beam patterned elongated gold nanoparticles, and showed that these can provide optimum Raman enhancement at certain excitation laser wavelengths [14]. In the same year, Kuwata *et al.* reported plasmon resonance shifting in gold

nanorods showing resonance tuning into the red and near infrared regions when the size and aspect ratio of the nanorods increased [15]. In 2011, Anderson and co-workers showed a greater than 100 nm plasmon resonance tuning in gold nanobelts as the aspect ratio of the nanobelts was modified [16]. In addition, several studies on plasmon resonances of different nanostructures such as nanotriangles [17], nanocubes [18, 19], and nanoshells [20, 21] have been reported.

1.2.3. Effect of inter-particle interaction

In addition to individual nanostructures, structures consisting of more than one nanostructure unit can provide plasmon resonance changes due to near-field and far-field inter-particle interactions. Nanoparticle dimers and nanoparticle arrays have been widely studied not only because of their controllable resonance frequencies but also because of the high field enhancement factors that can be reached in the small gap between the nanoparticles [22]. These regions with high field enhancement are usually referred to as a ‘hot spots’ which can strongly amplify selected signals [23-25]. The high field enhancement is attractive for plasmon mediated sensing applications, as discussed in the following section. Plasmon resonance tuning in closely spaced nanostructure dimers and arrays is predominantly due to near-field coupling, and it depends on the direction and magnitude of external near fields from neighboring particles. In particular, near fields affect the field distribution and therefore the electron motion in neighboring particles, leading to resonance shifts. If the incident field is aligned perpendicular to the particle chains/dimers, the external electric fields from neighbors will be aligned along the internal field of the reference particle. In this case the plasmon resonance of dimers/arrays will have a blue

shifted resonance compared to the response of isolated particles. In the other scenario the plasmon resonance will undergo a redshift since the external electric fields from the neighbors will align opposite to the internal field of the reference particle [3].

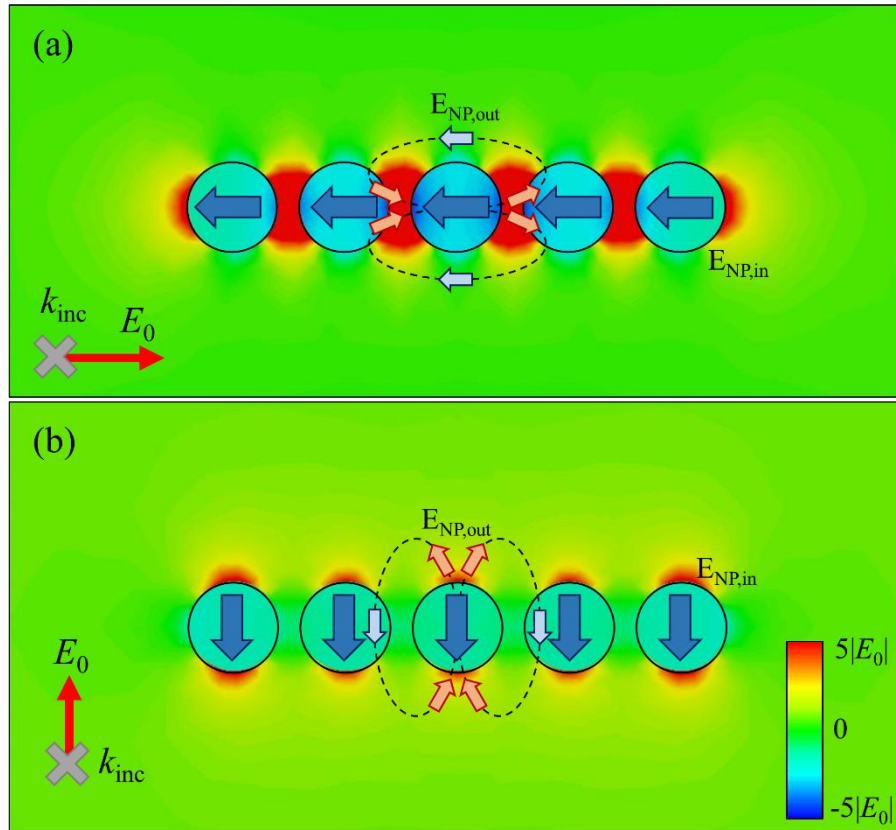


Figure 1-3: Near-field coupling between metal nanoparticles in a nanoparticle array at the resonance conditions under two incident electric field polarizations, (a) the incident electric field is perpendicular to the nanoparticle array resulting in a blue-shift and (b) the incident electric field is parallel to the particle chain resulting in a red-shift

Many numerical calculations and experiments have been reported investigating near-field mediated resonance shifts. In 2000, Aussenegg and his team reported a redshift in the resonance

wavelength in gold nanoparticle gratings with a large grating distance due to the far-field dipole interaction (Field strength \propto 1/Distance) [26]. The results agree well with theoretical work by Meier *et al.* in 1985 [27]. A report by Maier *et al.* in 2002 demonstrated two resonance shifts when the closely spaced gold particle chains were illuminated the incident field polarized along two different directions, demonstrating the importance of near-field interaction (Field strength \propto 1/Distance³) [28]. Figure 1.3 presents the distribution of electric fields of a gold nanoparticle chain consisting of five 50 nm diameter gold nanoparticles in water under two incident electric field polarizations simulated using CST Microwave Studio [29]. The field distributions show that the near-field of a gold nanoparticle can weaken or strengthen the internal electric field of neighboring particles depending on whether the polarization of the incident field is parallel or perpendicular to the particle chain axis. As a result, the resonance frequency of the structure is redshifted in Fig. 1.3(a) and is blueshifted in Fig. 1.3(b). In 2003 Zhao and co-workers reported a similar shifting behavior on silver nanoparticle arrays including two-dimensional arrays. Their study showed a blue-shift of the resonance for intermediate particle spacing (center-to-center distance > 2×diameter) and a red-shift when particles were separated by less than 2×diameter [30]. This was because neighboring fields in the perpendicular configuration (Figure 1.3(a), blue-shift) is stronger than the neighboring fields in the parallel configuration (Figure 1.3(b), red-shift) at moderate-long distance but weaker in the near field regime. Three months later Su *et al.* demonstrated a plasmon resonance redshift of gold nanoparticle dimers as the particle separation decreased [31]. In 2004 Nordlander and co-workers reported a numerical study of hybridization in nanoparticle dimers showing that the presence of two resonances modes and the fact that the resonance frequencies

shift as a function of the dimer separation could be understood as a result of mixing or hybridization of different plasmon modes [32]. These hybridized modes of the dimer were found to be either bright or dark, with the latter mode having practical implications. The interference between these two modes leads to interesting physical phenomena including plasmonic Fano-resonances [33, 34] and Electromagnetically-Induced-Transparency (EIT) [35, 36].

1.2.4. Effect of particle-substrate interaction

While coupled nanostructures such as dimers and trimers show promise in plasmon resonance control and can provide high field enhancement factors, fabricating such structures to have the desired electromagnetic coupling between closely spaced units generally involve costly and time consuming fabrication techniques such as electron beam lithography. An alternative approach is to couple a plasmonic nanostructure with a substrate. Substrate-based tuning of nanoparticle plasmon resonances makes use of the coupling between a nanoparticle and polarization change in the substrate. As a result, the need of precise alignment between nanostructures is eliminated. The plasmon resonance of substrate-controlled or ‘film-coupled’ nanoparticles can be controlled simply by depositing particles on different substrates. Several studies have reported a large resonance tuning range and strong predicted electric field confinement of film-coupled nanoparticles.

Early work in film-coupled resonance system was done by Antoniewicz in 1972 reporting a theoretical calculation showing an increase in the effective polarizability of an emitter near a metal surface [37]. A similar effect is observed when a metal nanoparticle is placed on a metal

substrate, as reported in subsequent numerical calculations [38, 39]. This effect was understood as an effect of an image charge distribution that forms in the metal substrate. In the early work, these effects could not be observed experimentally on individual metallic nanoparticles due to limitations in imaging and spectroscopy technology. In the late 1990s the optical detection of individual metallic nanoparticles using far-field optical microscopy was reported [40], demonstrating a method for the rapid study of surface plasmons on metallic nanoparticles without having to consider inhomogeneous broadening effects. Afterward, several experimental demonstrations confirmed early theoretical studies. Metal nanoparticle surface plasmons with hundreds of nanometers tuning range across the visible range were reported [41-46]. In 2003 Okamoto *et al.* reported a red-shift of approximately 200 nm of the plasmon resonance of gold nanoparticles on a gold substrate as the gap distance/particle radius decreases [47]. Similar effect was found in silver nanoparticles on a dielectric and metallic substrate which the metallic one gave a stronger response [48].

For small particle-substrate separations, the typically dipolar plasmon resonance of spherical particles is perturbed by the substrate due to a breaking of the spherical symmetry of the system, resulting in hybridized plasmon modes containing multipolar character with a maximum field amplitude near the contact point with the substrate, known as gap plasmons. Figure 1.4(a) presents the distribution of electric field enhancement of a 60 nm diameter gold nanoparticle on an aluminum film with a 4 nm Al_2O_3 coating. The structure is illuminated with a TM-polarized plane wave at a 77° angle of incidence. At the resonance frequency an electric field enhancement factor as high as 60 can be achieved at the junction between the particle and the substrate. This field enhancement factor is comparable to that of a gold nanoparticle dimer consisting of two 60

nm diameter gold nanoparticles and having the same separation distance as the Al_2O_3 thickness. The distribution of the electric field enhancement of the gold nanoparticle dimer is shown in Fig. 1.4(b). The observed gap plasmon modes are seen to be extremely confined, with lateral and surface-normal mode sizes that are similar to the gap size of the structures. Notably, these highly confined modes can be achieved in structures that can be prepared using chemically synthesized metal nanoparticles and a thin metal or dielectric layer using standard deposition techniques. This makes the preparation of film-coupled plasmon resonance structures simple, low cost, and rapid, as compared to lithography-based nanostructure fabrication.

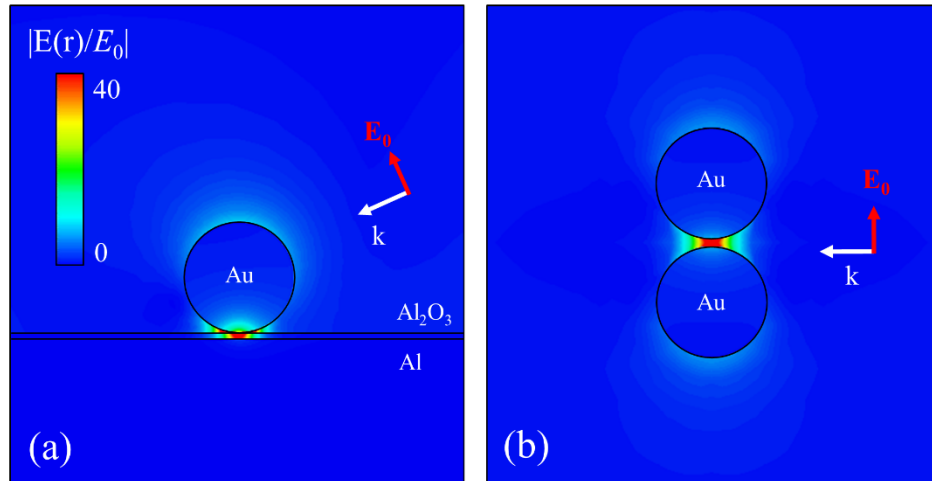


Figure 1-4: Simulated distribution of the electric field enhancement factor at the resonance frequency in air of (a) a 60 nm diameter gold nanoparticle on an aluminum film with a 4 nm Al_2O_3 coating and (b) two gold nanoparticles separated by a distance of 4 nm.

1.3. Applications of Localized Surface Plasmons

1.3.1. Sensing

Sensing is one of the most interesting applications that utilize the extreme field confinement and strong electric field enhancement factors in plasmonic nanostructures to improve the performance over their non-plasmonic counterparts. First we discuss the effect of field confinement. Because the electric field at the resonance wavelength is confined very strongly near metal nanostructures, both the resonance wavelength and resonance strength of metal nanostructures are very sensitive to small changes in the local environment. This has been demonstrated in several studies. Strong electric field enhancement factors have also been proven very useful in amplifying signal from an emitter near plasmonic nanostructures. It has been showed that plasmonic field enhancement factors can increase the emission rate of various kinds of emitters such as crystal defects [49], quantum dots [50], and fluorophores [51]. Among a wide range of studies in plasmon resonance enhanced sensing, Surface Enhanced Raman Scattering or SERS is one that has continuously drawn great attention. It has been shown that Raman scattering from single molecules can be detected using the extraordinary strong plasmonic field enhancement of metal nanoparticle aggregates [52, 53]. The first SERS observation was in 1974 when Fleischmann *et al.* reported the observation of a strong Raman signal from pyridine molecules when the molecules were adsorbed onto an anodized silver electrode [54]. Following that, the idea that enhanced Raman scattering is a result of field enhancement factors of metal nanostructures (rough metal surface) was proposed in 1977 by Jeanmaire and Van Duyne when they conducted a similar experiment [55]. Since then SERS has become a very interesting research fields since that period, catching interests from researchers in physics, chemistry, biological, and medicine [56]. Since then, numerous studies have reported SERS from several different plasmonic nanostructures. Enhanced Raman scattering using individual structures like nanospheres, nanorods, nanotriangles,

and nanocubes has been investigated. Although these structures are capable of enhancing Raman scattering from molecules, coupled nanostructures with small separation or gap provide a higher field enhancement resulting in what is referred to as a ‘hot spot’. Actually, the electric enhancement in hot spots could be the reason behinds the first SERS observation from rough silver electrodes [54]. Even though plasmon induced electric field enhancement factors in metal nanostructure aggregates can be very strong, the enhancement is typically not reproducible and varies significantly surfaces with SERS enhancement factors of 10^7 - 10^{15} have been reported [52, 57]. The difference was attributed to hot-spots that randomly formed across the substrates [58].

A better defined and likely the simplest coupled nanostructure is nanoparticle dimers. This type of coupled nanostructures, although provide only one hot spot per one dimer, can provide a high field enhancement with better reproducibility. The significant decrease in randomness allows systematically studies and proper evaluations of the performances. Early calculation attempts of the SERS enhancement factor of dimers were done in 1983. A SERS enhancement factor as high as 10^8 was predicted for silver dimers in water for 20 nm diameter nanospheres and a center-to-center distance of 21 nm [59]. Recent experimental results from nanosphere, nanodisc, nanoring, nanorod, and nanocube dimers revealed up to 10^7 in SERS enhancement factors [25, 60-62]. SERS spectra taken from a hot-spot of dimers are usually polarization dependent as expected from the anisotropic structure, producing the highest enhancement when the excitation laser is polarized along the longitudinal axis of the dimers, and if the laser wavelength matches the dimer plasmon resonance frequency [25, 63, 64]. To achieve the highest SERS enhancement factor in the dimers it is not only important to have the highest field enhancement in the hot-spot; the volume of the hot-spot also plays a role, as it determines the number of molecules that can contribute to the

signal. As a result, dimers with sharper tips do not necessarily produce higher enhancement compared to some truncated structures [62, 65]. Alternatively, film-coupled metallic nanoparticles having nanoparticles positioned on a polarizable substrate with a vertically oriented dipole also have a hot-spot in between the two nanoparticles [66]. As previously mentioned film-coupled nanoparticles are easy to prepare and produce a reliable and reproducible field enhancement, large scale plasmonic sensors or SERS substrates could be made without requiring the use of a high precision fabrication method like electron beam lithography. Several demonstrations of SERS using film-coupled nanoparticles involve self-assembly either of the Raman molecules or the nanoparticles on the substrate [66-68]. A recent study also showed that the resonance wavelength of film-coupled nanoparticle substrates can be tuned to match the excitation wavelength enabling optimization of sensing performance [69].

1.3.2. Metal photoluminescence

Photoluminescence (PL) of metal nanostructures, especially gold nanostructures, has received a lot of interest in the past few decades. Prior that time, PL of metals had not been seen as very attractive for real-world applications because of the low quantum efficiency of the emission process. The first observation of gold PL from a gold film was reported in 1969 by Mooradian where the PL of bulk gold was found to have the estimated quantum efficiency in an order of only 10^{-10} [70]. Only recently advances in nanofabrication have enabled the systematic investigation of PL from large collections of gold nanostructures and showed several orders of magnitude enhancement in the quantum efficiency over bulk gold [71-75]. Following these findings, PL of

metal nanostructures has been studied as an alternative choice to fluorescent biomarkers that might overcome challenges related to photobleaching. Following this surge of interest, PL from single gold nanoparticles was investigated. Recent studies have found that the PL spectrum of gold nanostructures closely resembles their plasmonic resonance spectrum. Several mechanisms have been proposed to explain the phenomenon but the universal explanation is still under development.

1.3.3. Hot carrier injection and photocatalysis

Plasmon induced hot carrier generation and catalysis in metal nanoparticles interacting with semiconductors/semiconductor oxides has recently received a tremendous amount of attention as a means of enhancing the efficiency of photonic devices and photocatalytic processes [76-81]. Surface plasmons have been shown to increase photon-to-hot-carrier conversion efficiencies in several research areas such as dye-sensitized solar cells [82-84], photoelectrochemical cells [85, 86], and photocatalytic reactions [87-91]. The enhancement in these processes can be attributed into three main mechanisms: plasmon enhanced power absorption in semiconductors/semiconductor oxides, plasmon induced hot carrier generation in metal nanostructures, and plasmon induced local heating [76, 92]. All three mechanisms originate from the strong electric field enhancement at the plasmon resonance condition of metal nanostructures, either in the nanostructures themselves or in nearby semiconductors/semiconductor oxides. The recent surge in the field of plasmon induced hot carrier science and plasmon enhanced catalysis seems to hold a lot of promise in utilizing plasmonic nanostructures to boost the efficiency of photonic devices and could open a new realm of applications. Gap plasmons with their extremely

high field enhancement factors and strong confinement of the internal field near the particle surface appear to be an ideally suited plasmon mode for useful hot carrier generation.

1.4. This Thesis

In this Thesis we investigate gap-plasmon resonances of film-coupled gold nanoparticles, with the aim to provide fundamental insights, and to demonstrate control of the gap plasmon resonances through engineering of the local particle environment at the nanoscale.

In Chapter 2, we demonstrate voltage controlled wavelength tuning of the gap plasmon resonance of gold nanoparticles on an aluminum film using single particle microscopy and spectroscopy. Anodization of the Al film after nanoparticle deposition forms an aluminum oxide spacer layer between the gold particles and the Al film, modifying the particle-substrate interaction. Darkfield microscopy reveals ring-shaped scattering images from individual Au nanoparticles, indicative of gap plasmon resonances with a dipole moment normal to the substrate. Single particle scattering spectra show narrow plasmon resonances that can be tuned over tens of nanometers by varying the anodization voltage. All observed experimental trends could be reproduced in numerical simulations.

In Chapter 3, gold nanoparticles on Al_2O_3 coated gold films are presented as a chemically and thermally robust platform for molecular sensing. Single particle spectroscopy as a function of Al_2O_3 coating thickness shows reproducible gold nanoparticle scattering spectra associated with Au NP gap plasmon resonances in the range from 690 nm to 610 nm as the Al_2O_3 thickness increases from 0 to 3.4 nm. Numerical simulations of these structures indicate that surface

enhanced Raman spectroscopy enhancement factors in excess of 10^6 can be achieved. The stability of the Al_2O_3 coated structures under high power laser irradiation was tested, revealing stable scattering spectra upon irradiation with 100 W/mm^2 at the particle resonance wavelength.

In Chapter 4, the effect of nanoscale surface roughness on the surface plasmon resonance of gold nanoparticles on thermally evaporated gold films is investigated experimentally and numerically. Single-particle scattering spectra obtained from 80 nm diameter gold particles on a gold film show significant particle-to-particle variation of the peak scattering wavelength of ± 28 nm. The experimental results are compared with numerical simulations of gold nanoparticles positioned on representative rough gold surfaces, modeled based on atomic force microscopy measurements. The predicted spectral variation and average resonance wavelength show good agreement with the measured data. These results highlight that surface roughness of the metal film can significantly affect gap plasmon resonances in the absence of a dielectric spacer layer.

In Chapter 5, we present a study of gap-plasmon enhanced photoluminescence of an individual gold nanoparticle on a gold film. The photoluminescence spectra of gold nanoparticles on an Al_2O_3 -coated gold film under both 532 and 633 nm excitation show a clear peak near the measured gap-plasmon resonance wavelength. Comparing the collected emission spectrum with that from a gold reference film under 633 nm excitation, a peak photoluminescence enhancement factor of 28 000 is observed. The strong photoluminescence enhancement factor is shown to be a result of the gap-plasmon mediated enhancement of the carrier generation rate and the electron-hole recombination rate. The spectral shape and absolute magnitude of the enhancement factors for both excitation wavelengths are reproduced using numerical calculations without the use of any free parameters. The good correspondence between modeled and measured

photoluminescence enhancement indicates that plasmon enhanced PL can be used to accurately determine local field enhancement factors.

In Chapter 6, the gap-plasmon resonance of gold nanoparticles placed in a nanohole in a metallic film is investigated in single particle microscopy and spectroscopy. Scattering and transmission measurements reveal that gap-plasmons of the so-called *hole-in-one* structure can be excited and observed under near-normal incidence excitation and observation. Numerical simulations suggest that a maximum local electric field enhancement factor at the gap-plasmon resonance of ~58 can be achieved, with a resonance hot-spot near the top surface of the structure. The proposed structure enables normal incidence excitation with a high field enhancement factor and easy access to the gap plasmon related hot-spot, which makes the structure attractive for use in gap-plasmon enhanced biochemical sensor arrays.

Finally, Chapter 7 concludes with a summary and outlook.

2. POST-FABRICATION VOLTAGE CONTROLLED RESONANCE TUNING OF NANOSCALE PLASMONIC ANTENNAS

2.1. Introduction

Nanoscale optical antennas that support localized surface plasmon resonances are receiving a tremendous amount of attention due to their ability to produce large optical field enhancement and extreme field confinement. Localized surface plasmon resonances of nanoscale metallic structures enable a broad range of applications and effects, including Surface Enhanced Raman Spectroscopy (SERS) [14, 58], plasmon enhanced nonlinear refraction and absorption [93, 94], plasmon enhanced harmonic generation and frequency mixing [95-97], plasmon enhanced biochemical sensing [98, 99], plasmon enhanced internal photoemission [78, 100, 101] , and plasmon enhanced photovoltaics [102, 103]. The response of nanoscale optical antennas can be engineered through a choice of material, size, shape of the structure, as well as the local environment [104, 105]. For nanoantennas that are to be used predominantly in a fixed environment (*e.g.* in an aqueous solution), this leaves little room for control of the antenna response after fabrication: once established the antenna composition, size, and shape are not easily modified. Here we present a method to modify the resonance response of nanoscale antennas after fabrication through substrate controlled resonance tuning.

It is well known that a polarizable substrate can affect localized plasmon resonances of metal nanoparticles. Early work by Kuhn provided a theoretical description of the interaction between a metal surface and molecular emitters, showing a distance dependent emission lifetime and quantum yield due to interaction of the dipole with induced image charges in the metal, as

well as a small emission wavelength shift [106]. Shortly thereafter Antoniewicz demonstrated theoretically that a point dipole near a metal surface exhibits an increased effective polarizability [37]. In subsequent theoretical work by Takemori *et al.* [38] and Ruppin [39] it was shown that similar effects occur in the coupling between a metal nanoparticle and a metal substrate. In particular the presence of the metal substrate was shown to cause a redshift of the particle-related absorption spectrum as a result of dynamic image charges. More recently, several experimental studies demonstrated plasmon resonance shifts of metal nanoparticles on a variety of substrates [41-43, 45-48, 107-109], and wavelength shifts as large as few hundred nanometer were observed. However, in all these studies the particle resonance was fixed once the particles were placed on the substrate, and no further resonance control was attempted after particle deposition.

In the present study we demonstrate post-deposition control of the localized plasmon resonance of individual gold nanoparticles on an aluminum film. Anodization of the aluminum film enables the growth of a stable aluminum oxide (Al_2O_3) film [110] that acts as a chemically controlled spacer layer between the Au nanoparticles and the Al film. Using single-particle scattering spectroscopy we track the plasmon resonance response of a set of individual deposited nanoparticles after several anodization steps, and demonstrate that the variable spacer layer thickness enables precise control of the nanoparticle resonance frequency. The method appears to leave the Au particles unaffected. While this work considers spherical gold nanoparticles, the presented approach could enable *in-situ* or post-fabrication optimization of a wide variety of more complicated nanoantenna structures, provided that the antenna material is not affected by the anodization process. The observed precise resonance frequency control could enable new systematic studies of light-matter interactions at the nanoscale.

2.2. Experiment and Simulation

2.2.1. *Experiment*

Samples were prepared on a 3-inch [100] silicon wafer with resistivity $> 1 \Omega\text{-cm}$. A 100 nm thick aluminum layer was deposited onto the Si wafer using thermal evaporation at a deposition rate of 12 Å/s using an Edwards FL 400 system. After deposition, exposure to ambient conditions leads to the rapid formation of a stable native aluminum oxide layer on the sample with a typical thickness of 2-4 nm [111, 112]. The Al-coated silicon wafer was cleaved into $\sim 1 \text{ cm}^2$ pieces. For nanoparticle deposition, a monodispersed gold nanoparticle colloid solution with a particle diameter of $60.4 \text{ nm} \pm 2.6 \text{ nm}$ was used (BBInternational, United Kingdom). It should be noted that this size range corresponds to the vendor-specified batch-specific size histogram. The colloidal solution contains trace amounts of citrate, tannic acid and potassium carbonate. The colloid was diluted with ethanol to a concentration of $2 \times 10^8 \text{ particles/mL}$. Approximately 4 μl of colloid was dropped on the samples using a high precision pipette and immediately dried using air flow. The ethanol diluted solution was found to wet the substrate well. This procedure was found to lead to well-separated individual particles located on the Al surface with a particle density of $\sim 1 \text{ particle}/100 \mu\text{m}^2$. The nanoparticle-coated wafer and a similarly prepared reference sample without nanoparticles were subsequently anodized in a 3 wt.% ammonium tartrate solution in deionized water ($> 10 \text{ M}\Omega\text{-cm}$) at room temperature using a stainless steel counter electrode at anodization voltages in the range 1.5 V – 12 V. Following each anodization step the sample was rinsed in deionized water and dried using air flow. This procedure produces an amorphous barrier-

type Al₂O₃ layer with a thickness that is controlled by the anodization voltage [110, 113]. The oxide thickness of the reference sample after each anodization step was determined using a J. A. Woollam variable angle spectroscopic ellipsometer. Scanning electron microscopy images were obtained using a Zeiss ULTRA-55 Field Emission Scanning Electron Microscope.

Optical microscopy and single particle scattering spectroscopy measurements were carried out after the initial particle deposition as well as after each anodization step using an Olympus BX-51 reflected light optical microscope equipped with standard dark-field optics. Most particles were found to remain on the substrate after anodization. The scattering spectra of individual nanoparticles were collected using a 50× dark-field objective (Olympus MPlanFl 50× BD, N.A.=0.80) and a multimode fiber connected to a spectrometer (Horiba Jobin-Yvon iHR320 monochromator with Synapse CCD array). The effective collection area on the sample was ~20 μm², and the spectral resolution was 10 nm. Single particle scattering spectra $I_{sc}(\lambda)$ were obtained using the relation $I_{sc} = (I_{NP} - I_{REF})/I_{IN}$ with I_{NP} the signal obtained from an area containing a single nanoparticle, I_{REF} the signal collected from a nearby region without a nanoparticle, and I_{IN} the lamp spectrum. All spectra were corrected for the detector dark current. Finally, the thus obtained single particle scattering spectra were corrected for a small remaining offset (< 4% of the peak scattering signal). The detailed data collection procedure is described in Appendix A.1.

2.2.2. Simulations and Calculations

Scattering spectra were determined based on three-dimensional frequency domain electromagnetic simulations [29] of a with lateral size 200 × 200 nm². The silicon substrate was

replaced with SiO_2 ($n=1.5$) due to limitations of the modeling software, however this choice is not expected to affect the results due to the relatively large Al thickness of 100 nm. Literature data were used for the Al_2O_3 [114], Au [115], and Al [4] dielectric functions. The structure is illuminated at an angle corresponding to the N.A. of the objective used in the experiment. The z-dipole moment μ_z of the nanoparticle was determined at each frequency from the calculated field distributions, and the scattered power of the oscillating dipole was assumed to be proportional to $|\mu_z|^2\omega^4$ with ω the angular frequency of the dipole oscillation [1].

2.3. Results and Discussion

Figure 2.1:(a) shows a real-color dark-field microscopy image of 60 nm Au particles deposited from a colloidal solution onto a 100 nm thick as-deposited Al film with a 3.6 nm thick native Al_2O_3 layer. The image shows many individual scatterers that are well separated, enabling single particle spectroscopy. All scatterers exhibit similar brightness and color, suggesting that these correspond to single Au nanoparticles that were deposited from the colloidal solution. This is further confirmed by the corresponding scattering spectra described below. Close inspection of the image shows slight color variations among the particles, possibly indicating small differences in local environment, *e.g.* surface roughness of the deposited Al, variations in native oxide thickness, small size and shape variations of the particles, or irregular deposition of surfactants from the colloidal solution. The partly inhomogeneous nature of the scattering response of supported nanoparticles would lead to artificially broadened resonance lines in ensemble measurements, highlighting the need for single-particle measurements. All particles produce a

ring-shaped image under the microscope. Such ring shaped images were also observed in prior experiments conducted by Mock *et al.* [42] and Hu *et al.* [46] on noble metal particles near a gold surface. This intensity pattern is indicative of a scatterer with a dipole moment that is aligned along the optical axis, *i.e.* normal to the sample surface. This polarization will be referred to as ‘z-polarized’.

Figure 2.1:(b)-(e) show darkfield microscopy images of the same four Au nanoparticles (marked by the dashed rectangle in Figure 2.1:(a)) for the as-deposited sample, as well as after anodization at voltages V_a of 3V, 6V, and 9V. The color of the scattered light is seen to change from yellow/orange to green as the anodization voltage increases, suggesting a controlled and gradual change in the local environment of the particles. For all voltages the scattering remains predominantly z-polarized. Figure 2.1:(f) and Figure 2.1:(g) show scanning electron microscopy (SEM) images of a Au nanoparticle before anodization and another Au nanoparticle after anodization. The nanoparticles show evidence of faceting, which could introduce slight variations in particle response and particle-substrate interaction.

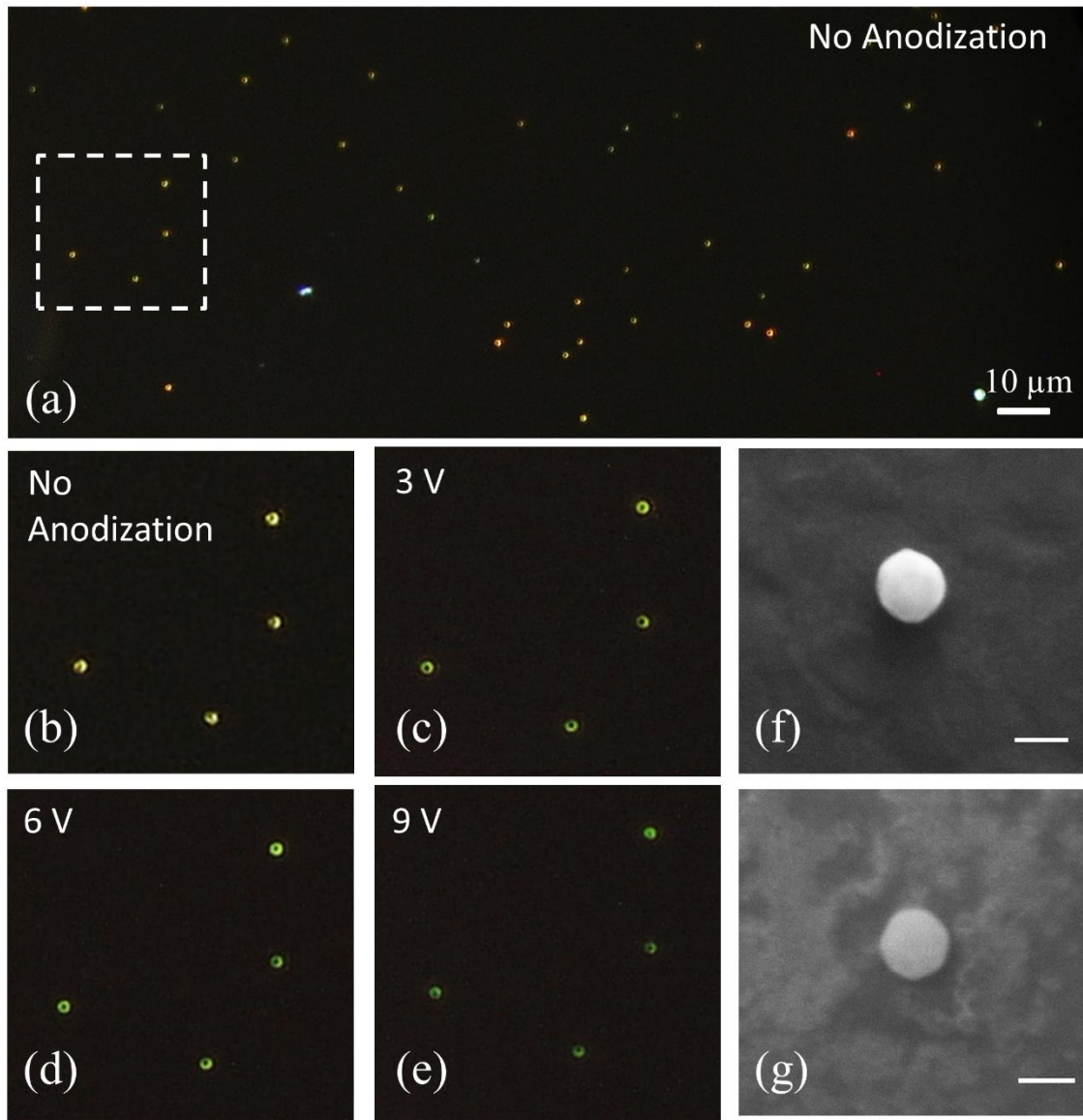


Figure 2-1: Darkfield microscopy images of 60 nm diameter gold nanoparticles on an Al substrate prior anodization (a) and (b), and after anodization at different voltages (c) to (e). Scanning electron microscopy images of Au nanoparticles before (f) and after (g) anodization.

To correlate the experimental observations with the oxide thickness, ellipsometry measurements were carried out after each anodization step. The inset of Figure 2.2(a) shows the measured Al_2O_3 thickness as a function of anodization voltage (solid circles). The data reveal a linear relationship between the Al_2O_3 thickness d and the anodization voltage given by $d(\text{nm}) = 3.42 + 1.07 V_a$. To quantify the observed color change in Figure 2.1:(b)-(e) single particle scattering spectra were taken of a set of nanoparticles for all anodization voltages. Figure 2.2(a) shows representative scattering spectra for one of these particles for the as-deposited sample, as well as for three anodization voltages. All spectra show a single well-defined scattering peak with a FWHM of 70-90 nm, and a peak position in the range 550 nm – 580 nm, consistent with the expected scattering spectrum of single Au nanoparticles. As the anodization voltage is increased, two trends are observed. First, the resonance wavelength is seen to blue-shift. Secondly, the peak scattering signal is seen to decrease.

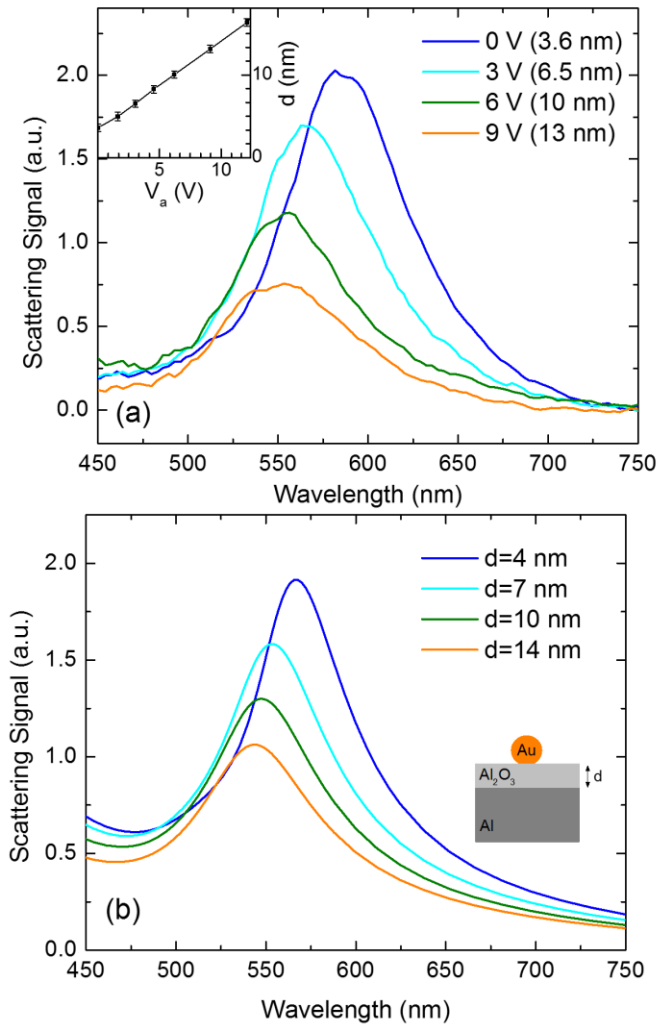


Figure 2-2: (a) Scattering spectra from a single Au nanoparticle for different anodization voltages. The corresponding oxide thicknesses are shown in parentheses. The inset shows the measured Al₂O₃ thickness as a function of anodization voltage. The sample structure is shown schematically. (b) Calculated scattering spectra of 60 nm Au nanoparticles on an Al₂O₃ coated aluminum film as a function of Al₂O₃ thickness d corresponding to the thickness values in panel (a). The sample structure is shown schematically.

To quantitatively analyze the observations in Figure 2.2(a) numerical simulations were carried out. Figure 2.2(b) shows the obtained scattering spectra for 60 nm diameter Au nanoparticles on an Al₂O₃ covered Al film for four different oxide thicknesses d corresponding to the oxide thicknesses of the experimental data in Figure 2.2(a). The simulated scattering spectra show remarkable agreement with the experimental data, demonstrating similar resonance wavelength, resonance shift, resonance linewidth, and reduction in scattering strength as the oxide thickness is increased. The simulated data exhibit a slightly higher signal at wavelengths above the plasmon resonance compared to the experimental results. This difference is due in part to the background correction procedure described in the Experimental Section 2.2 and Appendix A.1.

Figure 2.3(a) shows the measured peak wavelength position (solid squares) as a function of oxide thickness d obtained for a set of 10 separate particles. The error bars represent the experimental standard deviation, indicating slight spectral differences among the particles as also observed in Fig. 2.1(a). The statistical variation may be due to surface contaminants, inhomogeneity of the oxide thickness in the anodization process, differences in particle shape (*e.g.* faceting), or particle size variations. As the oxide thickness increases the average peak scattering wavelength blue-shifts from 584 nm to 550 nm, corresponding to a ~30 nm shift in resonance wavelength. The solid line in Figure 2.3(a) shows the simulated scattering peak position obtained by repeating the simulations in Figure 2.2(b) for several additional oxide thicknesses assuming a particle diameter of 60 nm. The simulated results reproduce the experimental trends remarkably well. Based on numerical simulations as a function of particle size (see Appendix A.2.) the known size distribution of the Au colloid could introduce peak wavelength variations of ± 2 nm, as indicated by the error bars on the simulated data in Figure 2.3. Note that no free parameters were

used in the calculation of the resonance wavelength. The experimental resonance wavelength is approximately 10 nm larger than the simulated resonance wavelength for all oxide thicknesses. This systematic difference is possibly due to slight differences between experimental and literature dielectric functions, the presence of an adventitious surface water layer [116, 117], or the presence of surface contaminants after deposition or anodization that were not considered in the simulations.

Figure 2.3(b) shows the experimentally observed peak scattering signal (open squares) as a function of oxide thickness for the same set of 10 Au nanoparticles. The error bars in the experimental data represent the standard deviation of the peak scattering signal from all particles at each oxide thickness. The scattering signal exhibits a gradual reduction as the Al_2O_3 thickness increases. The solid line shows the corresponding numerical simulation results, and the error bars on the simulated data correspond to a predicted 22% variation in peak scattering signal corresponding to the known particle size variation, see Appendix A.2. The simulations exhibit a similar reduction in scattering strength as the oxide thickness is increased. This reduction in scattering strength is due in part to the frequency dependent imaginary part of the Au dielectric function in this frequency range: as the oxide thickness increases from 3.6 nm to 16.3 nm, the blue-shift of the plasmon resonance leads to an increase in $\text{Im}(\epsilon_{\text{Au}})$ from 1.64 to 2.14, resulting in stronger plasmon damping for large oxide thickness.

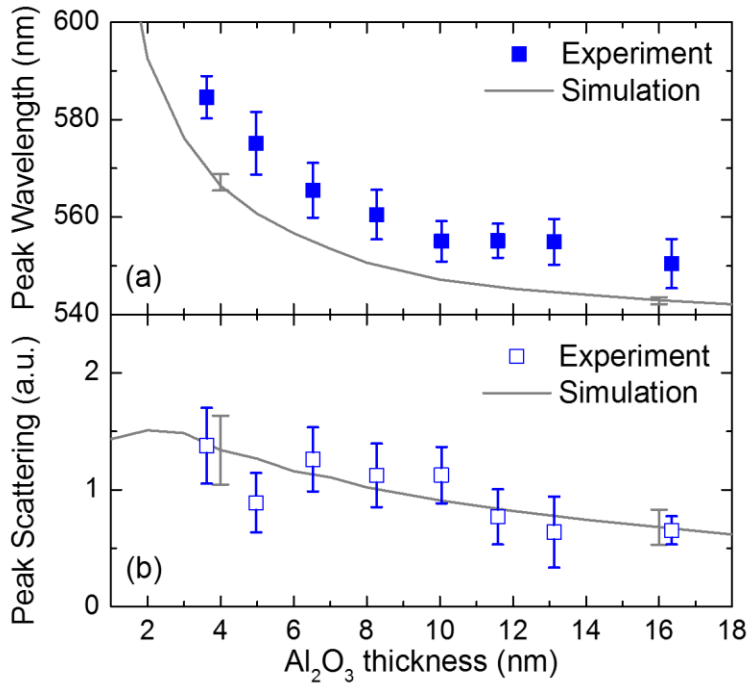


Figure 2-3: (a) Measured z-polarized plasmon resonance wavelength and (b) the corresponding peak scattering signal of 60 nm diameter Au nanoparticles on an oxidized Al film as a function of Al_2O_3 thickness. The lines represent the results from numerical simulations. The error bars on the simulated data represent predicted signal variation due to the known colloid size dispersion.

The experimental observations can be understood in terms of the interaction of the oscillatory nanoparticle dipole moment with its dynamic image dipole in the metal substrate. Figure 2.4(a) schematically shows an Au nanoparticle on an aluminum film with an Al_2O_3 spacer under TM illumination with electric field amplitude E_{in} . At the illumination angle θ_{in} of the dark field objective, $\theta_{\text{in}} \sim 69^\circ \pm 2^\circ$, the illumination contains both x- and z-polarized components. These field components in principle allow the excitation of two distinct sets of dipolar plasmon resonances and resulting image charge distributions in the Al film corresponding to x-polarized

excitation and z-polarized excitation. Figure 2.4(b) schematically shows the induced horizontal (x-polarized) oscillation of the particle dipole moment. At frequencies well below the Al plasma frequency this dipole oscillation on the Au particle induces an oscillating image charge in the Al film with a dipole moment opposite to that of the nanoparticle. This anti-parallel x-polarized dipole orientation is known to result in a redshift in the scattering spectrum compared to the response of an individual nanoparticle [46, 48, 118]. Figure 2.4(c) shows the corresponding situation for z-polarized excitation of the particle. In this case, the induced dynamic image dipole is parallel to that of the nanoparticle, again leading to a redshift of the resonance. The longitudinal near-field interaction between dipoles is known to be twice as strong as transverse interaction, suggesting that a stronger red-shift would be observed for the z-polarized mode. Since the near-field dipole-dipole interaction strength decreases rapidly as the dipole separation increases, the surface-induced red-shift is expected to reduce as the oxide thickness is increased, corresponding to the experimentally observed blue-shift for increasing oxide thickness. It should be noted that the finite polarizability of Al_2O_3 also affects the particle response. Replacing the Al_2O_3 layer by an air gap would place the particle in a lower refractive index environment, leading to an additional blueshift of ~ 15 nm for large particle-film separation based on numerical simulations.

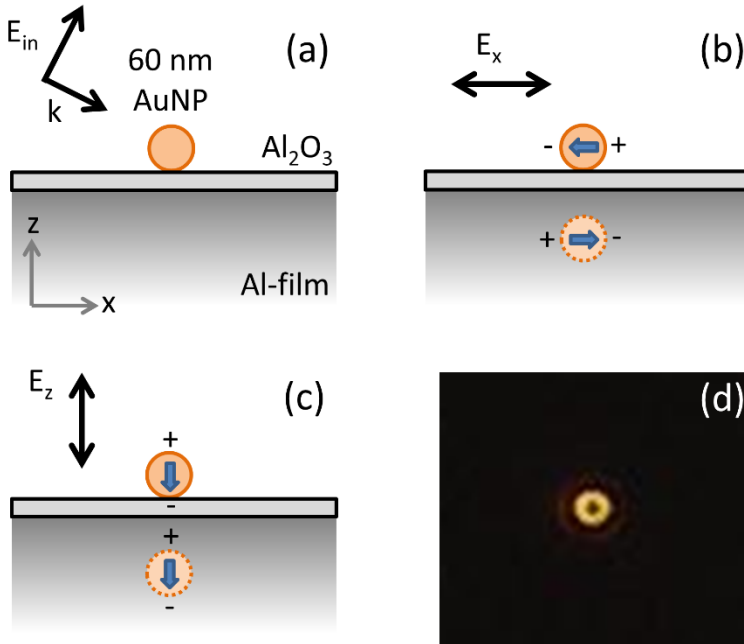


Figure 2-4: Schematic representation of (a) darkfield illumination of a supported Au nanoparticle on an oxidized aluminum film, (b) the particle polarization and image charge distribution resulting from x-polarized excitation and (c) from z-polarized excitation, and (d) a color image of the observed dark-field microscopy image of a Au particle on the native oxide layer on the Al film

Due to the different interaction strength for lateral and normal dipoles, the presence of both x-polarized and z-polarized excitation could be expected to produce a double peak feature in the nanoparticle scattering spectra, with a different red-shift depending on the polarization. However, the experimental results show single scattering peaks and pronounced ring-shaped scattering patterns (see Figure 2.1:(a)-(e) and Figure 2.4(d)) indicating that only the z-polarized mode is detected. The absence of the lateral oscillation mode in the scattering images and spectra can be

understood by considering the charge configurations of the two oscillation modes. The vertical mode induces an image dipole that is aligned along the particle dipole (Figure 2.4(c)), effectively generating an extended dipole that can radiate into the far-field, albeit predominantly along the sample surface. The horizontal mode on the other hand induces an image dipole that is oriented anti-parallel to the particle dipole, corresponding to a predominantly quadrupolar charge configuration (Figure 2.4(b)) which does not radiate effectively into the far-field for particle-image charge separations much less than $\lambda/2$. A second independent reason for the absence of the lateral dipole oscillation mode is related to the excitation efficiency. The oxide coated reflective Al substrate affects p-polarized and s-polarized illumination components differently, leading to significantly lateral and normal excitation field strengths. Assuming illumination with incoherent light at an angle of 70° containing equal TM and TE contributions, the Fresnel reflection coefficients predict that the E_z excitation 30 nm above an Al surface is approximately a factor 8 stronger than the E_x excitation. We therefore attribute the absence of a clear x-polarized contribution in the scattering images and spectra to the combined effect of a reduced excitation efficiency and a low radiation efficiency of the x-polarized mode. Note that the inhomogeneous dielectric environment of the Au nanoparticles is also expected to lead to the excitation of multipolar plasmon resonances. These multipolar resonances occur at frequencies above the dipolar plasmon resonance, and are not observed in the experiments.

The results presented here unambiguously demonstrate the possibility of controlling localized plasmon resonances through substrate anodization, with an experimentally observed tuning range of ~ 30 nm. In the material system considered here the native oxide layer puts an upper

bound on the resonance wavelength, as it sets a minimum distance between the nanoparticle and the induced dynamic image charge. The simulated resonance wavelengths for thinner oxide layers (Figure 2.3(a)) suggest that significantly larger red-shifts could be achieved in the absence of a surface oxide layer. Experiments and applications utilizing these substrate-controlled resonances will likely involve immersion of these structures in aqueous environments, which is expected to result in an additional red-shift, reduced resonance linewidth, and improved field enhancement for spherical Au nanoparticles. Finally, the experiments involved Au nanoparticles that are thought to be only weakly bound to the sample surface. The fact that several anodization steps could be carried out without apparent degradation of the electromagnetic response of the nanoparticles and without detaching a majority of the particles suggests that the method shown here could be used to tune the resonance response of wide variety of plasmon resonant nanoantenna structures, provided that the antenna material is not affected significantly by the anodization process.

2.4. Summary

Plasmon resonance control of 60 nm diameter Au nanoparticles supported on an aluminum film is demonstrated through substrate anodization, resulting in the formation of a thin Al_2O_3 spacer layer between the Au nanoparticles and the Al substrate. The Au nanoparticles produce ring-shaped scattering images in dark-field microscopy, indicative of z-polarized plasmon resonances. Single-particle scattering spectra show a consistent blue-shift of the plasmon resonance and a gradual drop in the scattering signal strength as the Al_2O_3 thickness is increased. The observations are explained in terms of oxide thickness dependent coupling between the

nanoparticle and a dynamic image charge distribution in the substrate. The experimental results and numerical simulations show remarkable agreement. The presented approach could be used for post-fabrication plasmon resonance optimization in a wide variety of plasmonic nanoantenna structures. The technique is simple, controlled, and could be useful for several applications that rely on plasmonic nanoantennas such as SERS, plasmon enhanced photoemission, and biodetection through observation of plasmon resonance shifts.

3. WIDE-BAND SPECTRAL CONTROL OF GOLD NANOPARTICLE PLASMON RESONANCES ON THERMALLY AND CHEMICALLY ROBUST SENSING PLATFORM

3.1. Introduction

Plasmonic resonances of metal nanostructures are widely used in sensing applications due to the extremely strong localized field enhancement they can produce, enabling the sensitive detection of analyte molecules in ultrasmall volumes through changes in plasmon resonance wavelength, fluorescence signal strength, and Raman scattering signal. Plasmon mediated field enhancement has enabled single-molecule Raman spectroscopy in small metal nanoparticle aggregates [52, 53]. The main enabling element in these experiments is the formation of nanogaps between adjacent nanoparticles resulting in *hot spots*: regions that exhibit extremely high field enhancement factors. While particle aggregates produce large field enhancement, the randomness of the structure formation and the extreme sensitivity of the optical response to the gap size makes nano-aggregates unpredictable, unstable, and difficult to produce reliably. For these reasons, a lot of effort has been put into developing plasmon-mediated biochemical sensor platforms that can provide small gap sizes while also having predictable and stable plasmon resonances. Select approaches include the use of electron-beam lithography (EBL) [119, 120], on-wire lithography [121, 122], and self-assembly [123-125].

An approach that has recently been receiving increasing attention is the use of chemically synthesized metal nanoparticles deposited onto high dielectric constant substrates, or onto metallic films with an optional spacer layer. In the resulting structures, a hot-spot is formed in the gap

between the nanoparticle and the substrate due to the development of dynamic image charges in the substrate [43, 126, 127]. This approach allows the controlled formation of structures that provide high field enhancement using low-cost and simple fabrication methods [66, 128]. Moreover, this approach can make use of nanostructures that are close to their thermodynamic equilibrium shape (approximately spherical), promising thermally stable performance. Finally, the plasmon resonance wavelengths of supported nanoparticles can be controlled by modifying the nanoparticle-to-substrate separation e.g. using a low-dielectric constant spacer layer on a large-dielectric constant substrate. Using this approach, it has been shown that plasmon resonances of gold nanoparticles which typically occur in the green can be tuned across the entire visible range by changing the substrate composition [43, 109], modifying the substrate thickness [129], and adjusting the gap size between the nanoparticle and the substrate [41, 42, 46, 130]. These approaches move the plasmon resonance of stable Au nanospheres to frequencies well below Au interband transitions, resulting in sharper plasmon resonances and larger field enhancement factors. Prior demonstrations of substrate controlled plasmon resonance made use of organic spacer layers [41, 131], which when used in Raman detection are expected to introduce a background signal due to Raman scattering from the spacer layer molecules, and may be chemically or thermally damaged relatively easily. An alternate approach using all-inorganic materials resulted in fragile systems [46] due to weak oxide-substrate binding using the SiO₂-Au system, or a limited tuning range [130] due to the presence of a native oxide layer using the Al₂O₃-Al system.

To address these issues, here we present experiments on the control of the plasmon resonance of Au nanoparticles using aluminum oxide (Al_2O_3) coated gold films experimentally and numerically. We demonstrate that this structure provides reproducible Au nanoparticle resonance spectra that can be spectrally tuned over at least an 80 nm bandwidth by varying the oxide spacer thickness and that remain virtually unaltered upon high-power laser irradiation. The controllable and reproducible plasmon resonance wavelength, large tuning range, stability of the structure under laser irradiation, and the chemical stability of all materials used make the presented system a good candidate for a reliable plasmonic sensing platform for applications such as surface enhanced Raman spectroscopy (SERS) and plasmon-enhanced fluorescence spectroscopy [132-134].

3.2. Experiment and Simulation

3.2.1. Sample Preparation and Characterization

Aluminum oxide coated gold films were prepared by thermal evaporation using a multi-pocket Edwards FL 400 thermal evaporator (base pressure $< 10^{-5}$ mbar). Gold films with a thickness of 50 ± 2 nm were deposited onto glass cover slips using a 2 nm Cr wetting layer. Few-nm thick aluminum films were deposited onto the gold-coated samples without breaking vacuum. A gold substrate without Al coating was used as a reference sample. The film thickness of all deposited films was verified using a Woollam M2000 Variable Angle Spectroscopic Ellipsometer. Al films are well known to form a thin native surface oxide layer of 2-4 nm [135] upon exposure to ambient environment. The Al layers deposited in the experiment are thinner than the 3.6 nm

Al_2O_3 thickness formed on thermal-evaporated Al films [130] and completely oxidized into a thin Al_2O_3 layer after exposure to air. Indeed, no evidence of metallic aluminum was found in post-deposition variable angle spectroscopic ellipsometry. Long range Al_2O_3 thickness variation on each sample was verified by performing ellipsometry at various locations on the samples. The variations in the measured thickness are included as error bars in Fig. 4. The root-mean-square surface roughness of the samples was determined using atomic force microscopy (AFM). The roughness was found to be ~ 1.5 nm on samples with and without Al_2O_3 coating, indicating that the roughness is dominated by the Au film roughness. Following the deposition steps, a colloidal solution of gold nanoparticles (BBInternational) with a batch-specific size distribution of 60.4 ± 2.6 nm was diluted in ethanol to a concentration of 2×10^8 particles/mL and drop coated onto the substrates. The droplet was observed to spread rapidly across the sample surface and was subsequently left to dry in air. Post-deposition microscopy of the samples revealed well-separated optical scatterers attributed to the presence of isolated Au nanoparticles, with inter-particle separations exceeding several microns.

3.2.2. Optical Microscopy and Spectroscopy

Dark field microscopy images were taken using an Olympus IX-71 inverted microscope equipped with a $50\times$ dark-field objective (Olympus UMPPlanFL $50\times$ BD, N.A.=0.75) and a Canon EOS 450D digital camera. Spectral images of the samples were recorded using a HSi-440C Hyperspectral Imaging System (Gooch & Housego) at a spectral resolution of 10 nm. High-resolution scattering spectra of individual gold nanoparticles were collected using an imaging

spectrometer attached to the microscope (Horiba iHR320 with Synapse CCD array) with an effective collection area of $\sim 8 \times 8 \mu\text{m}^2$ at the sample surface and a spectral resolution of 10 nm. All spectra were corrected for the dark current, and normalized to the scattering spectrum of a nearby region of the sample.

3.2.3. Numerical Simulation and Calculation

Numerical simulations were done based on the frequency domain finite integration technique [29] using literature data for the dielectric functions of gold [115] and aluminum oxide [114]. Details of the simulation and calculation procedures are provided in Appendix B.2.

3.2.4. Single Particle Stability Measurements

A linearly polarized 633 nm laser beam was focused onto the substrate at an angle of incidence of 15° using off-center illumination of the back aperture of a $50\times$ dark-field objective (Olympus UMPlanFL $50\times$ BD, N.A.=0.75). The beam polarization was chosen to result in p-polarized irradiation of the Au nanoparticles. The laser spot was found to be close to circular with an approximately Gaussian beam profile and a FWHM of $\sim 2.2 \mu\text{m}$ as measured by nanoparticle-mediated beam sampling (see Appendix B.3.). The peak irradiance incident on the nanoparticles was set to $\sim 100 \text{ W/mm}^2$.

3.3. Results and Discussion

Darkfield microscopy images of gold nanoparticles on Al₂O₃ coated gold films with five different Al₂O₃ thicknesses (0 nm, 1.31±0.18 nm, 1.54±0.21 nm, 2.20±0.32 nm, and 3.37±0.18 nm) were recorded by two CCD cameras; a Canon EOS 450D digital camera for real-color images and a HSi-440C Hyperspectral Imaging System for spectral images. Figure 3.1(a)-(e) show representative real-color dark-field microscopy images of isolated gold nanoparticles on five samples. Figure 3.1(a) shows the scattering observed from three Au nanoparticles. The particles appear green, with each particle exhibiting a single central maximum of the scattering intensity. This kind of spot shape is known to be indicative of a laterally (surface-parallel) polarized charge oscillation on the particle [136, 137]. In addition the green spots are seen to be surrounded by a faint red ring-shaped scattering pattern. This spot shape is indicative of a z-polarized (vertically polarized) plasmon resonance, and has been observed previously on metal nanoparticles on various metallic substrates [42, 130, 136]. Figure 3.1(b)-(e) show similar images taken of samples with a progressively thicker Al₂O₃ layer between the Au nanoparticle and the gold film. All images show a similar red ring-shaped scattering pattern, while the green central spot appears relatively weak. These images seem to suggest that the spectral differences among the four Al₂O₃ coated samples are limited. Figure 3.1(f)-(j) show corresponding false-color images of the same particles shown in Figure 3.1(a)-(e), based on images taken with a hyperspectral camera attached to the microscope. Images were taken in the spectral range 500 nm - 800 nm with a collection bandwidth of 10 nm per image, and a spectral sampling of 3 nm, resulting in a stack of 100 images. The images were processed (see Appendix B.1.) resulting in a color mapping of the peak scattering

wavelength according to the scale bar shown below the images. Figure 3.1(f) shows the false color image of the same three Au nanoparticles on the gold film shown in Figure 3.1(a). Two main differences are observed. First, the central maximum (green scattering signal in Figure 3.1(a)) is not visible since the false-color mapping emphasizes wavelengths in the range 600 nm - 700 nm. Second, instead of a ring-shaped scattering image, two separated scattering spots are observed. This is a result of the polarization sensitive nature of the hyperspectral imager, eliminating the left and right parts of the ring-shaped pattern. Figure 3.1(f)-(j) reveal that the red z-polarized plasmon resonance is gradually tuned toward shorter wavelengths as the Al_2O_3 thickness increases. Additionally, particles in each individual spectral image appear of the same color, showing that a consistent resonance wavelength is obtained at each oxide thickness. These assertions are corroborated by additional single particle scattering spectra presented below.

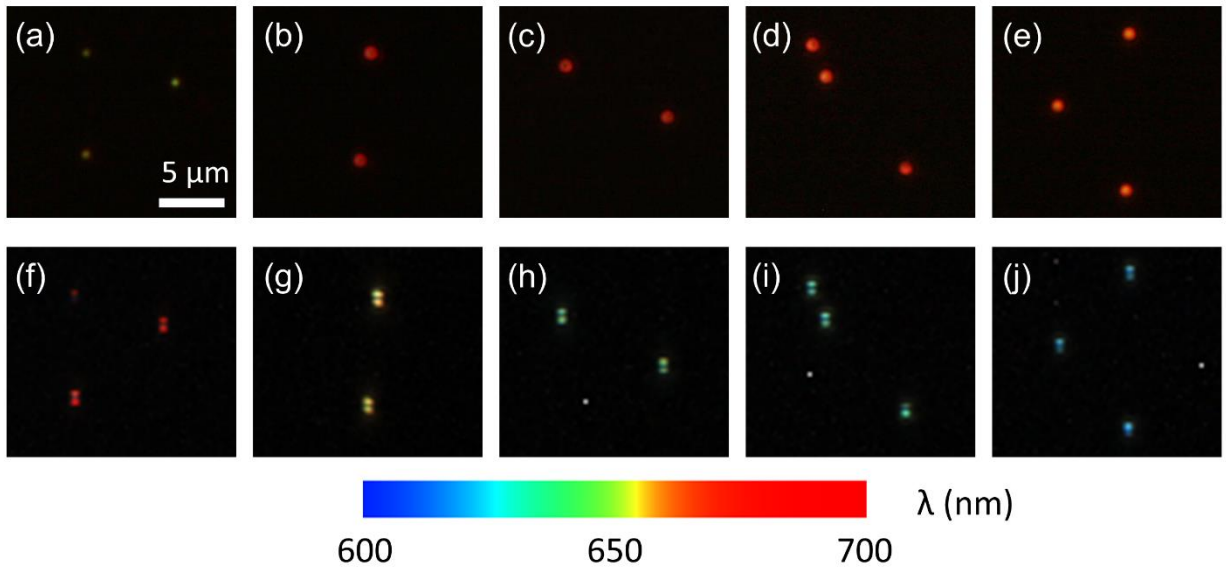


Figure 3-1: (a)-(e) Real-color dark-field microscopy images of gold nanoparticles on gold substrates with Al_2O_3 coating thickness 0, 1.3, 1.5, 2.2, and 3.4 nm, respectively. (f)-(j) False-color images of these same nanoparticles obtained using a hyperspectral camera taken in the range 500 - 800 nm. The color bar shows the wavelength representation used in figures (f)-(j).

To evaluate the response of the nanoparticles in Figure 3.1 in more detail, a large set of single-particle scattering spectra were taken for each sample. Figure 3.2(a) shows a typical scattering spectrum of an isolated gold nanoparticle on the gold substrate without Al_2O_3 (black solid line). The gray region represents the one-sigma confidence interval obtained by taking spectral measurements of fifteen randomly selected particles on the same sample. The spectrum shows a plasmon enhanced scattering peak at a wavelength of 690 nm (1.775 eV), with a Full Width at Half Maximum (FWHM) of 88 nm (0.223 eV). The observed spectral shape and linewidth are typical for a dipolar plasmon resonance in gold nanoparticles and similar to the extinction peak

width of these gold nanoparticles in colloidal solution (\sim 80 nm linewidth, specified by the supplier). However the resonance wavelength is red-shifted by \sim 150 nm compared to the plasmon resonance wavelength of 544 nm of these nanoparticles in colloidal solution (green dashed line and arrow in Figure 3.2(a)). The measured spectra also contain weak scattering features around 500 - 550 nm. The insets of Figure 3.2(a) show spectral images obtained from the same particle by collecting wavelength bands 545 - 555 nm (left), and 695 - 705 nm (right). These images confirm that the signal between 500 - 550 nm originates from an at least partly laterally polarized green plasmon resonance, while the signal at 690 nm originates from a z-polarized red plasmon resonance. The large redshift of the z-polarized resonance results from an interaction between the z-polarized electric dipole of the nanoparticle and induced dynamic image charges in the substrate [38, 39, 130]. The observed variation in signal strength of the scattering spectra as indicated by the confidence interval is attributed to the specified size variation of \pm 2.6 nm of the nanoparticles leading to an anticipated variation of the scattering signal strength by as much as \sim 30% assuming a scattering cross-section that is proportional to the square of the particle volume [2]. Note that the relatively strong scattering strength of the z-polarized resonance seems at odds with the observation of the weak red scattering in Figure 3.1(a). This is a result of the infrared cut filter present in the camera, leading to reduced response at wavelengths larger than 600 nm.

Figure 3.2(b)-(e) show the corresponding typical spectra and confidence intervals for gold nanoparticles on gold films coated with 1.3 nm (24 particles), 1.5 nm (14 particles), 2.2 nm (22 particles), and 3.4 nm (20 particles) thick Al_2O_3 spacer layers, respectively. As the oxide thickness increases from 0 nm to 3.4 nm, the peak scattering wavelength is seen to blue-shift from 690 nm

to 610 nm. This observed tuning range of 80 nm is significantly larger than that observed using anodization of an Al substrate in Chapter 2, where a resonance shift of only ~30 nm was observed. The larger tuning range is made possible by the absence of a limiting native oxide thickness, which allows for smaller particle-substrate separations than can be achieved in an Al₂O₃-coated Al system exposed to air. The scattering spectra of gold nanoparticles located directly on the gold film (Figure 3.2(a)) are seen to be broader than those of gold nanoparticles on Al₂O₃ coated substrates (Figure 3.2(b)-(e)), exhibiting linewidths of ~80 nm and 50 - 60 nm respectively. This may be due to the increased importance of nonlocal effects on the Au response for small particle-substrate spacing [138, 139]. Note that the scattering peak height of the z-polarized mode varies by less than 17% as the oxide thickness is changed (one-sigma interval). Finally, note that for all Al₂O₃-coated samples the lower bound of the confidence interval (marked by a vertical dash) peaks at a shorter wavelength than the upper bound of the confidence interval (marked by a plus symbol). This observation corroborates the assertion that the observed brightness fluctuations are due to particle size variations, since larger nanoparticles are known to produce stronger scattering signal and longer resonance wavelength, see e.g. Appendix A.2.

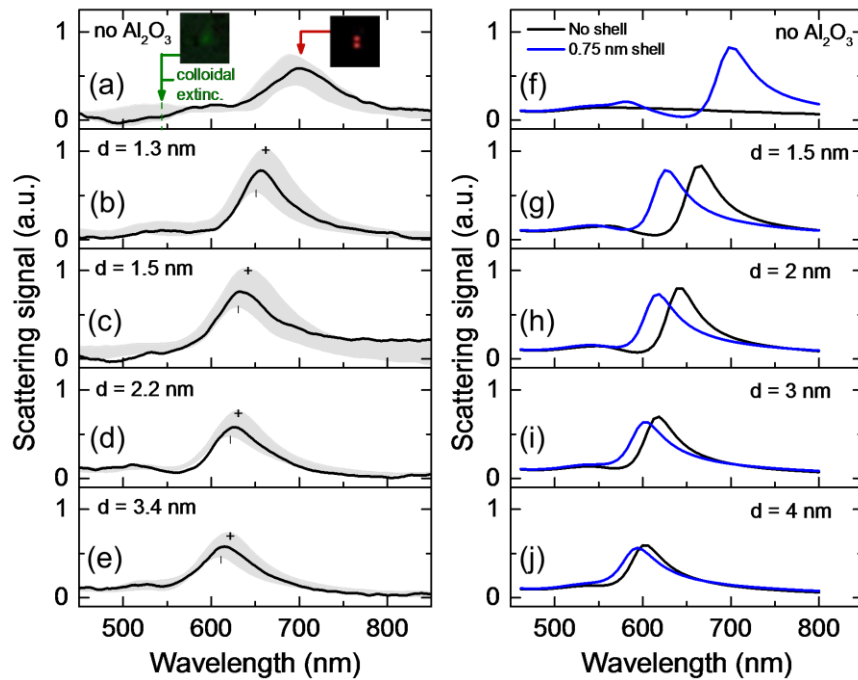


Figure 3-2: (a)-(e) Measured scattering spectra from single gold nanoparticles on gold substrates without an Al₂O₃ spacer layer and with 1.3, 1.5, 2.2, and 3.4 nm Al₂O₃ spacer layer, respectively. The shaded region on each plot represents the confidence intervals of the measurement and the black curve shows a typical scattering spectrum. The green arrow indicates the plasmon resonance wavelength of gold nanoparticles in colloidal solution. The insets in (a) show spectral images obtained from the same particle by collecting wavelength bands 545 - 555 nm and 695 - 705 nm. (f)-(j) Calculated scattering spectra of 60 nm gold nanoparticles on gold films coated with 0 nm, 1.5 nm, 2 nm, 3 nm, and 4 nm of Al₂O₃, respectively. The blue curves in (f)-(j) show the simulated scattering spectrum assuming the presence of a 0.75 nm thick organic coating on the gold nanoparticle.

To understand the observations made in Figure 3.1 and Figure 3.2(a)-(e), numerical simulations were carried out (see Appendix B.2.). Figure 3.2(f) presents the simulated scattering spectrum of a 60 nm diameter gold nanoparticle on a 50 nm gold film on a glass substrate with a refractive index of 1.5 (black line). The simulated spectrum shows a broad and weak scattering band around 550 nm and no evidence of a long wavelength resonance, markedly different from the experimentally observed spectrum. Part of this difference may be due to the fact that the simulation does not take into account the expected presence of organic ligands that remain on the particle surface or the Au film surface after deposition from solution. The simulations were repeated assuming that the nanoparticle surface is covered with a 0.75 nm thick organic layer, corresponding to the thickness of a monolayer of normally oriented citrate molecules. This choice results in a spectrum (Figure 3.2(f), blue line) that closely resembles the experimental data, showing a clear peak at 697 nm and a weaker scattering peak at 580 nm.

Figure 3.2(g)-(j) show the simulated scattering spectra of 60 nm diameter gold nanoparticles on gold films coated with a 1.5 nm, 2 nm, 3 nm and 4 nm thick Al_2O_3 layer. The figures contain both the calculated spectra of gold nanoparticle with and without a 0.75 nm organic coating. Both sets of the spectra show the same general trend as observed experimentally although it is clear that the presence of organic ligands significantly blue-shifts the spectral response of the particle.

To clarify the nature of the observed resonances, Figure 3.3 shows the calculated scattering spectrum of an Au nanoparticle on the Au film, assuming the presence of a 0.75 nm organic coating on the particle. The insets show electric field snapshots in the (x,z) plane of E_y (lateral field) at the

green resonance (550 nm) under TE illumination and of E_z (normal field) at the red resonance (690 nm) under TM illumination, displayed on the same relative scale. The full color range represents a maximum magnitude of 1.5 times the incident field strength. The lateral field distribution at the green resonance shows moderate field enhancement throughout the particle responsible for part of the observed scattering signal. The normal (z-polarized) field distribution at the red resonance, on the other hand, shows a predominantly dipolar mode with a large electric field in the gap between the nanoparticle and the gold substrate. The secondary peak at 575 nm is the result of a higher order plasmon resonance of the nanoparticle with a net z-polarized dipole moment (see Appendix B.2.).

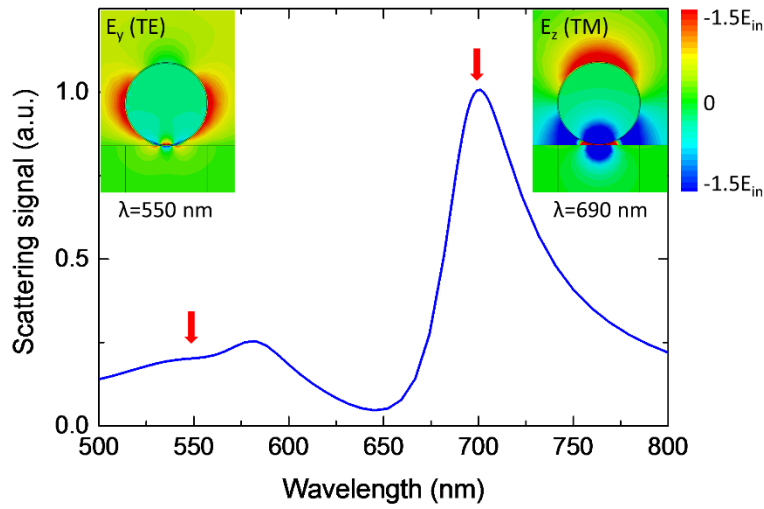


Figure 3-3: Calculated scattering spectrum of a 60 nm diameter Au nanoparticle coated with a 0.75 nm thick organic layer on a gold film. Insets show corresponding electric field snapshots at 550 nm and 690 nm under TE and TM illumination respectively, shown on the same relative scale.

Figure 3.4(a) summarizes the measured scattering peak wavelengths as a function of the Al_2O_3 thickness based on ~ 100 measured single-particle scattering spectra, as well as the corresponding simulated data. The measured data (black squares) and the simulated data for nanoparticles coated with a 0.75 nm organic ligand layer (red upward triangles) show a similar dependence on spacer layer thickness. Figure 3.4(b) presents the corresponding data sets for the relative peak scattering signal of the gold nanoparticles on each substrate. The measured scattering intensity (solid squares) exhibits relatively little variation as the spacer layer thickness is changed. This relative insensitivity of the scattering signal strength is reproduced in the simulations, both with and without the assumed presence of an organic coating on the nanoparticles. The measured

and simulated results show a very good agreement for both the peak resonance wavelength and the scattering amplitude.

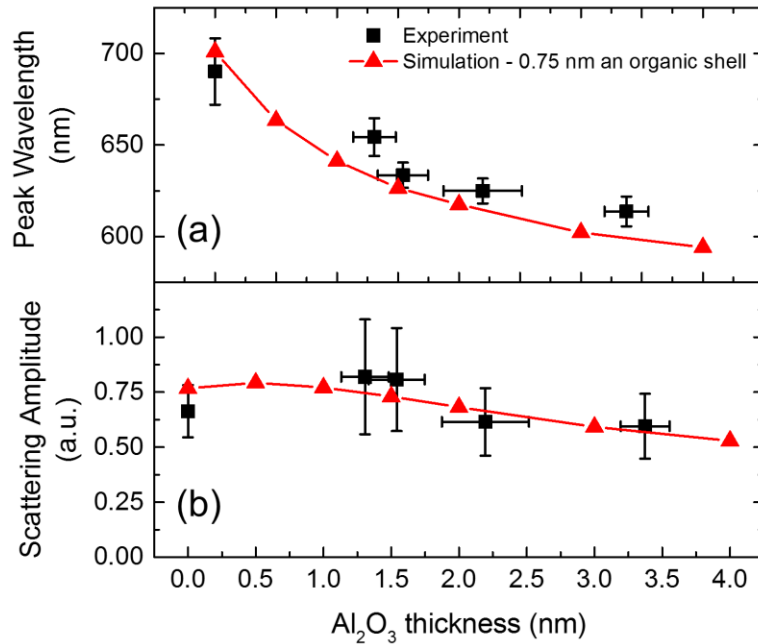


Figure 3-4: Measured and simulated scattering peak wavelength (a) and peak intensity (b) of single gold nanoparticles on a gold film with different Al_2O_3 coating thicknesses.

To evaluate the applicability of these structures to SERS-based detection of molecules on the particle surface, the enhancement of the surface-normal electric field E_z relative to the z-component of the incident field $E_{z,\text{inc}}$ was determined underneath the particle inside the 0.75 nm thick organic shell. The peak field enhancement factors $E_{z,\text{peak}}/E_{z,\text{inc}}$ range from ~ 441 to ~ 39 for the limiting cases of 0 nm Al_2O_3 and 4 nm Al_2O_3 , respectively, corresponding to predicted SERS enhancement factors $|E_{z,\text{peak}}|^4/|E_{z,\text{inc}}|^4$ ranging from 3.8×10^{10} to 2.4×10^6 . This expression for the SERS enhancement factor assumes that the detected Raman shifts are much smaller than the

plasmon linewidth [140, 141]. These calculations do not take into account effects of non-locality that are expected to reduce the field enhancement factors at small gap sizes. In addition, the listed enhancement factors would change if the particle shape changes, e.g. when the incident laser power exceeds the damage threshold of the irradiated structures. The particle stability against laser irradiation will be investigated in the following section. Note that the use of an inorganic spacer layer as done in the experiments has the added anticipated advantage that the support itself does not add Raman lines typical of organic molecular bonds, and consequently it is expected that the current structure allows for SERS measurements with relatively low Raman background signal.

Given the extreme sensitivity of the spectral position of the nanoparticle resonances to structural changes on the sub-nanometer scale, it must be verified whether these structures remain stable under typical measurement conditions in laser-excited spectroscopy such as SERS. To test the stability of the structures under laser irradiation, isolated nanoparticles were exposed to laser powers two orders of magnitude higher than those typically used in SERS of ~ 1 W/mm², and scattering spectra of the same nanoparticle were obtained before and after laser irradiation to verify spectral stability. A linearly polarized 633 nm laser beam was focused onto the substrate with the peak irradiance incident on the nanoparticles ~ 100 W/mm² for all subsequent measurements. The beam polarization was chosen to result in p-polarized irradiation of the Au nanoparticles, necessary for achieving the large gap-fields associated with the z-polarized resonance. Note that the laser wavelength is close to the z-polarized resonance wavelengths experimentally observed in this study.

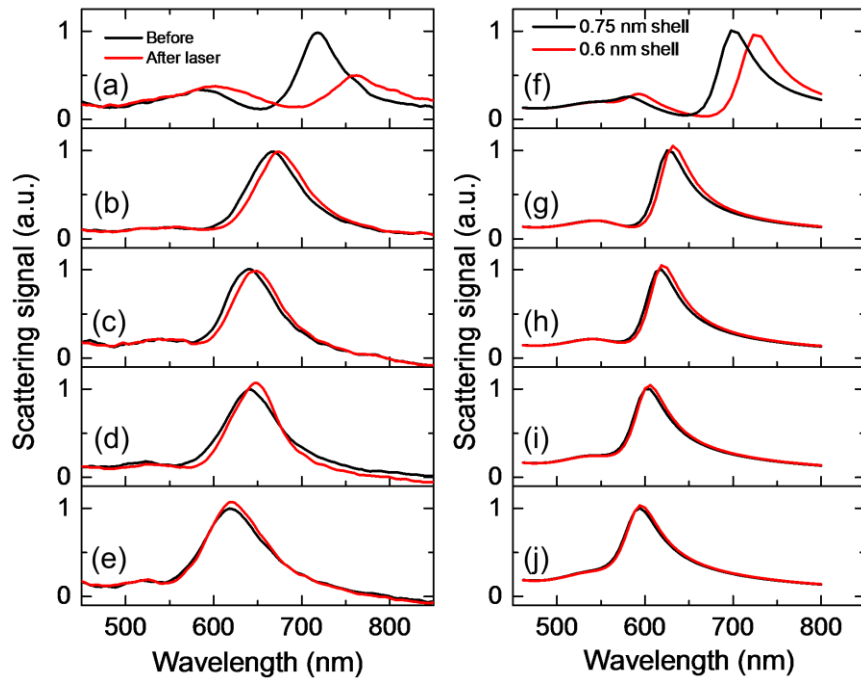


Figure 3-5: (a)-(e) Normalized scattering spectra of single gold nanoparticles on gold films coated with 0 nm, 1.3 nm, 1.5 nm, 2.2 nm, and 3.4 nm Al_2O_3 layers, respectively. The red and black curves represent the spectra before and after one minute of laser illumination at $\sim 100 \text{ W/mm}^2$, respectively. (f)-(j) Calculated scattering spectra of gold nanoparticles with (black line) and without (red line) a 0.1 nm organic shell on gold films with 0 nm, 1.5 nm, 2 nm, 3 nm, and 4 nm Al_2O_3 coating, respectively. The black and red dashed lines in (f) correspond to the same particle with a 0.6 nm and 0.5 nm organic coating, respectively.

Figure 3.5(a) shows scattering spectra of a gold nanoparticle on the gold substrate without Al_2O_3 coating before and after laser irradiation for one minute shown on the same relative scale. A significant change in the scattering spectrum is observed. Both the short and long wavelength resonance shift significantly, and the brightness of the long wavelength peak is seen to reduce

substantially. The experiment was repeated several times on separate particles, with similarly large spectral changes observed in all cases. Notably, the scattering spectra of these particles were found to be different after each successive irradiation, indicating that no stable equilibrium particle configuration was reached. Figure 3.5(b) presents the scattering spectrum of a gold nanoparticle on an Al₂O₃ coated gold substrate with a 1.3 nm Al₂O₃ thickness before and after laser irradiation. Contrary to the observations in Figure 3.5(a), the nanoparticle on the thin Al₂O₃ coating shows a relatively stable scattering spectrum. Irradiation is only seen to introduce a small (<10 nm) red-shift of the spectrum, and a slight (<8 %) increase in the peak scattering intensity. Similarly small changes in the scattering spectra were found in samples with 1.5 nm, 2.2 nm, and 3.4 nm thick Al₂O₃ coatings, as shown in Figure 3.5(c)-(e), respectively. In contrast with the observations made for particles in the absence of an Al₂O₃ coating, the spectra in Figure 3.5(b)-(e) remain stable after prolonged irradiation.

The remarkable stability of Au nanoparticles on Al₂O₃ coated Au films under high power laser irradiation is attributed to their close proximity to their equilibrium thermodynamic shape, as well as the stability of the oxide spacer layer used. Given the subtle nature of the spectral changes observed in Figure 3.5, it seems unlikely that the observed spectral shifts are the result of any major changes in the nanoparticle shape. One possible origin of the small spectral shifts is the slight modification of the particle-substrate interaction. To investigate this possibility, scattering spectra were calculated of a gold nanoparticle on the same Al₂O₃ spacer layers as in Figure 3.2 with a 0.75 nm organic shell and a 0.6 nm organic shell on the nanoparticle (black and red solid lines respectively). These simulations should be considered illustrations of the effect of sub-

nanometer changes in the effective particle-substrate separation, e.g. through slight nanoparticle deformation, changes in configuration or position of any remaining organic ligands on the Au nanoparticle surface, or the thermally stimulated removal of organic molecules from the gap region. The possibility of the thermally induced temporary removal of a surface water layer was rejected, since the red-shift persisted for minutes after the irradiation. Figure 3.5(g)-(j) show the simulated spectra for the Al₂O₃ supported Au nanoparticle different organic shell thicknesses. For each Al₂O₃ spacer layer thickness a similar effect is observed: the reduction of organic layer thickness 1.5 Å results in a slight redshift of the resonance peak. These simulated resonance shifts are slightly smaller than those observed in the corresponding experimental images (Figure 3.5(b)-(e)). Intriguingly another experimentally observed trend is reproduced remarkably well by the simulations: the experiments show that the peak scattering wavelength becomes less sensitive to laser irradiation on samples with a thicker Al₂O₃ spacer layer. This trend is reproduced in the numerical simulations while assuming an identical structural change in all cases (here represented by a 1.5 Å reduction in the organic cover layer thickness). This trend can be understood by noting that the distance dependence of the plasmon resonance becomes less pronounced at large spacer layer thickness, as observed in Figure 3.4(a). These observations support the assumption that the laser-induced spectral changes are related to small changes in particle-substrate interaction. Please note that the presented data indicate the stability against irradiation of gold nanoparticles on an Al₂O₃ coated gold substrate, however note that analyte molecules may decompose or otherwise be modified at lower irradiation powers.

Despite the good correspondence between experimental and simulated trends in Figure 3.5 for Al₂O₃-coated samples, significant differences are observed for the sample not coated with

Al_2O_3 . The results obtained with the 1.5 Å reduction in organic shell thickness show a smaller reduction in peak scattering signal and a smaller redshift than observed experimentally. The differences are possibly due to the fact that the numerical simulations ignore non-local effects [138, 139, 142] or effects related to electron tunneling expected to occur at small gap sizes [143-145]. Given these caveats the simulations of the Au film without Al_2O_3 coating do not prove that removal or modification of organic ligands are the root cause of the observed large spectral shift in Figure 3.5(a), but rather illustrate that these large spectral changes may also be explained by the type of sub-nanometer changes in particle-substrate separation assumed in Figure 3.5(g)-(j).

Several alternative hypotheses were considered to explain the observed spectral shifts observed upon laser irradiation, including significant thermally induced changes in particle shape (faceting), the formation of a finite electrically conductive contact area between particle and substrate in the case of an Au nanoparticle on the Au film, and the development of the theoretically expected contact angle of Au on Al_2O_3 upon laser irradiation. However, none of the corresponding numerical simulations led to satisfactory agreement in spectral shape and spectral location, leading to e.g. dramatically larger red-shifts or the development of pronounced multipolar resonances that were not observed experimentally. The irradiances used here are also substantially lower than those used in recent work that demonstrated particle deformation due to optical gradient forces (~100 times) [146]. We therefore conclude that the spectral changes observed here are due to minute changes in effective particle-substrate interaction, possible due to redistribution, deformation, oxidation, or removal of surface molecular layers.

3.4. Summary

In conclusion, we demonstrate wide-band plasmon resonance tuning of gold nanoparticles on thermally and chemically stable Al₂O₃-coated gold substrates. Dark-field microscopy images and hyperspectral images show well separated scattering patterns indicative of a strong z-polarized plasmon resonance. Optical spectroscopy of individual nanoparticles shows spectral tuning from 690 nm to 610 nm as the Al₂O₃ thickness increases from 0 nm to 3.4 nm. The observed tuning range of ~80 nm is three times larger than previously achieved for Au nanoparticle resonances tuned with anodized Al substrates, as the current structure does not suffer from a limiting native oxide layer thickness. Simulated scattering spectra show a good agreement with experimental observations, and the corresponding field enhancement factors suggest SERS enhancement factors well in excess of 10⁶ are possible. The scattering spectra on Al₂O₃ coated Au films were found to remain stable upon prolonged exposure to 100 W/mm² laser illumination near the nanoparticle plasmon resonance wavelength, demonstrating that this structure may be used as a reliable optical biochemical sensing platform.

4. EFFECT OF SURFACE ROUGHNESS ON SUBSTRATE-TUNED GOLD NANOPARTICLE GAP PLASMON RESONANCES

4.1. Introduction

Substrate-tuned or film-coupled metal nanoparticle systems are promising for use in plasmon-enhanced biochemical sensing applications due to their ability to provide large electric field enhancement at controlled resonance wavelengths [127, 128, 131, 147]. These structures are typically defined by depositing noble metal particles onto a metal-coated substrate, where near-field interaction between the plasmon resonant particle and free charges in the substrate lead dramatically change the optical response of the particle. Unlike plasmonic structures defined by electron beam lithography or other top-down approaches, such film-coupled nanoparticle systems are easy to fabricate, can use single-crystalline chemically synthesized metal nanoparticles, and produce a well-defined hot-spot at the gap between the nanoparticle and the substrate. Recent studies have shown that combining film-coupled nanoparticle structures with an inorganic spacer can improve their stability under laser irradiation while maintaining large field enhancement factors, making them great candidates for reliable optical sensors [130, 148]. A common method for preparing such systems involves particle deposition from colloidal suspensions onto thermally evaporated metal films. On such samples, variations in resonance frequency are routinely observed despite the use of solutions with a narrow particle size distribution. These spectral variations may be related to several factors, including nanoparticle size/shape variations in local dielectric environment, and the presence of film surface roughness. While the effect of particle size, shape variation, and local dielectric function on the particle resonances has been widely studied (see for

example ref. [7, 149-151]), the effect of surface roughness has received relatively little attention [152].

In this Chapter, we investigate the effect of surface roughness on the plasmon resonance spectra of gold nanoparticles in a substrate-tuned nanoparticle system. Single-particle scattering spectra of gold nanoparticles on a thermally deposited gold film were measured, revealing significant spectral variations. To understand these observations numerical simulations of representative local nanoscale geometries were carried out and compared with the experimentally observed spectra. The results indicates that the experimentally observed spectral variation can be understood in terms of the measured surface roughness, highlighting the importance of the film surface morphology on the reliability of substrate-tuned nanoparticle structures. These effects cannot be readily observed in ensemble measurements, but are expected to play a crucial role in determining the performance of nanoparticle based plasmonic devices.

4.2. Experiment and Simulation

4.2.1. Sample Preparation

Sample preparation involved the thermal evaporation of a 2 nm thick chromium wetting layer onto a glass cover slip (Thermo scientific) immediately followed by the thermal evaporation of a gold film. The resulting gold film thickness was measured using variable angle spectroscopic ellipsometry, and was found to be 48.7 ± 0.5 nm. The root mean square film roughness of the film was found to be ~ 1 nm as measured using tapping-mode atomic force microscopy (AFM). The

substrate was then incubated in a 10^{-3} mol/L 4-methylbenzenethiol (4-MBT, Sigma Aldrich) solution in ethanol for two hours. Subsequently the substrate was thoroughly rinsed with ethanol and dried using compressed air. This procedure produces a self-assembled monolayer of 4-MBT molecules on a gold film [153-155], representative of a typical Surface Enhanced Raman Scattering (SERS) test structure. Gold nanoparticles were deposited onto the substrate by incubating the substrate for 10 minutes in an 80 nm gold nanoparticle solution (BBInternational, batch-specific mean diameter of 80.7 nm with size variation $2\sigma < 7.8\%$) diluted in ethanol to a concentration of 5×10^8 particles/mL. The substrate was subsequently rinsed with ethanol and dried using compressed air. The method resulted in a low particle areal density enabling single particle spectroscopy.

4.2.2. Microscopy and Spectroscopy

Optical microscopy and single particle spectroscopy of gold nanoparticles on the gold films were carried out using an inverted microscope (Olympus IX71). A Canon EOS 450D digital camera was used for image capture, and an imaging spectrometer attached to the microscope (Horiba iHR320 with Synapse CCD array) was used for single particle spectroscopy. Scattering spectra were obtained using a 50 \times dark field objective with an illumination angle of $\sim 77^\circ$ (Olympus UMPlanFl 50 \times BD, N.A.=0.75). The scattered light from the particle was collected by the same objective and sent to either the camera or the spectrometer. For spectroscopy, the collection area was set to be $6 \mu\text{m} \times 2.6 \mu\text{m}$ by limiting the spectrometer entrance slit width and using vertical binning of the recorded CCD data. The spectral resolution in all measurements was

6 nm. Single-particle scattering spectra I_{sc} were obtained by using the relation $I_{sc}=(S-R)/R$, where S and R were the collected signal from an area containing a nanoparticle and a nearby region without nanoparticles, respectively. The subtraction removes any background signal related to scattering from the substrate. The obtained scattering spectra were peak-normalized to facilitate comparison.

4.3. Results and Discussion

Figure 4.1(a) shows a darkfield microscopy image of a representative area of the sample, showing sparsely distributed gold nanoparticles on the gold film. The particles exhibit similar scattering color and intensity, with most particles producing a red ring and a weak central green spot as seen in the insets in Figure 4.1 (a). These features are known to correspond to scatterers with a low-frequency (red) vertical scattering resonance and a high-frequency (green) predominantly lateral scattering component [148]. Figure 4.1(b) presents peak-normalized single particle scattering spectra from 21 randomly selected gold nanoparticles on the gold film. The spectra were approximately sorted by peak scattering energy to facilitate comparison between spectra. The vertical dashed line indicates the average peak resonance energy of the scattering spectra at 1.67 eV (745 nm). The vertical dotted lines represent the statistical variation in peak position spanning two standard deviations on each side ($\pm 2\sigma = \pm 63$ meV). Spectral variation of this magnitude could significantly affect the performance and reliability of this substrate-tuned nanoparticle plasmonic system when used e.g. as a SERS substrate.

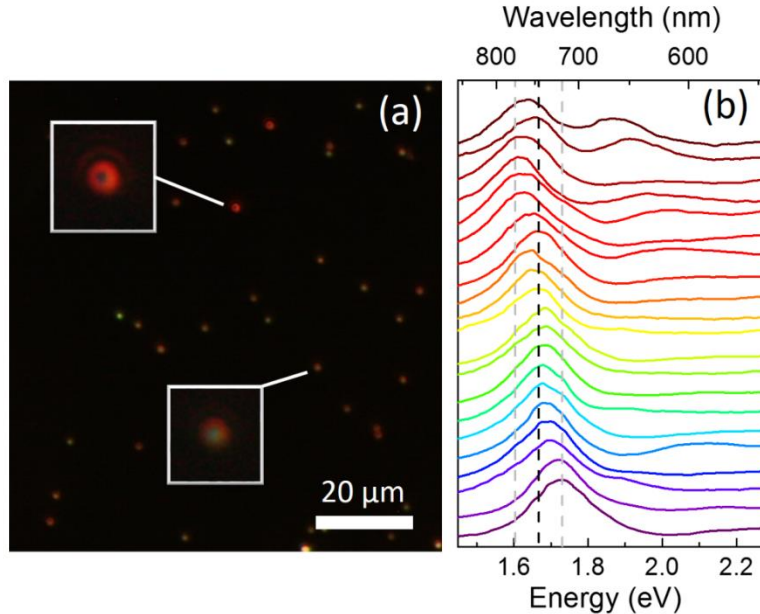


Figure 4-1: (a) A darkfield microscopy image of gold nanoparticles on a gold film. The insets show a magnified view of two representative particles. (b) Peak-normalized single particle scattering spectra from randomly selected gold nanoparticles.

To trace the origin of the observed spectral variations, we first consider the effect of surface roughness on single particle scattering spectra by simulating representative geometries. This is a challenging issue: due to the largely random nature of the surface roughness, each particle is situated in a slightly different local environment. In order to find representative geometries based on the surface morphology as measured by AFM, it was assumed that the liquid-based particle deposition places the particles at local height minima. Possible particle locations were found using a numerical algorithm that extracted the lowest geometrically possible z-position of an 80 nm diameter nanosphere at each lateral position of the AFM scan. Each local z-minimum from this data set was considered to be a possible particle location after deposition. Figure 4.2(a) shows the

AFM image of the gold film used in this analysis. Figure 4.2(b) shows a zoomed-in perspective of the sample surface at a randomly selected local minimum, with the outline of an 80 nm diameter gold nanoparticle superimposed at the corresponding local z-minimum. Note that the measured local curvature of the gold film is similar to the known curvature of the gold nanosphere, implying that surface roughness can significantly affect the particle-substrate separation in the important junction region underneath the particle. Since the particle locations considered here represent local minima, the particle may have either one or three contact points with the substrate at these locations. In the case of one contact point the particle is separated from the metal film only by the thickness of the 4-MBT layer, while in the case of three contact points, an air gap may form directly underneath the particle. As will be shown below, the variation in this particle-substrate gap is a key factor in determining the variability in nanoparticle resonance spectra in substrate-tuned nanoparticle systems with finite surface roughness.

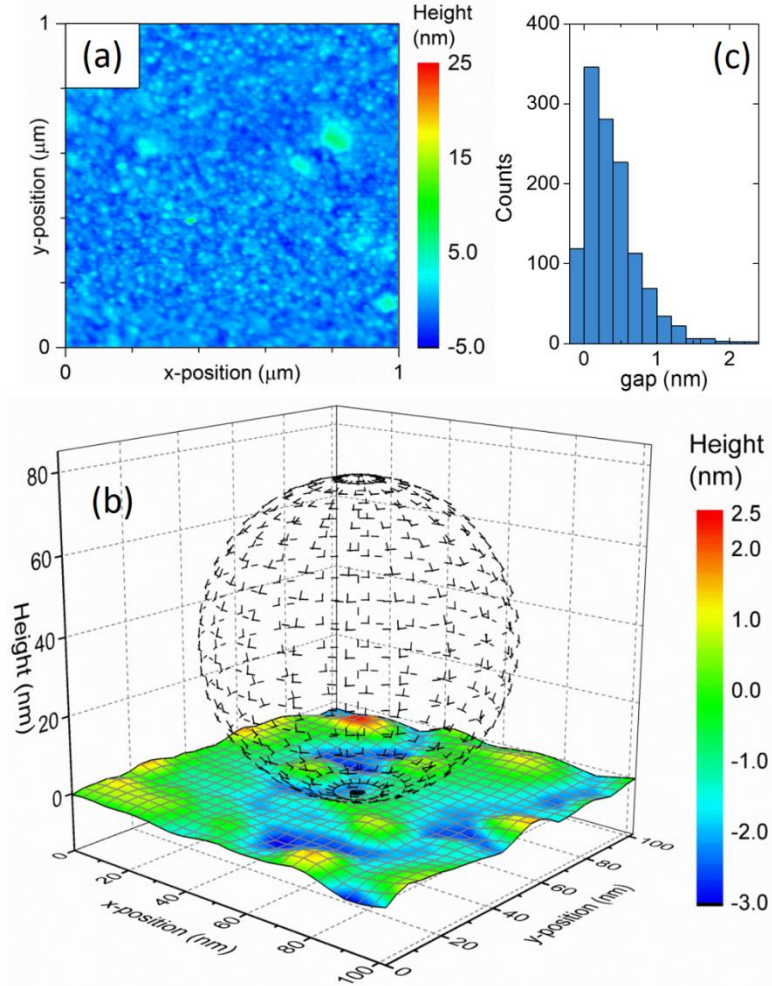


Figure 4-2: (a) AFM image of a gold film thermally evaporated on glass. (b) Example surface geometry near a liquid-deposited gold nanoparticle deposited on top of the surface shown in (a). (c) Normalized gap size histogram from over 1,200 possible particle locations.

To determine whether gap size variation could account for the amount of spectral variation observed in the experiments, the geometrically predicted gap size was extracted for all possible particle positions obtained from the AFM data. Figure 4.2(c) shows the gap size histogram obtained from analyzing over 1,200 local particle height minima. The data is displayed at a bin

size of 2 Å where the first bin extending from -2 Å to 0 Å represents particle positions that produce zero gap size (single contact point). A key point to note is that only 10% of the particle locations produce zero gap size, suggesting that most deposited particles deposited randomly on this substrate will not have a contact point directly underneath the particle. While the obtained gaps and gap size variations are small, they can cause substantial variations in peak scattering wavelength.

To convert the gap sizes in Figure 4.2(c) to predicted scattering spectra, representative geometries with a single contact point as well as geometries with three contact points and varying gap sizes were considered. The nanoscale local particle environment was modeled by defining three spherical protrusions on a gold film, arranged in an equilateral triangle and separated by a distance P as shown in Figure 5.3(a). The gold film is assumed to be covered by a 0.5 nm thick layer of 4-MBT molecules, corresponding to the molecule used in the surface preparation. Based on the known surface morphology from the AFM data the protrusions were chosen to have a radius of curvature (R_p) of $0.8R_{NP}$ and separation (P) of 25 nm respectively. This choice of P corresponds to the most prevalent spatial frequency present in the measured AFM scan of the gold surface, while the curvature of the protrusions is similar to typical surface curvature values throughout the AFM scan. Different gap sizes (d) are achieved by varying the z-position of the protrusions. A side view of the resulting surface structure is shown in Figure 4.3(b), corresponding to the plane marked by the vertical dashed line in Figure 4.3(a). Figure 4.3(c) shows a perspective of one of the used geometries with an 80 nm diameter nanosphere superimposed.

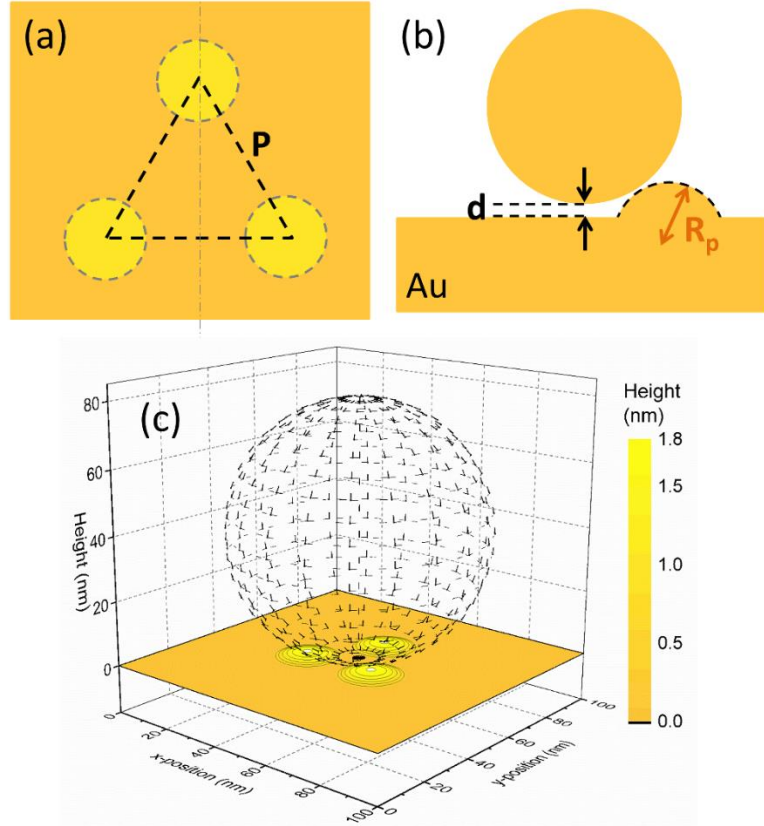


Figure 4-3: Schematic of a representative simulation geometry and relevant parameters showing
 (a) a top view without a gold nanoparticle showing three protrusions, (b) a side view along the
 dashed line in (a) with a deposited gold nanoparticle present, and (c) a perspective view of the
 final structure.

The optical response of representative geometries was simulated using the three-dimensional frequency domain finite integration technique [29], following the method described in Chapter 2. Briefly, a simulation volume of $240 \times 240 \times 310$ nm³ was illuminated with a p-polarized electromagnetic wave at an angle of incidence of 77°, corresponding to the illumination angle used in the experiment, and the scattering spectrum is obtained from the dipole moment of

the nanoparticle. The dielectric function of gold was taken from the literature [115] and the refractive index of the molecular layer was assumed to be 1.55. The laterally polarized dipole component which is responsible for the green scattering spot was not considered in this calculation due to its small contribution to the main resonance peak. Figure 4.4(a) shows the simulated normalized scattering spectrum associated with the z-polarized dipole moment of a gold nanoparticle on a flat gold film. The spectrum shows a main z-polarized scattering peak at an energy of 1.59 eV (781 nm), somewhat lower than the typical spectral position of the main resonances in Figure 4.1(b). A snapshot of the surface-normal field component is included for excitation at the peak wavelength as indicated by the arrow. Figure 4.4(b) shows the corresponding results for a gold nanoparticle on a corrugated surface with $d=0$ (dashed line). The corrugation is seen to cause a small red-shift of the main peak to 1.58 eV (786 nm) compared to the results in Figure 4.4(a). The solid line shows the results for a corrugated structure with $d = 0.39$ nm (solid line), corresponding to the average gap size obtained from Figure 4.2(c). The introduction of a 0.39 nm gap is seen to cause a significant blueshift of the main resonance peak to 1.71 eV (727 nm), close to the average resonance peak position of 1.67 eV in the experiment. A snapshot of the surface-normal field distribution at this gap size is included for the peak wavelength as indicated by the arrow. The simulated scattering spectra at zero gap show clear secondary peaks at higher energy, which based on field snapshots (not shown) are attributed to higher order gap modes. Evidence for such modes appears to be present in several of the experimental spectra in Figure 4.1(b), and intriguingly they indeed appear most prevalent in spectra with low-frequency main peaks. Based on the results presented in Figure 4.4 it is clear that realistic changes in local surface geometry can produce spectral variations of a magnitude similar to those observed experimentally.

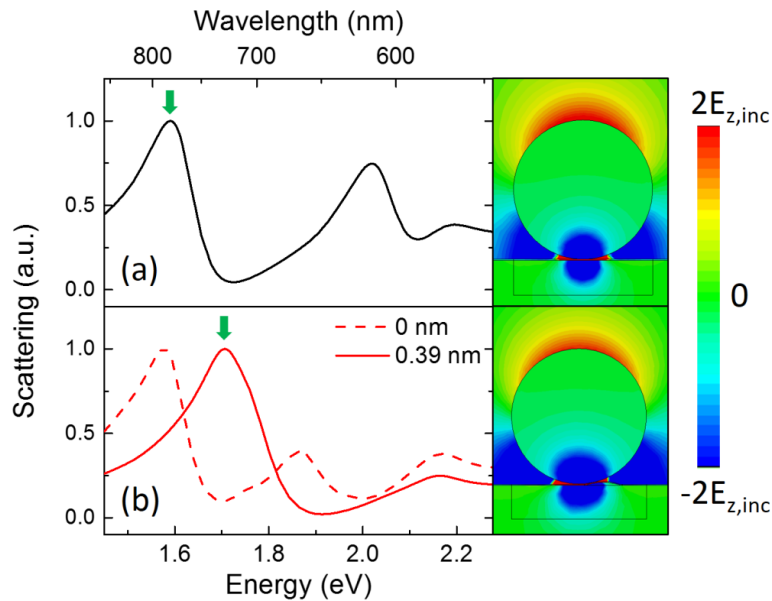


Figure 4-4: Normalized scattering spectra of a gold nanoparticle (a) on a flat gold film and (b) on a corrugated gold surface with $d = 0$ (dashed line) and $d = 0.39$ nm (solid line). The field-plots show two-dimensional electric field distributions at the main resonance peak of the spectra as indicated by the green arrows.

While the presented simulations demonstrate that roughness-related gap-size variations can account for the observed spectral fluctuations, the known particle size distribution in the used colloidal nanoparticle solution could also play a role. To investigate this possibility, particle-size dependent scattering spectra were calculated. Figure 4.5(a) shows a contour graph of the simulated scattering spectra of gold nanoparticles with a diameter in the range 73.76 nm to 86.24 nm, deposited on a flat gold surface. This range matches the known 2σ particle size variation from the experiment. The main resonance energy of each simulated spectrum is marked by a black square for clarity. For comparison the horizontal black dashed line indicates the average resonance energy

obtained from the measured scattering data, and the grey dashed lines correspond to the experimentally determined $\pm 2\sigma$ variation. The black solid line represents a linear fit to the simulated peak positions. All spectra show a strong low-frequency peak with a small redshift compared with the experimentally observed resonance wavelength as well as a short wavelength peak previously attributed to a higher order gap resonance. As the particle size is increased, a small redshift of the main resonance is observed. Based on the known size variation and the size-dependent simulated scattering spectra, an average resonance energy of 1.59 eV and a 2σ spectral variation of ± 17.5 meV are predicted, as indicated by the blue circle and its energy error bars. These values are notably smaller than the spectral variation observed in the experiments, demonstrating that particle size variation alone is not sufficient to explain the experimental results.

To quantitatively compare the measured and predicted spectral variations related to surface roughness effects, simulations of the rough surface with different gap sizes were carried out. Figure 4.5(b) shows a contour graph of the scattering spectra of 80 nm diameter gold nanoparticles on a rough surface with $R_p = 0.8R_{NP}$ and $P = 25$ nm as a function of gap size. The black solid line represents an empirical fit to the data. As the gap size is increased the low-energy peak in the scattering spectra blueshifts from 1.58 eV to 1.74 eV. This simulated gap-size-dependence of the main scattering peak was used to convert the gap size histogram (Figure 4.2(b)) to a resonance energy histogram. The thus obtained average resonance energy of 1.68 eV is shown as a blue circle in Figure 4.5(b) while the error bar of ± 105 meV shows the predicted 2σ variation. The predicted resonance energy and variation agree reasonably well with those of the measured spectra which show an average resonance at 1.67 eV and $2\sigma=63$ meV.

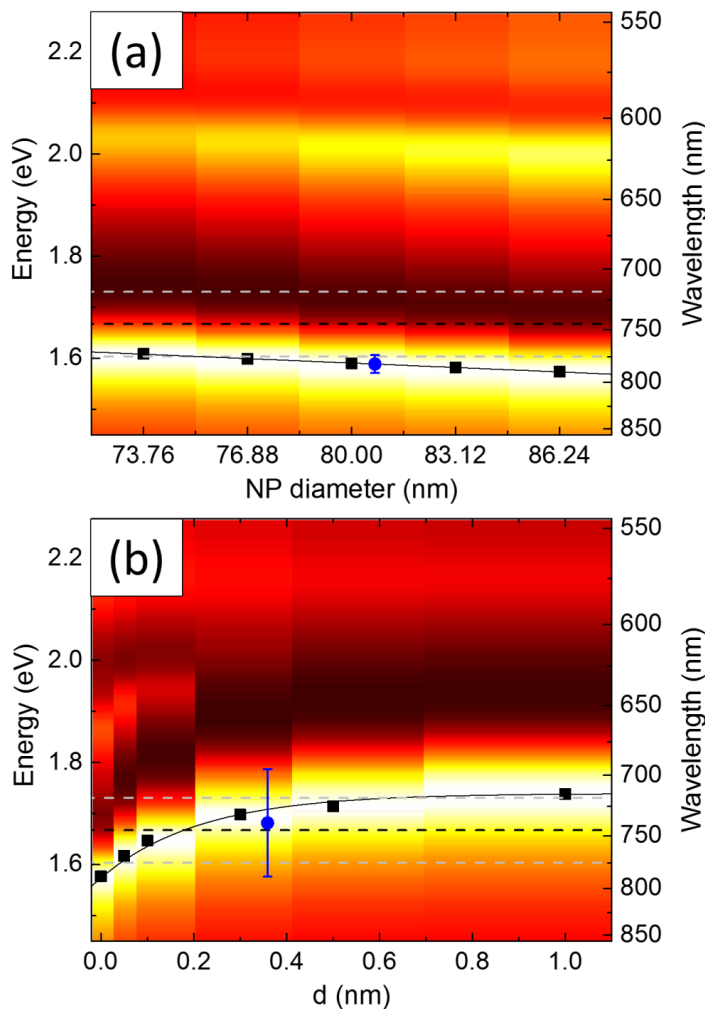


Figure 4-5: (a) Contour graph of the scattering spectra of gold nanoparticles with different sizes on a flat gold film. (b) Contour graph of the scattering spectra of an 80 nm diameter gold nanoparticle on a rough surface as a function of air gap size d . The black dashed line represents the average resonance energy from the experiment and the two grey dashed lines span 2σ on each side. The black squares mark the main peak positions and the solid lines show empirical fits to the peak position. The blue circles represent experimentally expected spectral positions and variations based on numerical simulations.

The numerical simulations demonstrate that a typical roughness of ~ 1 nm on a thermally evaporated gold film is sufficient to significantly affect the substrate-tuned resonance of 80 nm diameter particles. This is a consequence of the fact that plasmon resonances on supported nanoparticles evolve into gap plasmons at small particle-substrate separations, making the resonances extremely sensitive to the exact nanoscale geometry near the particle-substrate junction. The effect of local geometry is expected to be slightly less pronounced when taking into account nonlocal effects, where are known to lead to a blueshift in the gap resonance frequency and a weaker dependence of resonance wavelength on small gap sizes [139]. Finally, it should be pointed out that some of the observed effects could be avoided by using alternate substrate preparation techniques that minimize surface roughness, including template stripping [156] or the use of chemically synthesized single-crystal gold films [157].

4.4. Summary

This chapter presents the effect of surface roughness on the plasmon resonance of gold nanoparticles on a gold film. The surface roughness of a thermally evaporated gold film was shown to have a significant effect on the average resonance wavelength and on spectral variation. This is attributed to the statistical nature of the formation of the local environment of randomly deposited gold nanoparticles. The study demonstrates the importance of surface roughness in substrate-tuned nanoparticle structures, and suggests that the achievement of consistent resonance frequencies and field enhancement factors with deposited nanoparticles necessitates the use of specialized substrates with minimal surface roughness.

5. GAP-PLASMON ENHANCED GOLD NANOPARTICLE PHOTOLUMINESCENCE

5.1. Introduction

The first observation of gold photoluminescence (PL) was reported in 1969 by Mooradian who observed a broad unpolarized emission spectrum with an emission peak at ~500 nm. These findings were attributed to radiative recombination of holes in the *d*-band with electrons in the *sp*-band [70] with an estimated emission quantum efficiency of the order of 10^{-10} . In 1986 Boyd *et al.* developed a detailed model describing the photoluminescence from roughened metal films in terms of band structure and field enhancement factors. By describing the rough surface as a random collection of grounded nanoscale hemispheres and considering the field enhancement at the excitation and emission wavelengths, good agreement between measured and experimental photoluminescence data was obtained [158]. Since those early observations advances in nanofabrication have enabled the systematic investigation of photoluminescence from large collections of gold nanostructures. Such ensemble measurements revealed unusually strong PL signal which unlike that observed in bulk gold shows emission peaks that correlate with plasmon-related peaks in the extinction spectra, suggesting that surface plasmons are involved in the emission enhancement [71-75]. More recently, advances in microscopy and spectroscopy techniques have enabled the investigation of the PL response of individual gold nanostructures. These single-particle studies demonstrated a close correlation between the PL spectra and their scattering spectra, and confirmed the increase in PL quantum yield compared to bulk gold [159-163]. Moreover, it was observed that the enhanced PL from anisotropic gold nanostructures results

in emission with a polarization angle aligned with the polarization direction of a spectrally matched plasmon resonance, even when the structure is excited at frequencies far from the resonance [163-165]. Most studies describe the enhancement in terms of a plasmon-enhanced *e-h* pair generation rate and a plasmon-enhanced radiative recombination efficiency, both associated with the enhanced local electric fields that occur near the plasmon resonance frequency. In addition it has recently been proposed that excitation of high-angular-momentum plasmons can become a major nonradiative *e-h* recombination channel for holes located near the metal surface [166]. Despite the general agreement on the main contributing factors to the fluorescence enhancement, few studies quantitatively analyze these effects at the single particle level [72-75, 162-165].

A plasmonic system that recently received a significant amount of attention is the film-coupled nanoparticle system. Metal particles deposited on metallic or highly polarizable substrates or films exhibit resonances that are strongly localized near the gap between the particle and the substrate. The field enhancement provided by such gap-plasmons can significantly exceed that of individual nanosphere resonators, and it has been used in plasmon-mediated optical sensing applications including the detection of local chemical reactions [167] and surface enhanced Raman scattering of molecules [66, 109, 128, 147]. This structure is also of interest due to its ability to generate energetic electrons and holes in the important junction region of a nanoparticle with a dielectric-coated substrate, which may have applications in plasmon enhanced (internal) photoemission and plasmon mediated photocatalysis [78, 85, 86, 168]. In addition, film-coupled nanoparticles offer several advantages over other coupled plasmonic resonators that support gap plasmons. These include their ease of fabrication, their highly reproducible optical response, their

structural stability, and their wideband spectral tunability through variation of the particle-substrate separation [130, 148, 169]. These factors make film-coupled nanospheres a promising platform for the quantitative analysis of plasmon enhanced gold photoluminescence and related electronic effects. The present study uses a combination of single particle scattering spectroscopy and single particle multi-wavelength excited photoluminescence spectroscopy to determine the magnitude and physical origin of the gold PL enhancement by gap plasmons. A numerical approach is presented that achieves quantitative agreement between the observed and modeled PL enhancement spectra. We show a maximum measured PL enhancement factor as high as 28000 at the gap mode resonance wavelength, relative to the PL signal obtained from a planar gold film with an area equal to the physical cross-section of the nanoparticle.

5.2. Experiment and Simulation

5.2.1. Sample Preparation

An Al_2O_3 coated gold film was prepared by thermal evaporation using a multipocket Edwards FL 400 thermal evaporator. A 2 nm thick chromium wetting layer was deposited onto a glass cover slip (Thermo scientific), immediately followed by the thermal evaporation of a 50 nm gold film. A few-nanometer thick aluminum layer was deposited on the gold layer without breaking vacuum. The aluminum film completely oxidizes into an Al_2O_3 layer after exposure to air. The Al_2O_3 thickness was measured using variable angle spectroscopic ellipsometry, and was found to be 3.4 nm. Gold nanoparticles were drop-coated on the substrate and left to dry in air

from an ethanol-diluted monodispersed gold nanoparticle colloidal solution (BBInternational) with a particle diameter of 80.7 nm (size variation $\sigma < 3.9\%$).

5.2.2. Single Particle Microscopy and Spectroscopy

Optical microscopy and spectroscopy were performed on an Olympus IX-71 inverted microscope equipped with standard dark field optics using a 50 \times dark field objective (Olympus UMPlanFl 50 \times BD, collection N.A. = 0.75, 77° illumination angle). Dark field images and single particle spectra were recorded using a Canon EOS 450D digital camera and an imaging spectrometer (Horiba iHR320 spectrometer equipped with Andor DU401-BR-DD CCD camera), respectively. The large inter-particle separation allows for the spatial selection of individual nanoparticles for spectroscopy by limiting the spectrometer entrance slit width and using vertical binning of the recorded CCD data (collection area $\sim 6 \times 4 \mu\text{m}^2$). All spectra were collected with a 10 second exposure time and corrected for the detector dark current. The raw spectra were averaged over 18 pixels to match the optical spectral resolution of 10 nm. The scattering spectrum of gold nanoparticles was obtained by collecting the scattered signal from the particle (I_{NP}), subtracting the scattered signal from a nearby area without a nanoparticle (I_{ref}), and dividing by the latter, corresponding to the formula $I_{scat} = (I_{NP} - I_{ref})/I_{ref}$.

5.2.3. Photoluminescence Measurement

For single-particle PL measurements each nanoparticle was aligned to the center of the laser spot using a three-axis piezo-controlled sample stage. The reflected laser beam was blocked

using a beam stop and any remaining Rayleigh scattered laser light was suppressed using a 550 nm long pass filter in the case of 532 nm excitation and a notch filter in the case of 633 nm excitation. Photoluminescence spectra were recorded under 100 uW continuous wave irradiation with the same collection system as used in the scattering spectroscopy but using a 60 second integration time and $\sim 6 \times 10 \mu\text{m}^2$ collection area. All spectra were corrected for the detector dark current and the grating and detector spectral response functions.

5.2.4. Numerical Simulation and Calculation

Frequency domain full field electromagnetic simulations were carried out using CST Microwave Studio [29] assuming a unit cell boundary condition with a lateral cell size of 240 nm \times 240 nm. Plane waves with TE and TM polarization were used as the excitation sources. Simulated electric field distributions at an angle of incidence of 77° and 35° were used to calculate the gold particle scattering spectrum and PL enhancement spectrum, respectively. Literature data were used for the dielectric functions of gold [115] and Al₂O₃ [114]. The scattering spectrum of a gold nanoparticle was calculated using the method described in Ref. [148]. Briefly, the calculated electric fields in the particle and the gold film were first used to calculate the total electric dipole of the structure (μ). The scattering spectrum is assumed to be proportional to the dipole radiation power $I_{\text{scat}} \propto \omega^4 |\mu|^2$. [1] The PL spectrum from gold in the simulated structure was obtained based on the simulated electric field distributions by integrating Eq. (4-2) throughout the gold volume.

5.3. Results and Discussion

Figure 5.1(a) shows a dark-field microscopy image of the gold nanoparticles sparsely distributed on the Al₂O₃ coated gold film. The film-coupled nanoparticles predominantly scatter red light and appear ring-shaped, characteristic of a vertically polarized gap mode plasmon resonance [42, 127, 130]. Figure 5.1(b) presents the peak-normalized measured scattering spectrum I_{scat} (solid line) of the nanoparticle highlighted by the white circle in Figure 5.1(a). The scattering spectrum has a strong resonance peak at ~650 nm with a full width at half-maximum (fwhm) of ~68 nm, and a small shoulder at a wavelength of ~550 nm. Spectral measurements on several other particles reveal typical variations in peak scattering wavelength on the order of ±10 nm. For additional representative spectra see Appendix C. Numerical simulations of the scattering spectrum were carried out to identify the modes responsible for the features in the experimental scattering spectrum. Figure 5.1(c) shows the simulated scattering spectrum of an 80 nm diameter spherical Au nanoparticle on a gold film coated with a 2.8 nm Al₂O₃ film, close to the experimentally determined Al₂O₃ thickness. The simulations reproduce the experimentally observed scattering peak position of 652 nm, as well as the presence of a secondary peak at shorter wavelength. Figures 1d and 1e show the simulated distribution of the electric field magnitude at 550 nm and at 652 nm, respectively, shown on the same scale. The main resonance peak at 652 nm is seen to correspond to a highly confined plasmon mode with most of the field concentrated near the gap between the particle and the gold film (gap plasmon) [127]. At this frequency the peak field amplitude inside the gold particle exceeds the incident field strength by a factor 17 under TM illumination. The electric field distribution under 550 nm excitation shows the presence of a

higher order resonance with lower overall field enhancement than the main resonance. This mode appears relatively prominent in the simulated scattering spectrum in Figure 5.1(c) compared to the experimental results. This difference may be due to the fact that the simulations do not take into account the nonlocal nature of the metal dielectric function, which is known to suppress modes exhibiting significant field variation over a typical distance v_f/f with v_f the Fermi velocity and f the plasmon resonance frequency through a process known as Landau damping [170]. In gold at 550 nm this distance is 2.5 nm, which is indeed comparable to the spatial field variation near the gap of the electric field distribution at 550 nm in Figure 5.1(d).

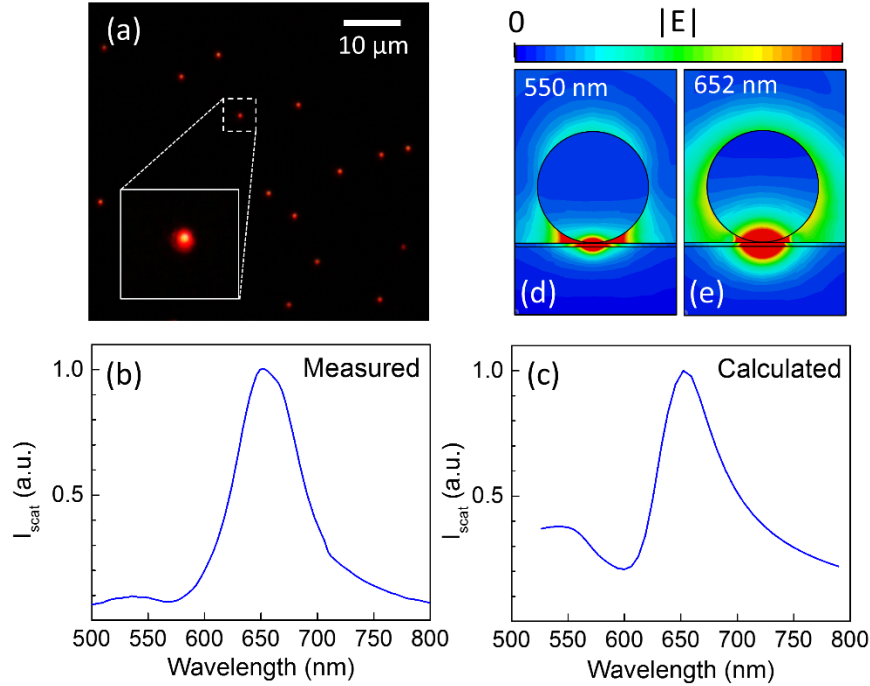


Figure 5-1: (a) Dark field microscopy image of 80 nm diameter gold nanoparticles on an Al₂O₃ coated gold film. (b and c) Measured and simulated scattering spectra of the gold nanoparticle highlighted in (a). (d and e) The simulated distribution of the electric field magnitude under illumination at respectively 550 nm and at 652 nm TM at an angle of incidence of 77°.

Photoluminescence measurements of individual gold nanoparticles were carried out using continuous wave excitation at either 532 nm or 633 nm. The experimental setup is shown schematically in Figure 4.2(a). A 100 μW laser beam (532 nm or 633 nm) is sent into the microscope via a laser port and directed off-center to the microscope objective, leading to p-polarized illumination at the sample surface at a measured angle of incidence of ~35°. The fwhm of the laser spot at both wavelengths was determined to be ~2.8±0.2 μm using the nanoparticle-mediated beam sampling method described in Ref. [148]. This excitation geometry provides the

surface-normal electric field component needed to excite the gap mode on the Au nanoparticles. This is illustrated by the simulation results in Figure 5.2(b) and (c), showing a snapshot of the z-component of the electric field under *p*-polarized excitation respectively at 532 nm and 633 nm at an angle of 35°, scaled to the same field value. These excitation wavelengths are close to the gap mode resonance wavelengths, and indeed in both cases the excited field distribution is seen to be strongly confined in the gap. Note that the mode excited at 532 nm exhibits a higher spatial frequency along the particle perimeter and lower internal field strength compared to the mode excited at 633 nm.

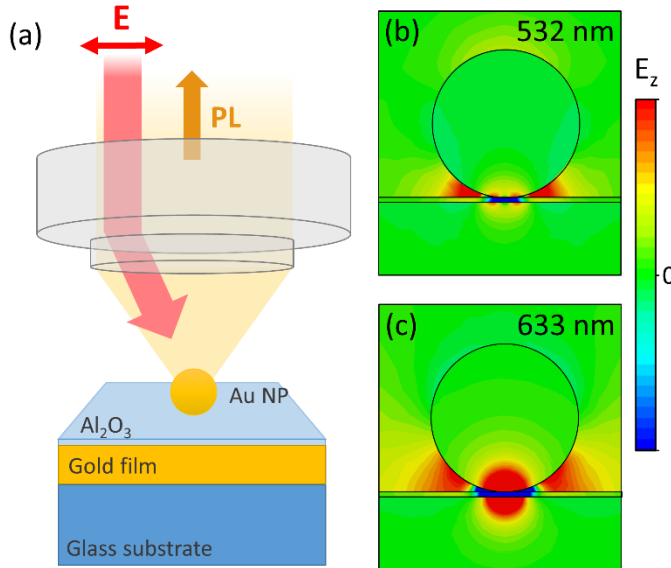


Figure 5-2: (a) The experimental configuration for single-particle photoluminescence spectroscopy. (b and c) Snapshots of the simulated electric field distributions respectively under 532 nm and at 633 nm excitation at a 35° angle of incidence.

Figure 5.3(a) shows gold photoluminescence spectra collected under 532 nm excitation, obtained from the sample shown in Figure 5.1(a). The dark green line shows the signal when exciting a region of the gold film not containing a nanoparticle, resulting in a broad featureless emission spectrum with a short-wavelength onset governed by the long-pass filter used to suppress Rayleigh scattering. This emission is commonly attributed to the excitation of d -band electrons to the sp -band followed by radiative carrier recombination [158, 171]. Based on the absorbed laser power, the collection efficiency, and the integrated photon count the quantum efficiency of the detected photoluminescence is estimated to be 3×10^{-10} . This matches typical numbers reported in the literature, providing further evidence that the collected signal originates from the gold film

[70]. The bright green line in Figure 5.3(a) shows the PL signal collected when the nanoparticle highlighted in Fig. 1a is moved into the center of the excitation spot. In this case a similar broad luminescence background is present, however additional signal appears near the nanoparticle gap mode resonance wavelength, resulting approximately in a doubling of the PL signal at 660 nm. Remarkably, this signal doubling is achieved using a particle that has a physical cross section three orders of magnitude smaller than the laser spot area, see the left sketch in Figure 5.3(a). Figure 5.3(b) shows the corresponding data under 633 nm excitation. In this case the signal from an area not containing a nanoparticle (dark red line) is again broad and featureless, but a factor 2.4 weaker than when excited with green light. This reduction in signal is attributed to the fact that at this lower excitation energy fewer interband transitions are available, as evident from the Au band structure and the Au dielectric function, leading to a reduced e - h pair generation rate. Note that the spectrum shows a narrowband dip near the laser line. This is caused by the response of the notch filter that was used to suppress Rayleigh scattering of the excitation laser. The PL signal from the area containing the nanoparticle (bright red line) is remarkably strong under 633 nm excitation, exceeding the corresponding background signal by a factor \sim 16 at the main gap-plasmon resonance wavelength. The nanoparticle (NP)-enhanced PL emission appears to have a different spectral shape under different excitation conditions, which is largely due to the different relative contribution of NP-mediated PL and the Au film PL background in these two cases; see Appendix C. No experimental evidence was found for photoluminescence excited via propagating surface plasmon polaritons on the gold.

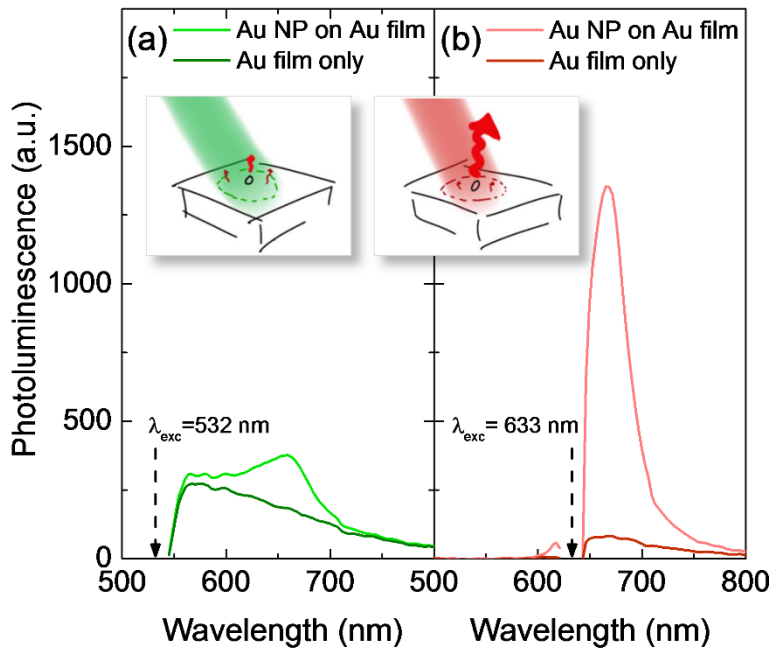


Figure 5-3: Photoluminescence spectra collected under 532 nm excitation (a) and 633 nm excitation (b) from areas containing a gold nanoparticle (bright green and bright red lines) and no gold nanoparticle (dark green and dark red lines). The insets schematically show that a gold nanoparticle adds PL signal at the particle resonance wavelength (red arrows) to the weak background PL.

To investigate the nanoparticle PL enhancement quantitatively we define a photoluminescence enhancement factor g_{PL} as

$$g_{PL}(\lambda_{exc}, \lambda_{em}) = \frac{I_{NP} - I_{film}}{I_{film}} \frac{A_{eff}}{\sigma_{NP}} \quad (5-1)$$

where I_{NP} is the PL signal collected when illuminating an area containing a particle, I_{film} is the signal collected from a substrate area away from the particle, A_{eff} is the effective laser spot area defined as $A_{eff} = \pi R_{1/e}^2$ with $R_{1/e}$ the spot radius at 1/e of the peak irradiance, and σ_{NP} is the physical cross-section of the NP. With this definition, the enhancement factor represents the PL signal added by the presence of the particle, relative to the PL signal from a substrate area with a size equal to the physical cross-section of the particle excited at the same irradiance. This enhancement factor is independent of the laser spot size, does not depend on the intrinsic wavelength-dependent $e-h$ generation efficiency, and does not depend on the intrinsic wavelength dependent emission efficiency. Figure 5.4(a) shows the experimentally obtained PL enhancement spectra g_{PL} for the gold nanoparticle highlighted in Fig. 1a excited with 532 nm and 633 nm laser beams (green and red solid lines, respectively), based on the curves in Figure 5.3 and the measured laser spot sizes. For comparison the peak-normalized scattering spectrum of the particle has been included (black dashed line, right axis). Several features should be noted. First, the maximum PL enhancement occurs close to the main plasmon resonance wavelength of the nanoparticle. Second, the shape of the enhancement spectrum appears identical for the two excitation wavelengths. Third, the overall enhancement factors achieved under 633 nm excitation are approximately an order of magnitude larger than under 532 nm excitation. These observations reproduce quantitatively when using a different particle on the same sample (see Appendix C). The largest enhancement is achieved near

the gap mode resonance under excitation near the resonance frequency, showing a peak enhancement factor of 28000.

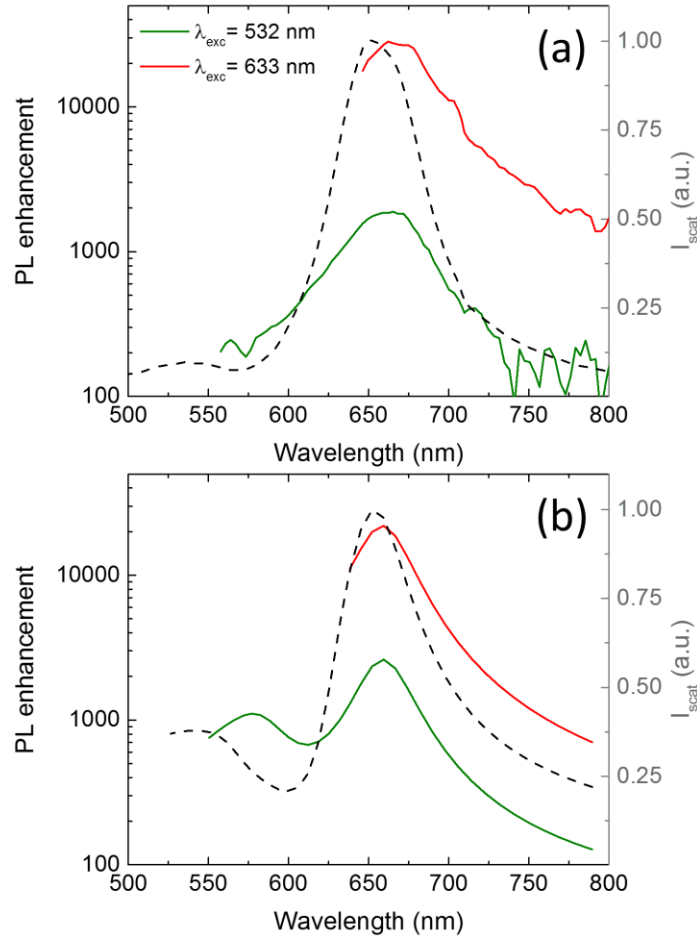


Figure 5-4: The measured (a) and calculated (b) photoluminescence enhancement spectra g_{PL} for a gold nanoparticle excited with 532 nm (green solid lines) and 633 nm (red solid lines) laser lines. The black dashed lines show the measured and calculated peak-normalized scattering spectra of the particle.

To understand the observations in Figure 5.4, we quantitatively model the photoluminescence enhancement factor by evaluating the nanoparticle-induced changes in *e-h* generation rate and emission efficiency based on simulated electric field distributions. The electron-hole pair generation rate in a volume element dV inside gold is proportional to $\varepsilon''_{IB} |\vec{E}_{TM}(\vec{r}, \omega)|^2$ where ω is the angular frequency of the excitation source, $\varepsilon''_{IB}(\omega)$ is the part of the imaginary dielectric function related to interband transitions at the excitation frequency, and $\vec{E}_{TM}(\vec{r}, \omega)$ is the simulated field distribution under TM excitation at the experimental angle of incidence (see Figure 5.2(b) and Figure 5.2(c) for corresponding field cuts). To determine the enhancement of the emission efficiency, we make several assumptions. First, we assume that radiative *e-h* recombination in the gold film is highly inefficient and remains highly inefficient in the presence of the nanoparticle. In this case any changes in emission rate are accompanied by an improvement of the emission efficiency by the same factor. Second, we assume that the radiative emission rate into a given narrow angular range is proportional to the simulated local electric field intensity under plane wave excitation at an angle in that range. Third, we assume that the collected PL spectrum is dominated by signal emitted at the highest collected angle. Since radiative recombination may lead to *s*- or *p*-polarized emission, we take into account simulated fields $E_{TM}(\omega_{em})$ and $E_{TE}(\omega_{em})$ for TM and TE polarization, where ω_{em} represents the angular frequency of the emitted light. Finally, we assume that carrier movement during the *e-h* recombination time is negligible relative to the spatial extent of the excitation field, allowing us the model excitation and emission enhancement based on simulated electric fields at a single position \vec{r} . Based on these

assumptions, the emission rate R_{PL} from a volume element near position \vec{r} excited at ω_{exc} is proportional to

$$R_{PL}(\omega_{exc}, \omega_{em}) \propto \varepsilon''_{IB}(\omega_{exc}) |\vec{E}(\omega_{exc})|^2 \times \gamma(\omega_{exc}, \omega_{em}) \left[\left| \frac{E_{TE}(\omega_{em})}{E_0(\omega_{em})} \right|^2 + \left| \frac{E_{TM}(\omega_{em})}{E_0(\omega_{em})} \right|^2 \right] \quad (5-2)$$

where γ is a function describing the bulk gold photoluminescence spectrum under excitation at ω_{exc} . Position arguments have been omitted for brevity. The total gold photoluminescence in the presence of a Au nanoparticle I_{NP} can now be calculated in relative units based on the simulated field distributions by integration of Eq. (5-2) throughout the particle volume and the Au film, while I_{film} can be determined similarly from simulated field distributions in the absence of a nanoparticle. The resulting spectra allow us to predict the PL enhancement factor g_{PL} using Eq. (5-1)) without the use of any free parameters for a given simulation geometry.

Figure 5.4(b) presents the resulting simulated PL enhancement spectrum g_{PL} for excitation at 532 nm (green solid line) and 633 nm (red solid line) of the structure shown in Figure 5.2. The peak-normalized calculated scattering spectrum is included for comparison (black dashed line). The simulated results show remarkable agreement with the experimentally determined enhancement spectra. First, the maximum simulated enhancement factor under excitation at 633 nm is 22000, only 22% lower than the experimentally determined value, despite the sensitivity of the result on the laser spot size and particle alignment in the laser spot. It bears repeating that this correspondence is obtained without the use of any free parameters. Second, the simulated PL enhancement under 532 nm excitation is a factor 8 lower than under 633 nm excitation, compared

to a factor 15 in the experiment. Third, the simulated enhancement spectra have nearly identical shape for different excitation wavelengths, as is also observed experimentally. Finally, the maximum simulated enhancement appears at slightly longer wavelengths than the scattering peak wavelength. Numerical simulations indicate that this small shift is a result of the difference in excitation angles for the scattering spectroscopy and PL measurements.

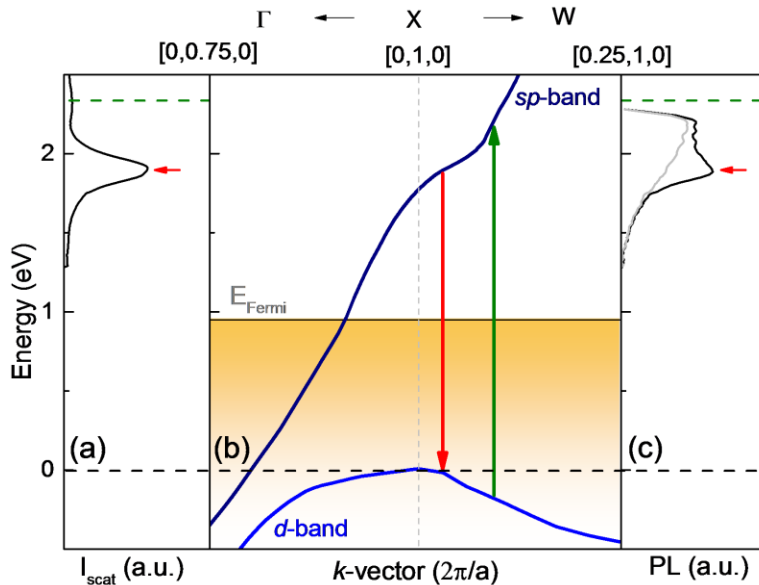


Figure 5-5: (a and c) Measured scattering and photoluminescence spectra of a film-coupled gold nanoparticle. The dashed green lines mark the photon energy corresponding to 532 nm excitation. The horizontal red arrows indicate the gap plasmon resonance energy. (b) The Au band structure around the X point near the Fermi level, adapted from Ref. [172]. The vertical green and red arrows show *e-h* excitation at 532 nm followed by plasmon enhanced recombination at an *e-h* energy separation that matches the gap plasmon resonance energy.

Given the good correspondence between the experimental and numerical results we are able to assign the physical origin of the various experimental observations. Figure 5.5 illustrates the contributing factors to the PL enhancement under excitation at 532 nm. Figure 5.5(b) shows the Au band structure around the X point adapted from Ref. [172] with the energy of the top of the *d*-band set to 0 eV, and energies below the Fermi level marked by the shaded region. Excitation of a gold film with 532 nm light can excite *d*-band electrons into empty *sp*-band states (green vertical arrow), followed by electron and hole relaxation and eventual electron-hole recombination. From the experimental scattering spectrum shown in Figure 5.5(a) it is clear that this green light (energy marked by the green dashed line) interacts with the higher order plasmon mode, resulting in slightly enhanced *e-h* generation in the Au nanoparticle gap region, in addition to the *e-h* pairs generated in the gold film. This excitation enhancement slightly increases the total PL intensity in this case, and does not affect the spectral shape of the emission. During relaxation of the generated energetic carriers, a small probability of radiative recombination exists. Since the extra *e-h* pairs are predominantly excited near the gap (see Figure 5.2(b)), they experience a strongly enhanced local optical density of states associated with the gap plasmon mode, leading to an enhancement of the emission rate. Consequently, the observation of large enhancement factors requires spatial overlap of the plasmon enhanced *e-h* generation profile with the field distribution of the plasmon mode that is responsible for the emission enhancement. When the energy difference between the electron and the hole during relaxation matches that of the gap resonance (marked by the red horizontal arrows in Figure 5.5(a) and Figure 5.5(c)) the recombination rate is maximally enhanced, coupling energy into the gap-mode which subsequently radiates into the far field. Figure 5.5(c) shows the corresponding experimental PL spectra under 532 nm excitation of a flat film

(gray line) and of a nanoparticle on the film (black line). For excitation at 633 nm, the mechanism is similar but the excitation photon energy is closer to the gap mode resonance energy, resulting in a stronger enhancement of the *e-h* generation rate. In addition, the excitation field distribution is almost exactly matched to that of the gap mode, maximizing the fraction of *e-h* pairs that can interact with the gap mode. Together these effects explain the larger overall PL enhancement factors observed under 633 nm excitation compared to those observed under 532 nm excitation.

While the numerical simulations and the physical model description are able to quantitatively describe the key aspects of the experimentally observed enhancement spectra, differences are observed. Most notably the simulated PL enhancement spectra exhibit a pronounced shoulder near 580 nm that is not observed in the experimental data. This shoulder is caused by the higher order resonance observed in the simulations, see Figure 5.2(b). As argued before, this mode is expected to be relatively highly damped due to nonlocal effects that are not accounted for in the simulations, resulting in an overestimation of the field enhancement and therefore of the *e-h* excitation enhancement. A final point worth noting is that the gap-mode enhanced photoluminescence does not originate exclusively from the Au nanoparticle. Based on the simulations, we find that the extra PL contributed by the gap-mode plasmon resonance ($\lambda = 660$ nm) originates largely from the region inside the Au nanoparticle closest to the substrate (~70 %) while the region of the gold film directly underneath the nanoparticle contributes ~30% of the added PL signal.

5.4. Summary

We have measured plasmonic gap-mode enhanced photoluminescence of a gold nanoparticle on an Al₂O₃ coated gold film. A PL enhancement factor was defined making use of the PL signal collected from a gold film reference, and based on this definition a maximum PL enhancement factor of 28000 under 633 nm excitation was obtained. Numerical simulations were shown to reproduce the excitation wavelength dependence, the spectral shape of the enhancement, as well as the absolute enhancement factors without the use of any free parameters. The enhancement could be explained entirely in terms of a plasmon enhanced *e-h* pair generation, combined with an increase in the emission rate associated with the electric field enhancement near the particle-substrate contact point.

6. NORMAL INCIDENCE EXCITATION OF SIDEWALL GAP-PLASMONS ON GOLD NANOPARTICLES IN A CYLINDRICAL NANOHOLE

6.1. Introduction

Gap-plasmon resonances of metallic nanostructures are rapidly gaining interest due to their extremely high electromagnetic field enhancement which is advantageous in several practical applications including molecular sensing [109, 128, 147, 173, 174], photovoltaics [175, 176], photocatalysis [86, 177], and nanolasers [178, 179]. Isolated metallic nanoparticles on a metallic film (also known as the ‘nanoparticle on a mirror’ geometry) represent an attractive gap plasmon supporting structure due to the fact that they can be prepared without the use of sophisticated lithography techniques. In these systems the nearby metallic surface breaks the spherical symmetry of the particle, turning the dipolar plasmon resonance mode of the isolated particle into a strongly confined *gap plasmon* mode localized near the point of contact with the substrate, providing field enhancement factors that significantly exceed those of Au NPs in free space. The gap plasmon resonance wavelength of Au NPs on a mirror can be tuned across the visible region by modifying the thickness of a spacer layer [42, 43, 46, 130, 139, 180], making this geometry a versatile sensing element. While gap plasmons on such supported NPs are desirable in several applications, the particle-on-mirror structure requires high-angle excitation and collection due to the net surface-normal polarization of the gap mode. This poses a challenge to the practical implementation of gap plasmons in sensor arrays.

A structure that could overcome this angular restriction is that of a plasmonic NP inside a nanohole (NH) in a metallic film. Here the metallic sidewall acts as the mirror surface that enables

the development of a gap plasmon. Early work on such a structure consisting of a Au NP in an aperture in a gold film by Wei *et al.* demonstrated large field enhancement and enhanced Raman scattering, but the study did not explicitly consider the polarization and excitation angle dependence of the structure's response or its spectral response under normal incidence excitation [181]. Moreover, the Au NPs in the study were chemically bound to the bottom of the nanohole, resulting in a variable NP-to-sidewall spacing and consequently an unpredictable resonance frequency determined by the exact location of the NP in the hole. A recent study by Jahr *et al.* investigated gold nanoparticles in nanoholes in a chromium film and used these structures to detect DNA hybridization events [182]. This study did not consider gap plasmons, instead using the aperture in the metal film to reduce background which enabled the detection of individual particle resonance wavelengths in a standard transmission geometry rather than using darkfield scattering. In the same year, Cecchini *et al.* investigated surface-enhanced Raman scattering (SERS) from functionalized Au nanoparticles flowing through a nanopore in a gold film [183]. Here the influence of particle-sidewall interaction on the field enhancement was considered, but due to the dynamic nature of the experiment it was not attempted to correlate particle position and spectral response. Nevertheless these prior studies show the promise of such structures as sensing elements with large field enhancement and the usefulness of the metal film as a means of reducing unwanted background signal.

In this chapter we present experiments and simulations of the spectral, angular, and polarization dependent response of a Au NP-in-a-hole system that makes use of an aluminum film to produce a hybrid Au-Al gap plasmon mode on the sidewall of the aperture. The presence of a

native oxide spacer layer on the Al sidewall leads to a natural minimum gap size, resulting in a predictable resonance wavelength. In addition, the oxide improves thermal and mechanical stability, and removes the need for organic spacer molecules that could introduce a background signal in biochemical sensing with the structure [148, 184]. The Au-Al hybrid geometry introduced here is shown to provide field enhancement factors comparable to those achieved in all-gold structures, and is demonstrated to enable facile normal-incidence excitation and detection. In addition, the structure can be fabricated using a simple and low-cost method, making it attractive for real-world sensor applications.

Figure 6.1(a) shows an illustration of the proposed structure which consists of a Au nanoparticle located inside a nanohole in an Al film on a glass substrate, covered by a liquid analyte. For brevity we will refer to this geometry as the *hole-in-one* (HiO) structure. The Au NP touches the Al sidewall enabling the development of a strongly confined gap plasmon mode between the Au NP and the metallic wall. A thin native oxide is present on all exposed Al surfaces. The thickness of Al film is purposely chosen to be slightly higher than the NP radius, placing the anticipated gap-plasmon mode close to the Al surface, which gives incoming analyte molecules (purple ellipsoids in Fig. 6.1(a)) relatively easy access to the hot-spot. Figure 6.1(b) shows the fabrication process of the HiO structures using a combination of nanosphere lithography (NSL) and NP deposition, as described in detail in Section 6.2. Briefly, 110 nm diameter polystyrene (PS) beads were drop coated onto a glass coverslip (step i), followed by Al deposition (step ii). Exposure to air of the resulting structure leads to the rapid formation of a few-nm thick native oxide on all exposed Al surfaces. Removal of the PS beads (step iii) leaves behind ~110 nm diameter holes in

the Al film. Subsequently, 60 nm diameter Au particles were drop coated onto the sample from colloidal solution (step iv). This process leaves many NP on the top surface, with a small fraction of the holes capturing a NP during the drying process. Figures 6.1(c) and 6.1(d) show Scanning Electron Microscopy (SEM) images of two HiO structures formed in this way.

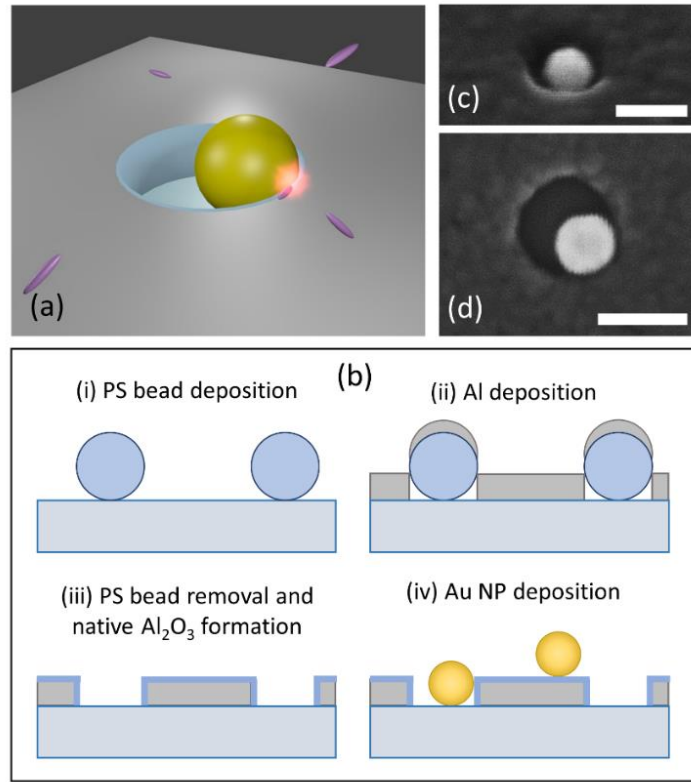


Figure 6-1: (a) Illustration of a HiO structure consisting of a Au NP inside a NH in an Al film on a glass substrate with the NP touching the oxidized Al sidewall. Analyte molecules (purple ellipsoids) can diffuse to the gap-plasmon resonance hot-spot (orange) close to the Al surface where they can be detected. (b) Fabrication process of the HiO structures using nanosphere lithography. (c and d) SEM images of two HiO structures, taken at a stage angle of 45° and at normal incidence respectively. The scale bar in the SEM images represents 100 nm.

6.2. Experiment and Simulation

6.2.1. Sample Preparation

Al nanohole templates were prepared by drop coating a methanol-diluted 110 nm diameter polystyrene bead colloidal solution (dilution factor of 10^6 from 1.4×10^{14} beads/mL initial concentration – Bangs Laboratories, Inc.) on oxygen-plasma treated glass coverslips. The plasma treatment was conducted using a Plasma-Therm 790 RIE/PECVD system at 40 mTorr pressure with 10 sccm He and 20 sccm O₂ gas flow rates for 30 seconds. After PS bead deposition, the glass coverslips were inspected using a darkfield optical microscope to verify that a uniform and sufficiently sparse distribution of PS beads was achieved to enable optical inspection of individual nanoholes (i.e. well below one PS bead per diffraction limited spot). Subsequently, an Al film with a thickness of 37 nm was deposited on the coverslips using a Temescal FC/BJD2000 electron beam evaporation system (deposition rate ~ 5 Å/s). This thickness provides substantial background signal attenuation in transmission measurements and places the NP-to-sidewall contact point for a 60 nm diameter Au NP just below the Al surface. After the deposition, a few-nm thick layer of native Al₂O₃ formed on the Al surface upon exposure to air. It was observed in optical transmission microscopy that sonication of the sample in acetone did not fully remove the Al-capped PS beads. To remove the remaining Al-covered PS beads tape-lift off was applied resulting in the formation of optical apertures with an areal density matching the previously observed PS bead coverage of the sample. The samples were subsequently sonicated in acetone and in isopropanol and rinsed with deionized water in order to remove any remaining polystyrene on the samples. Finally, 60 nm

diameter Au NPs were drop-coated on the samples from a methanol-diluted monodispersed Au NP colloidal solution (dilution factor of 100 from 2.6×10^{10} NPs/mL initial concentration, Nanopartz Inc.).

6.2.2. Microscopy and Spectroscopy

Optical microscopy and spectroscopy were performed on an Olympus IX-71 inverted microscope equipped with standard dark field optics using 20 \times and 50 \times darkfield objectives (Olympus UMPlanFl 20 \times BD, N.A. = 0.46 and UMPlanFl 50 \times BD, N.A. = 0.75). All optical measurements were taken in air, i.e. no analyte solution was present. For darkfield microscopy and spectroscopy the sample was top-illuminated (i.e. on the Al-coated side of the sample), whereas transmission microscopy and spectroscopy measurements were conducted using bottom illumination (i.e. illuminated from the substrate-side). Microscopy images and single particle spectra were recorded respectively using a Canon EOS 450D digital camera and an imaging spectrometer (Horiba iHR320) equipped with a thermoelectrically cooled CCD camera (Andor DU401-BR-DD). Spatial selection of individual HiO structures, Au NPs, and NHs for spectroscopy was done by limiting the spectrometer entrance slit width and using vertical binning of the recorded CCD data (collection area $\sim 3.5 \times 3.5 \mu\text{m}^2$). All spectra were corrected for the detector dark current. The scattering (or transmission) spectrum of each nanostructure (NS) was obtained by collecting the scattering (or transmitted) signal from the structure (I_{NS}), subtracting the signal from a nearby Al area (I_{ref}), and dividing by the latter, corresponding to the formula $I = (I_{NS} - I_{ref})/I_{ref}$. Scanning Electron Microscopy images were taken after detailed optical spectral

characterization of the sample using a ZEISS Ultra-55 field emission Scanning Electron Microscope.

6.2.3. Numerical Simulation and Calculation

Frequency domain full-field electromagnetic simulations of a HiO structure, a nanohole, and an Al film were carried out using frequency domain simulations in CST Microwave Studio [29]. Open boundary conditions were assumed for all simulations. The simulated HiO structure consists of a 60 nm diameter Au NP in a 110 nm diameter nanohole in a 37 nm thick Al film on a glass substrate with the Au NP touching the sidewall. A 3.4 nm thick native Al_2O_3 layer is assumed to be present on the sidewalls of the NH based on previous measurements of the Al_2O_3 film on similarly deposited Al films [130]. Literature data were used for the dielectric functions of Au, Al, and Al_2O_3 [4, 114, 115]. A plane wave with the electric field polarized parallel to the in-plane symmetry axis of the simulated HiO structure was used as the excitation source. The structures were illuminated from the substrate side as in the experiments. The simulated transmission spectra of the HiO structure and the nanohole were obtained by integrating the total transmitted power of the structure at each frequency, subtracting the transmitted power P_{Al} of a continuous Al film at the same excitation frequency, and dividing by P_{Al} , which matches the background subtraction method used to obtain the experimental spectra.

6.3. Results and Discussion

In order to locate nanoholes containing a NP, selected sample regions were imaged using darkfield microscopy before and after drop coating of the colloidal Au NP solution, and spots displaying a modified scattering color after NP deposition were identified. Figure 6.2(a) shows a darkfield microscopy image of a typical sample region after removal of the PS beads but before Au NP deposition, taken with a 20 \times objective. The green scattering spots originate from the nanoholes in the Al film formed in the NSL step. A typical SEM image of one of the many NHs on the sample is shown in Fig. 6.2(c) revealing a largely circular hole with a diameter of 104 nm, close to the size of the PS beads used in the nanosphere lithography step.

Figure 6.2(b) presents a darkfield microscopy image of the same area as shown in Fig. 6.2(a) taken after Au NP deposition. Several subtle changes can be seen. First, an additional pale-yellow scattering spot has appeared as marked by the red arrow. This type of feature was found to originate from isolated Au NPs on the Al surface, as determined by correlating optical microscopy images with SEM images. An example SEM image of one such particle is shown in Fig. 6.2(d). More importantly, while the scattering color of most NHs is unchanged after NP deposition, the hole indicated by the magenta arrow shows a reduced brightness and a more pale yellow or orange color, possibly indicating the presence of a Au NP in the nanohole. Visual inspection of the polarization dependence of the scattered light showed that the modified structures exhibit a loss of rotational symmetry, as expected in the presence of an off-center NP in the nanohole. Similar changes in optical signature were observed at different locations on the sample, and several such locations were selected for further characterization. Figure 6.2(e) shows an SEM image of one of

these structures, revealing a HiO structure containing a 62 nm diameter gold nanoparticle in close contact with the sidewall of a 104 nm diameter circular hole in the Al film. Figure 6.2(f) shows another example of a HiO structure on the same sample. Most of the HiO structures were found to contain an off-center Au NP, however in one candidate structure that showed a different spectral response and relatively weak polarization dependence the NP was found to have dried near the center of the NH. Nevertheless, the side-wall attached geometry appears to be most favorable, possibly due to capillary forces acting on the particle during the drying process after drop-coating [185, 186]. Additional darkfield microscopy and SEM images are provided in Appendix D.

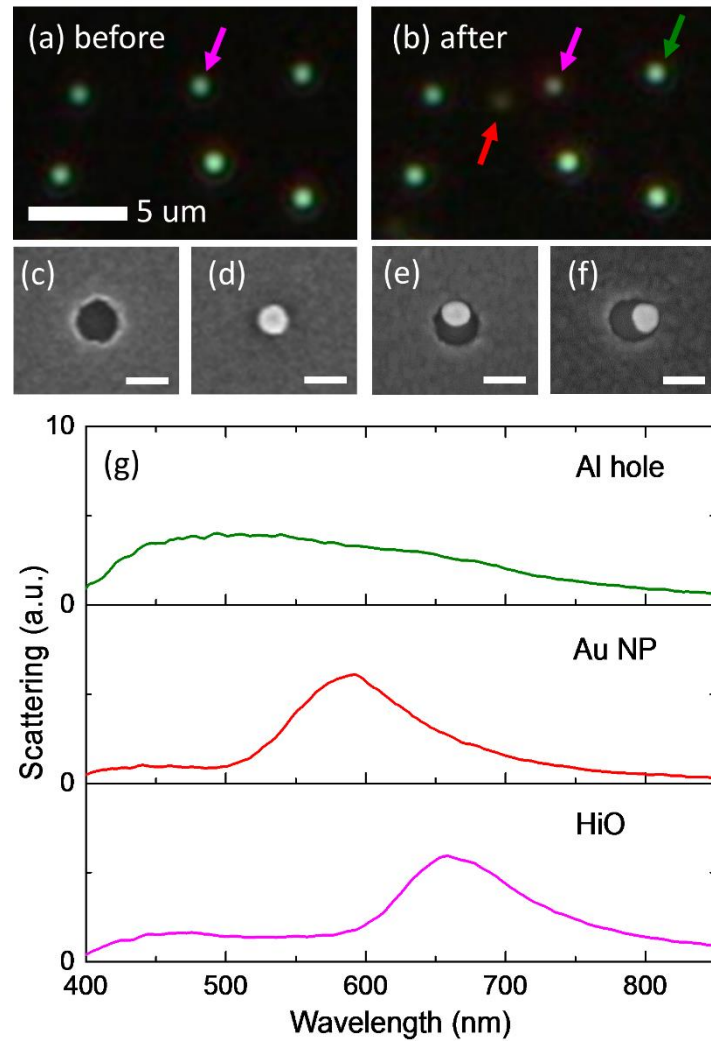


Figure 6-2: (a) Darkfield microscopy images of a representative sample region after nanosphere lithography (a) before and (b) after Au NP deposition. (c–f) SEM images of a nanohole, a Au nanoparticle, and two HiO structures, respectively. The scale bar represents 100 nm. (g) Scattering spectra of the NH, Au NP on Al, and HiO structure marked by the arrows in (b).

Figure 6.2(g) presents darkfield scattering spectra obtained from the structures indicated by the arrows in Fig. 6.2(b). The nanohole shows a broad featureless scattering spectrum, with a maximum in the blue-green spectral region. In contrast, the scattering spectrum of the isolated Au NP shows a prominent resonance peak \sim 585 nm with a full width at half maximum (FWHM) of \sim 105 nm, corresponding to a gap plasmon resonance between the Au NP and the oxidized Al film as observed in our previously published results [130]. The HiO spectrum, measured on the actual structure shown in Fig. 6.1(d), shows a clear scattering peak at \sim 660 nm with a similar scattering intensity and linewidth as the isolated Au NP. The similarity of this scattering spectrum to that obtained from isolated NPs suggests that the HiO structure indeed supports a gap-plasmon mode, with a modified spectral response due to the curvature and finite height of the Al sidewall. Additional representative scattering spectra are provided in Appendix D.

Figure 6.3(a) shows a darkfield microscopy image of the HiO, Au NP, and Al nanohole labelled by the arrows in Fig. 6.2(b), taken with a 50 \times objective. The image was rotated clockwise by 90° for presentation purposes. At this higher magnification the isolated Au NP shows the characteristic red ring-shaped scattering pattern associated with surface-normal gap plasmon resonances of single Au NPs on metallic substrates [46, 109, 130]. Figure 6.3(b) shows the same structures with a linear analyzer inserted in the collection path of the microscope at six different analyzer angles. The analyzer transforms the ring-shaped scattering pattern of the isolated Au NP into a dumbbell-shaped image, as expected based on the known radial polarization of the scattered light collected from the gap plasmon resonance. The Au NP thus acts as a convenient indicator of the analyzer angle in Fig. 6.3(b). The fact that the NH and HiO structures remain circularly

symmetric upon rotation of the analyzer proves that the modes causing these scattering features are not dominated by a surface-normal polarization, a first indication that the HiO structure is better suited for normal incidence excitation and collection than the isolated Au NP. As the analyzer is rotated the scattering color of the nanohole remains unchanged while the HiO structure exhibits a clear color shift varying between red and green. Figure 6.3(c) presents an SEM image of the sample area shown in Fig. 6.3(a) and 6.3(b), displayed on the same scale.

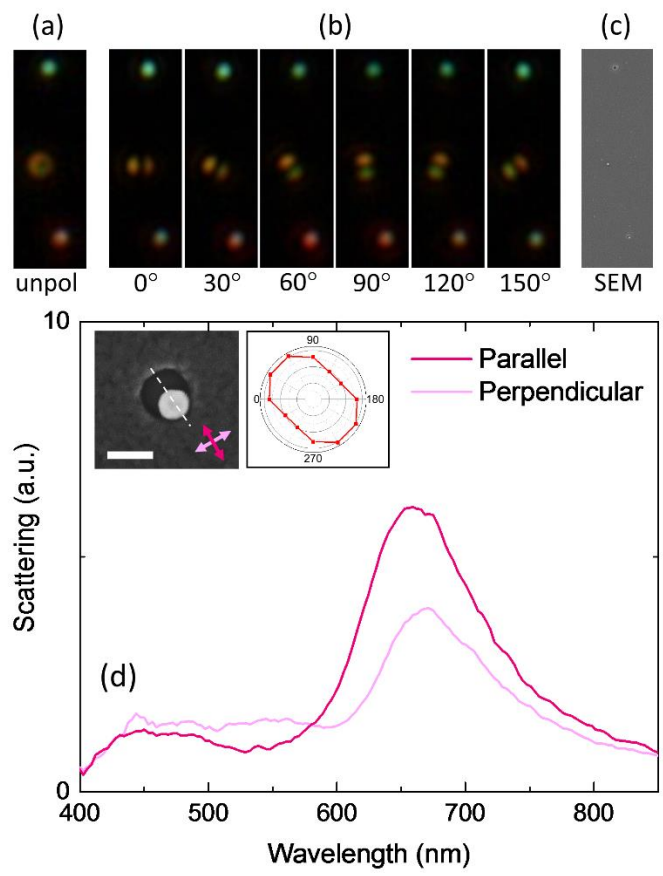


Figure 6-3: (a) Darkfield microscopy image of the NH (top), Au NP (middle), and HiO structure (bottom) from Fig. 2(b). (b) Darkfield microscopy image of the same structures but with a linear analyzer inserted in the collection path of the microscope. (c) Matching SEM image of the structures. The images in (a–c) are $\sim 2.5 \mu\text{m}$ wide. (d) Scattering spectra of the HiO structure collected at two analyzer angles, approximately parallel and perpendicular to the symmetry axis (dashed white line) indicated respectively by the dark and light magenta double arrows in the SEM image of the HiO structure in the inset. The scale bar in the inset is 100 nm. The polar plot shows the peak scattering intensity of the HiO structure as a function of analyzer angle.

To quantify the color changes observed in Fig. 6.3(b), scattering spectra of the HiO structure in Fig. 6.3(a) were collected at different analyzer angles. The polar plot in Fig. 6.3(d) shows the recorded peak scattering intensity as a function of analyzer angle, revealing maximum scattering at an angle of $\sim 60^\circ$. The SEM image of this particular HiO structure in Fig. 6.3(d) shows that the Au NP touches the oxidized Al sidewall of the nanohole at this same angle, corresponding to the symmetry axis of the structure (dashed white line). The two spectra shown in Fig. 6.3(d) were recorded with the analyzer oriented along the light and dark magenta arrows in the SEM image. Note that the HiO structure indeed appears red in Fig. 6.3(b) when the analyzer is aligned with the symmetry axis.

To investigate the optical response of the HiO structures under normal incidence excitation, transmission measurements were carried out. Figure 6.4(a) presents the obtained transmission spectra of the HiO structure and the nanohole marked by the magenta and green arrows in Fig. 6.2(b). The inset shows the corresponding transmission microscopy image at $50\times$ magnification. To obtain transmission spectra of the individual nanostructures in the partly transparent Al thin film, a background subtraction procedure was carried out as described in Section 6.2. The resulting transmission spectrum of the nanohole is broad and virtually featureless, similar to the NH scattering spectrum in Fig. 6.2(g). The transmission spectrum of the HiO on the other hand shows a region of enhanced transmission at ~ 670 nm with a FWHM linewidth of ~ 140 nm. This spectral location and linewidth matches the scattering peak of the HiO structure in Fig. 6.2(g) suggesting that the sidewall gap plasmon mode is successfully excited under normal incidence illumination.

To further clarify the nature of the observed optical resonance enhanced transmission in Fig. 6.4(a), numerical simulations were carried out as described in Section 6.2. Figure 4(b) shows the simulated transmission spectra of a HiO structure and of an isolated nanohole in an Al film, both on a glass substrate. The simulated transmission spectrum of the HiO structure exhibits a peak resonance wavelength of \sim 645 nm and a FWHM linewidth of \sim 120 nm while the simulated nanohole transmission spectrum is broad and featureless, both in good agreement with the measured results. Differences between measured and simulated resonance wavelength and linewidth may be due to structural imperfections, e.g. a small variation in the Au NP and hole size, Al and Al_2O_3 thickness, and surface irregularities, and variations in dielectric function compared to the literature values used in the simulations.

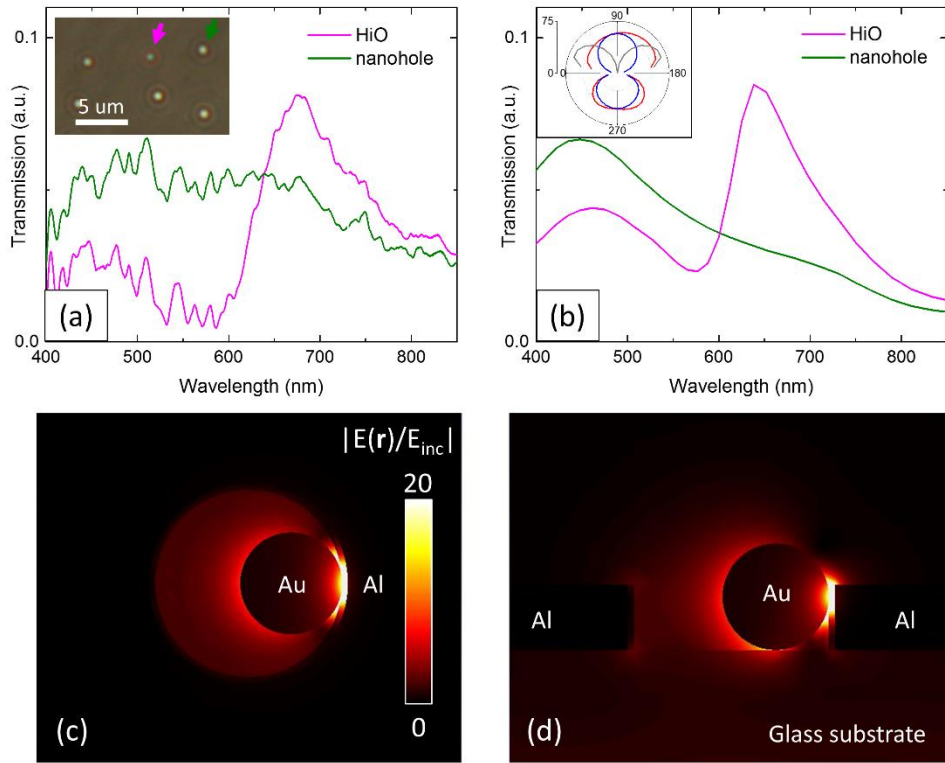


Figure 6-4: (a and b) Measured and simulated transmission spectra of a HiO structure and an isolated NH. The measured spectra were obtained from the HiO structure and NH in Al marked by the magenta and green arrows in the transmission microscopy image inset. (c and d) Simulated distribution of the electric field enhancement factor of a HiO structure under normal incidence plane wave excitation at the main resonance frequency. The field cuts correspond to (c) a plane along the surface at the height where the Au NP touches the oxidized Al sidewall and (d) a plane normal to the surface along the symmetry axis of the HiO structure. The polar plot in (b) shows the electric field enhancement factor in the NP-oxide junction region of the HiO structure as a function of excitation angle along (red curve) and normal to (blue curve) the HiO symmetry axis, and of a Au NP on an Al film (gray curve).

The good correspondence between the measured and simulated transmission spectra indicates that the simulated field distributions match the real-world field distributions well. Figures 6.4(c) and 6.4(d) show the magnitude of the simulated electric field enhancement factor $|E(\mathbf{r})/E_{\text{inc}}|$ at the main resonance frequency, where $E(\mathbf{r})$ is the simulated electric field distribution, and E_{inc} represents the amplitude of the incident electromagnetic wave. The top view of the HiO structure in Fig. 6.4(c) represents a field cut at the height where the NP touches the sidewall, and the side view in Fig. 6.4(d) shows a field cut normal to the sample surface along the symmetry axis of the HiO structure. The enhanced electric field is seen to be extremely confined near the junction between the Au NP and the oxidized sidewall of Al film, and a peak electric field enhancement factor as high as 52 is observed. The field distribution on resonance closely resembles a gap-plasmon mode as observed for Au NP on flat Al films, but in this case the mode is supported by the NP and the curved Al sidewall, with a predominant field polarization normal to the sidewall, i.e. parallel to the sample surface. Figure 6.4(d) shows that at the chosen Al film thickness the strong field enhancement occurs close to the sample surface. Additional simulations were carried out to investigate the excitation-angle dependence of the gap-plasmon related field enhancement of a HiO structure and of a Au NP on a flat Al film with a native oxide layer. The polar plot in Fig. 6.4(b) shows the electric field enhancement factor at the junction of the HiO structure under excitation at 625 nm with the incident electric field polarized in the surface-normal plane along the HiO symmetry axis, as a function of the angle of incidence, with 90° corresponding to normal incidence top illumination. The HiO structure is seen to produce a large field enhancement factor over a wide range of excitation angles in the surface-normal plane along (red curve) and normal to (blue curve) the HiO symmetry axis in both top and bottom illumination configuration.

comparison, the gray curve shows the corresponding excitation-angle dependence of the field enhancement factor at the gap plasmon resonance frequency of the Au NP on the flat Al film under TM-polarized excitation. The HiO structure produces significantly larger field enhancement factors for near-normal excitation angles and offers a more angle-invariant response compared to that of the Au NP on the continuous Al film. Note that the gap-plasmon mode of the HiO structure can be excited through the glass substrate, implying that optical interrogation can be carried out even in the presence of a strongly absorbing analyte solution. The omnidirectional excitation of strong gap-plasmon enhanced local electric fields makes the presented HiO geometry ideal for real world applications that rely on normal incidence optical inspection of large area arrayed sensor elements.

The observations made above highlight several attractive features of the particle-in-a-cylindrical hole geometry. A large field enhancement can be obtained under normal incidence excitation, enabling easy optical access to the structure. The structure enables a confined and enhanced optical field close to the sample surface, potentially allowing relatively easy access of analyte molecules to the hot-spot. The presence of a native Al_2O_3 layer introduces a natural minimum spacing between the Au and Al surfaces, which reduces relative variation in gap size related to structural imperfections of the sidewall and the NP, enabling a reproducible resonance wavelength. Furthermore, the oxide layer avoids the development of charge transfer plasmons with reduced field enhancement. The materials used are known to be chemically and mechanically resilient, making the structure broadly applicable. The structure does not rely on organic spacer layers, avoiding the introduction of background signals in SERS/fluorescence-based sensing of

organic molecules. After selective area substrate removal the nanohole could also function as a flow channel, further improving analyte access to the gap plasmon. The nanohole in the Al film also offers several advantages of zero-mode-waveguides including a reduction of the excitation of fluorescence in the analyte, a reduction of the transmission of any excited fluorescence back to the illumination side, and a small sampling volume which could allow the use of undiluted analyte solutions [187-192]. Finally, the resonance wavelength can easily be controlled by several structural parameters, including particle size, hole diameter, and oxide thickness. The combination of these advantages and the relative ease of fabrication of these structures make the hole-in-one structure a promising building block for high sensitivity biochemical sensor arrays.

6.4. Summary

In conclusion, we have presented an experimental study of hybrid hole-in-one nanostructures consisting of a gold nanoparticle in a nanopore in an aluminum film. The structure supports a strong gap-plasmon resonance and can be fabricated using simple and low-cost methods while offering a significant improvement in the optical accessibility to the hot-spot compared to metallic nanoparticles on a continuous Al film. The structure shows a prominent plasmon resonance peak at ~670 nm in both scattering and normal incidence transmission spectra indicating that gap-plasmons supported by the HiO structures can be excited and detected at near-normal angles of incidence. Numerical simulations of the structure match the experimental results and suggest a maximum electric field enhancement factor at the hot-spot of ~52 with a resonance hot-spot near the top surface of the structure. The structure generates strong field enhancement over a

broad range of excitation angles. The presented self-assembled structure possesses several desirable optical traits which make it ideal for implementation as a sensing element in large-area ultrasensitive biochemical sensor arrays.

7. SUMMARY AND OUTLOOK

In summary, this Thesis presents an extensive study on the topic of gap-plasmon resonances of single gold nanoparticles. It was shown that the optical resonance response and electromagnetic field enhancement factors of gold nanoparticles can be controlled in a simple manner by coupling metallic nanoparticles with metallic substrates.

In Chapter 2 and Chapter 3, it was shown that gap-plasmon resonances of gold nanoparticles can be precisely tuned over the range of ~140 nm from green to infrared by controlling the thickness of an Al₂O₃ spacer layer between gold nanoparticles and metallic substrates. The process produced reliable plasmonic structures with few-nanometer precision control of the resonance wavelength without involving costly and complicated fabrication techniques. The Al₂O₃ spacer layer was shown to serve as a protecting layer providing extra stability of the structure under laser illumination. In addition, the structure does not use organic spacer layers, and consequently will not introduce background signal related to organic molecules when used as a biochemical sensor. The precise resonance control, robustness, and background free operation make the structure attractive for real world sensing applications.

In Chapter 4, we presented the effect of nanoscale surface roughness of a metallic substrate which causes spectral variation in the optical resonance spectra of gold nanoparticles. This effect is important to consider when dealing with plasmonic structures that involve coupling between metallic particles and surfaces at extremely small particle-substrate separation distances.

Subsequently in Chapter 5, the strong field enhancement of gap-plasmon resonance of gold nanoparticles on a gold film was demonstrated through enhanced photoluminescence of gold

nanoparticles. A model for the photoluminescence enhancement was developed, which produced exceptional agreement between experiment and simulation without the use of any free parameters. A photoluminescence enhancement factor higher than four orders of magnitude was reached under 633 nm laser excitation, implying a combined local enhancement of the excitation and emission rate of 1 million near the junction between a particle and the film.

Finally in Chapter 6, an alternative gap-plasmon supporting nanostructure was introduced. The so-called *hole-in-one* nanostructure combines a zero-mode-waveguide in an aluminum film with a gold nanoparticle forming an easily optically accessible gap-plasmon with stable spectral performance while supporting large field enhancement factors.

The work presented in this Thesis demonstrated how the gap plasmon resonance of supported metal nanoparticles can be precisely controlled by nanoscale modification of the local environment of the particles, and how the localized electric field enhancement helps to increase the efficiency of different optical processes. Such control over the extremely confined and strongly enhanced electric field makes it possible for gap plasmons to be integrated with and to improve the performance of a broad range of optical devices. The simple fabrication process also makes it feasible for the presented structures to be made in large scale. Examples of applications that can directly benefit from gap plasmon enhanced electric fields are optical biosensing, photon upconversion, and photocatalysis. Gap plasmons are also ideally suited for the investigation of the transition between classical and quantum plasmonics, providing gap sizes small enough to allow for carrier tunneling and exhibiting mode sizes that are small enough to require the consideration of nonlocal and quantum size effects. Additionally due to their ability to concentrate light and amplify optical signals from nanometer-sized objects, gap plasmons can be employed as a means

to study light matter interaction at the molecular level. This could lead to better understanding and optimization of processes such as photoexcitation and photoemission of single molecules or single quantum dots. Understanding and controlling these effects is indeed an important step in the realization of nanoscale integrated optical devices.

APPENDIX A: SUPPORTING INFORMATION FOR CHAPTER 2

A.1. Spectral Measurements

Single particle scattering spectra $I_{SC}(\lambda)$ were obtained using the relation

$$I_{sc}(\lambda) = \frac{I_{NP}(\lambda) - I_{REF}(\lambda)}{I_{IN}(\lambda)} \quad (\text{A-1})$$

with $I_{NP}(\lambda)$ the signal obtained from an area containing a single nanoparticle, $I_{REF}(\lambda)$ the signal collected from a region without a nanoparticle, and $I_{IN}(\lambda)$ the dark-current corrected reference spectrum, peak-normalized to compensate for any variation in lamp brightness between experiments. Figure A.1 shows I_{NP} , I_{REF} , I_{IN} , and the resulting I_{SC} corresponding to the blue curve in Fig. 2.2(a) of the main manuscript before anodization. Note that the thus obtained scattering spectrum contains a small offset at long wavelengths well away from the particle resonance. This offset may be due to slight variations in lamp output power between the nanoparticle and reference measurement, or a slight variation in substrate scattering at the particle location and at the nearby location used for the reference measurement. The magnitude of this offset was typically less than $\pm 4\%$ of the peak nanoparticle scattering signal. To correct for this contribution the scattering signal at $\lambda=800$ nm was subtracted for all measurements. In the main manuscript the final curves are shown at a spectral resolution of 10 nm.

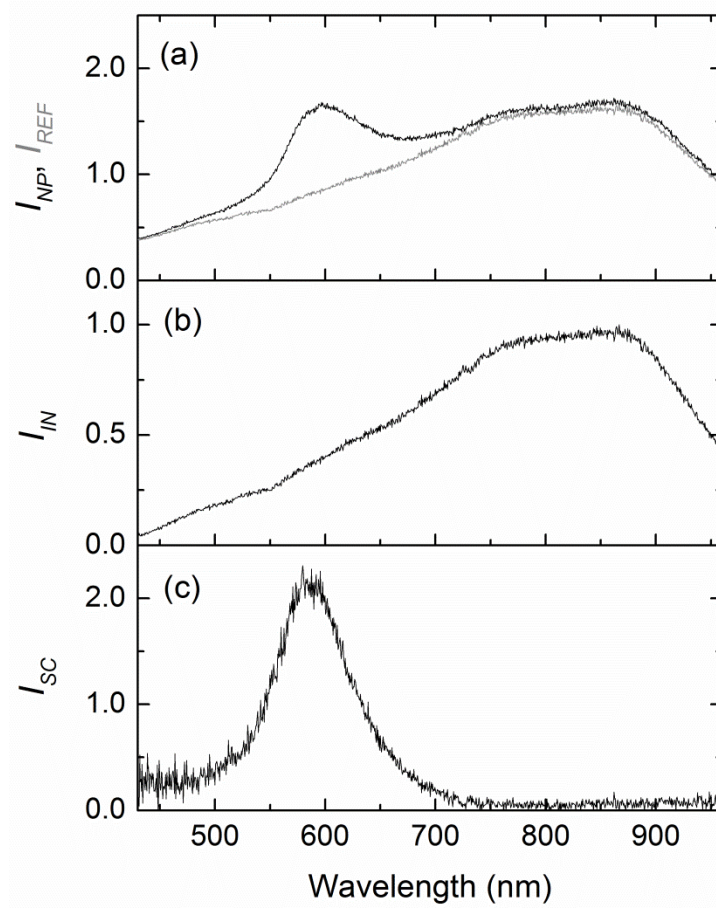


Figure A-1: Darkfield scattering spectra including (a) the raw signal obtained from an area containing a single nanoparticle (I_{NP}) and the raw signal collected from a nearby region without a nanoparticle (I_{REF}), (b) the peak-normalized, dark-current corrected reference spectrum (I_N), and (c) the resulting single particle scattering spectrum before background correction (I_{SC}).

A.2. Particle Size Variation

In order to evaluate the possible influence of known particle size variations on the measurements, scattering spectra were simulated as described in the main manuscript for five

particle diameters in the range $50 - 70$ nm for oxide spacer thickness values $d = 4$ nm and $d = 16$ nm. The results are shown in Fig. A.2. For both aluminum oxide thickness values the scattering spectra undergo a small red-shift as the particle size increases. In addition, the peak scattering strength increases rapidly with increasing particle diameter.

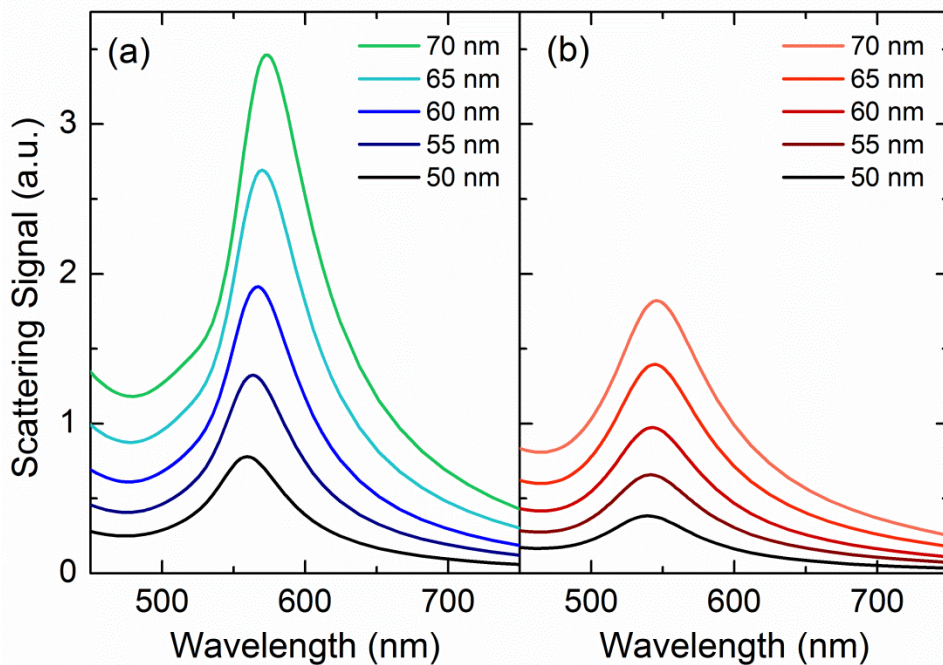


Figure A-2: Calculated scattering spectra of the gold nanoparticles with different diameters on an aluminum film with (a) 4 nm and (b) 16 nm aluminum oxide surface layer.

Figure A.3 presents the corresponding peak scattering wavelength as a function of particle diameter for both oxide thicknesses. The solid lines represent linear fits to the data. Note that the peak wavelength shifts more rapidly for the thin oxide layer. The dashed lines represent particle sizes corresponding to one standard deviation above or below the mean nanoparticle size based on the size histogram provided by the vendor. These results were used to determine an anticipated

spectral variation in the measurements based on the vendor-specified particle size variation, shown as effective error bar on the simulated curves in Fig. 2.3.

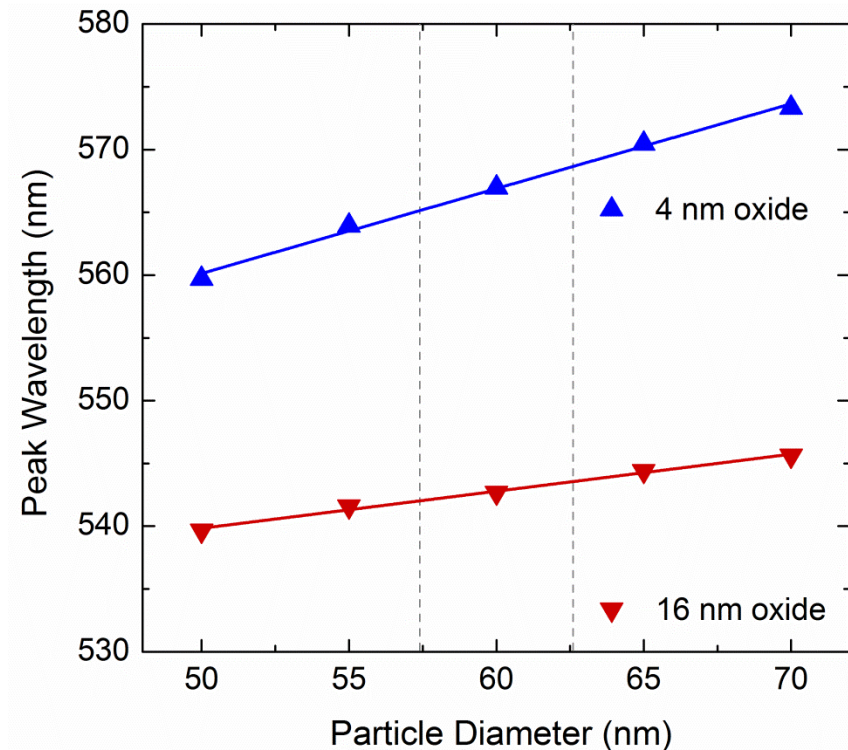


Figure A-3: Peak scattering wavelength vs. nanoparticle diameter for samples with a 4 nm and 16 nm aluminum oxide layer thickness.

The dashed lines represent the anticipated experimental particle size variation.

APPENDIX B: SUPPORTING INFORMATION FOR CHAPTER 3

B.1. Conversion of Hyperspectral Images to False-color RGB Representation

Images of 60 nm diameter gold nanoparticles on Al₂O₃ coated gold film were taken using a Gooch & Housego HSi-440C Hyperspectral camera. A stack of 100 images was taken in the range of 500 nm-800 nm with a collection bandwidth of 10 nm per image, and a spectral sampling of 3 nm. The images were converted to a RGB color representation by multiplying the spectral images with artificial color response functions for the red, green, and blue channel and combining them into a single false color RGB image. Figure B.1(a) shows the response functions used peaking at 620 nm (blue channel), 640 nm (green channel), and 680 nm (red channel), chosen to give good visibility of the experimentally observed resonance wavelength shifts. Figure B.1(b-d) presents examples of the image data obtained for two nanoparticles on a gold film, showing the resulting the blue channel (Fig. B.1(b), shown at 15×brightness), the green channel (Fig. B.1(c), shown at 2×brightness), and the red channel (Fig. B.1(d)). Figure B.1(e) shows the final false color image produced after combining the three color channels into a single RBG image. The color bar represents the expected image color as a function of detected (scattered) wavelength, assuming a linewidth of 40nm for the scatterers.

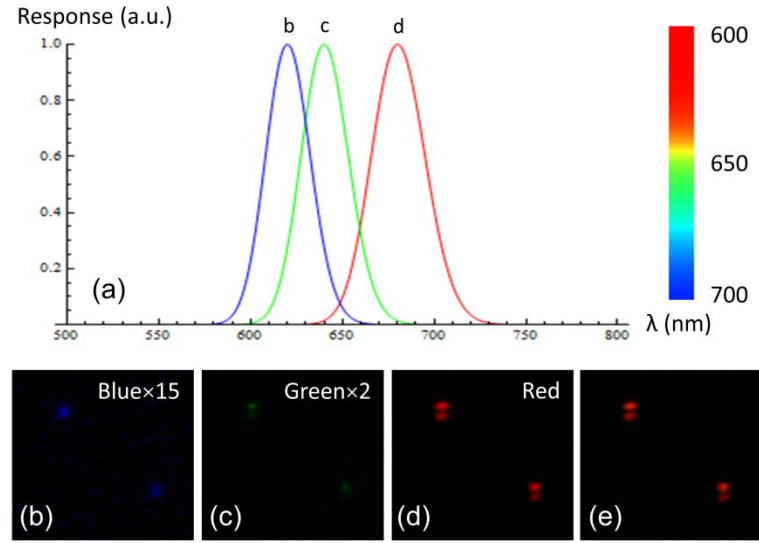


Figure B-1: (a) The color response functions used to generate false-color scattering images with the corresponding color scale. (b-d) image information corresponding to the blue, green, and red color channels with adjusted brightness, respectively. (e) The final false color image based on the three color channels shown in (b-d).

B.2. Simulation of Single-particle Scattering Spectra and Electric Field Distributions

Simulations were performed based on the frequency domain Finite Integration Technique using CST Microwave Studio [29]. The simulated structure consists of a gold nanoparticle, with or without an organic shell ($n=1.5$) on an Al_2O_3 coated gold film on a semi-infinite glass substrate ($n=1.5$) using open boundaries at the top and bottom of the simulation volume, and unit cell boundary conditions along the film (x and y directions) with a 200 nm unit cell length. The structure is excited with plane-wave TE and TM illumination at a 77° angle of incidence with respect to the surface normal, as shown in Fig. B.2.

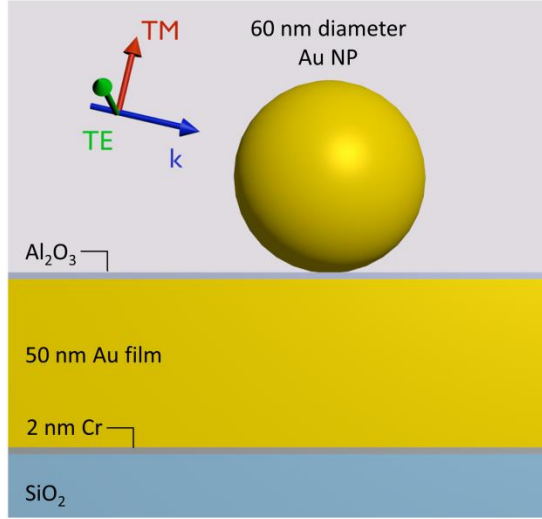


Figure B-2: Simulation structure used to calculate single particle scattering spectra.

The simulated scattering spectra are assumed to be dominated by dipolar contributions. To calculate the scattering spectrum as a function of angular frequency ω , the total dipole moment $\vec{\mu}_{tot}(\omega)$ of the particle and its immediate environment is determined as follows:

$$\vec{\mu}_{tot}(\omega) = \epsilon_0 \int_V \chi(\omega, \vec{r}) E(\vec{r}) d\vec{r} \quad (\text{B-1})$$

The integration volume was chosen to contain all near field components by integrating over the gold nanoparticle, the organic shell (if present), the Al_2O_3 layer, and the 50 nm gold film immediately underneath the nanoparticle. A reference calculation was carried out under the same conditions, but in the absence of the particle, and the dipole moment integration was repeated resulting in a reference dipole moment $\vec{\mu}_{ref}(\omega)$. The nanoparticle-related dipole moment $\vec{\mu}_{NP}(\omega)$ then follows from $\vec{\mu}_{NP}(\omega) = \vec{\mu}_{tot}(\omega) - \vec{\mu}_{ref}(\omega)$, and the resulting nanoparticle related scattering spectrum $I_{scat}(\omega)$ is assumed to follow the radiation power of a point dipole given by

$$I_{scat}(\omega) \propto \omega^4 |\vec{\mu}_{NP}(\omega)|^2 . \quad (B-2)$$

Figure B.3 shows the calculated scattering spectrum of a 60 nm diameter Au nanoparticle coated with a 0.75 nm thick organic layer on a gold film, showing the x-, y-, and z-polarized contributions separately. The z-polarized dipole radiation is the major contribution to the scattering signal. The total signal observed at ~550 nm can be seen consist of contributions from lateral (x- and y-polarized) dipole moments, as well as a normally polarized dipole moment associated with modes on the particle with a partly multipolar character.

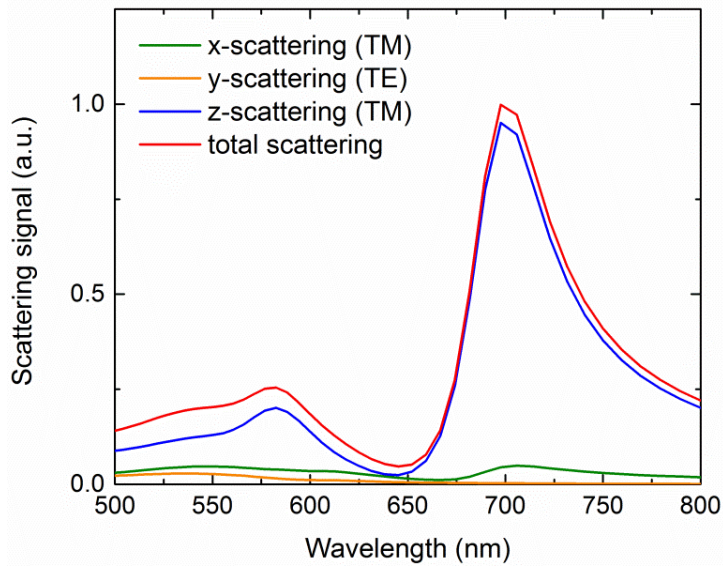


Figure B-3: Calculated scattering spectrum of a 60 nm diameter Au nanoparticle coated with a 0.75 nm thick organic layer on a gold film (red line) as well as the separate contributions from x-, y- and z- oriented dipole moments (green, orange, and blue curves, respectively).

B.3. Laser Spot Size Determination using Nanoparticle-mediated Beam Sampling

In order to obtain a precise measure of the irradiance used to investigate the particle stability against laser irradiation, the beam profile of the He-Ne laser beam ($\lambda=633$ nm) directly at the sample surface was measured using a gold nanoparticle as an optical probe. A 60 nm diameter gold nanoparticle on a 3.4 nm Al_2O_3 coated gold film was scanned through the laser spot using a Physik Instrumente NanoCube piezo stage while monitoring the Rayleigh scattering from the particle. Since the particle is much smaller than the laser spot size, this measurement can provide a precise measurement of the spot size, without errors related to the diffraction limit.

Figure B-4 shows the collected scattering signal versus particle position relative to the center of the laser spot (red squares). The solid blue line represents a Gaussian fit with a full width at half maximum (FWHM) of 2.2 μm . Repeating the measurement along a different scanning direction revealed that the spot was approximately circular. Based on the known illumination power and the illumination spot size and shape, the irradiance at the center of the beam was determined.

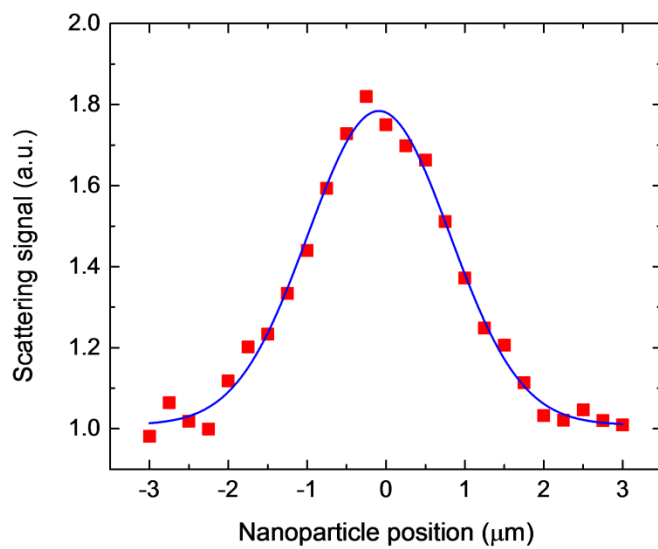


Figure B-4: Rayleigh scattering signal versus nanoparticle position relative to the center of the laser spot (red squares). The blue curve represents a Gaussian fit to the measurement, showing a FWHM of 2.2 μm .

APPENDIX C: SUPPORTING INFORMATION FOR CHAPTER 5

C.1. Scattering Spectrum from Different Gold Nanoparticles

Dark-field scattering spectra were collected for several particles on the Al₂O₃ coated Au film. To demonstrate the consistency of the plasmon resonant response of these supported particles, Figure C-1 shows the scattering spectra of three randomly selected particles. In this and all following graphs the left panel shows the particle (NP1) used in the main manuscript. Note that the particles show maximum scattering at a wavelength of 658 ± 11 nm. Small spectral differences are present, possibly related to small variations in the local environment at the particle-substrate junction.

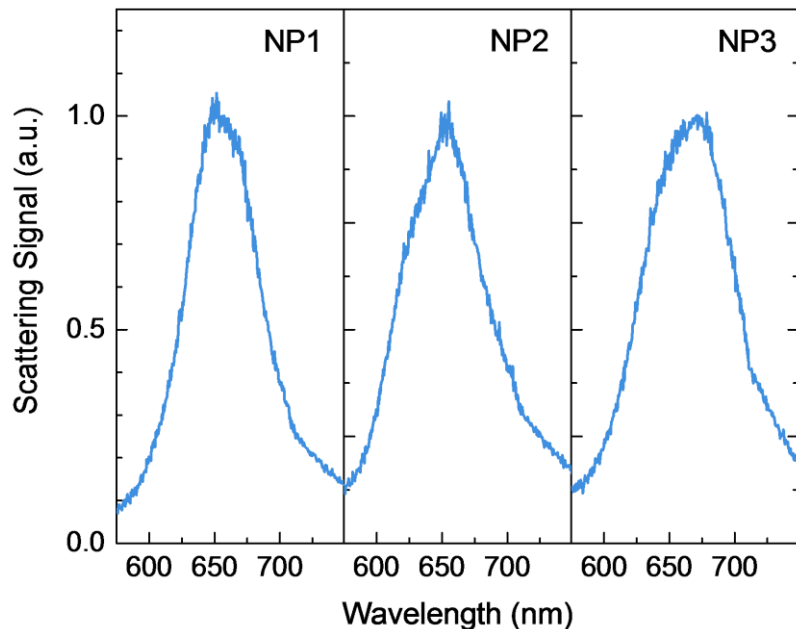


Figure C-1: Measured single nanoparticle scattering spectra of three different gold nanoparticles on an Al₂O₃ coated Au film on glass.

C.2. Spectral Shape of the Particle-related Photoluminescence

The photoluminescence (PL) spectra from Au nanoparticles on an Al₂O₃ coated gold film as shown in Fig. 5.3 appear to have a different spectral shape depending on the excitation wavelength. This apparent difference is largely an artifact due to the different relative contribution of the PL background originating from the gold film. To highlight this fact, Figure C.2 shows the collected spectra, corrected for the film PL background. These spectra thus correspond to the term ($I_{NP} - I_{film}$) in Eq. (5-2) and represent the added PL signal due to the presence of the particle in the excitation spot. Note that at energies more than ~80 meV below the excitation energy the added PL signal has a similar spectral shape for all measurements.

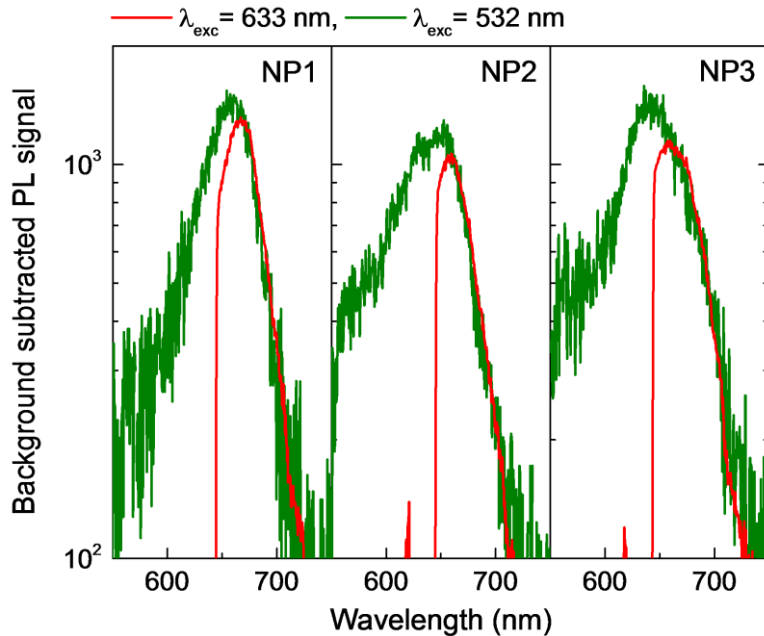


Figure C-2: Background subtracted photoluminescence from three gold nanoparticles showing a small offset between the peak positions of the 532 nm and 633 nm excited NP-mediated photoluminescence spectra. The spectra under 532 nm excitation were scaled to facilitate comparison with the 633 nm excited spectra.

C.3. Photoluminescence Enhancement Spectrum from Different Gold Nanoparticles

The analysis presented in the main manuscript was repeated for additional nanoparticles in order to test the reproducibility of the results. Figure C.3 shows the obtained PL enhancement factors for the two excitation wavelengths used with a scaled scattering spectrum of the corresponding particle overlaid on each curve. Note that the peak position of the enhancement consistently appears identical for both excitation wavelengths, that the magnitude of the enhancement is consistent within 7% and 20% for 633 nm and 532 nm excitation, respectively,

and that the location and spectral shape of the scattering peak closely matches the enhancement peak shape.

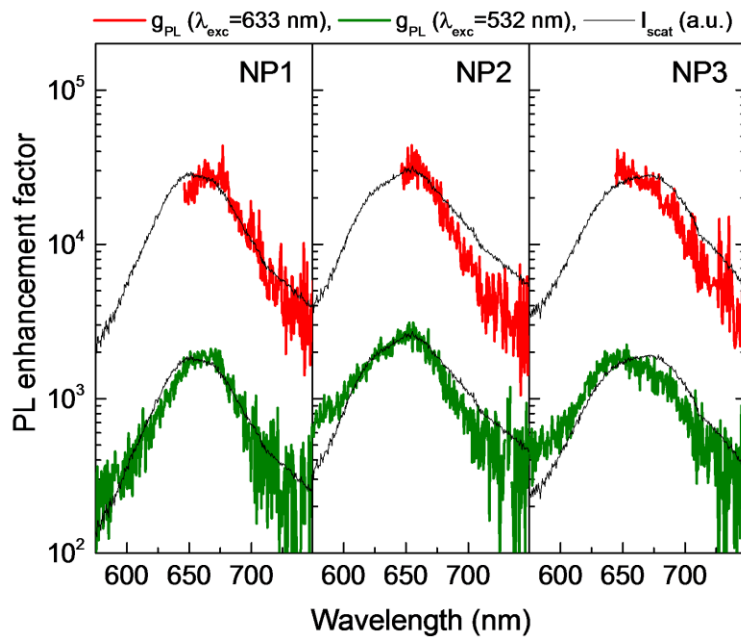


Figure C-3: Photoluminescence enhancement spectra at 532 nm and 633 nm excitation from three different gold nanoparticles on a gold film. The scattering spectrum of these particles are scaled and overlaid to facilitate comparison between scattering and photoluminescence enhancement spectra.

APPENDIX D: SUPPORTING INFORMATION FOR CHAPTER 6

D.1. Microscopy Images from Different Steps of Sample Preparation

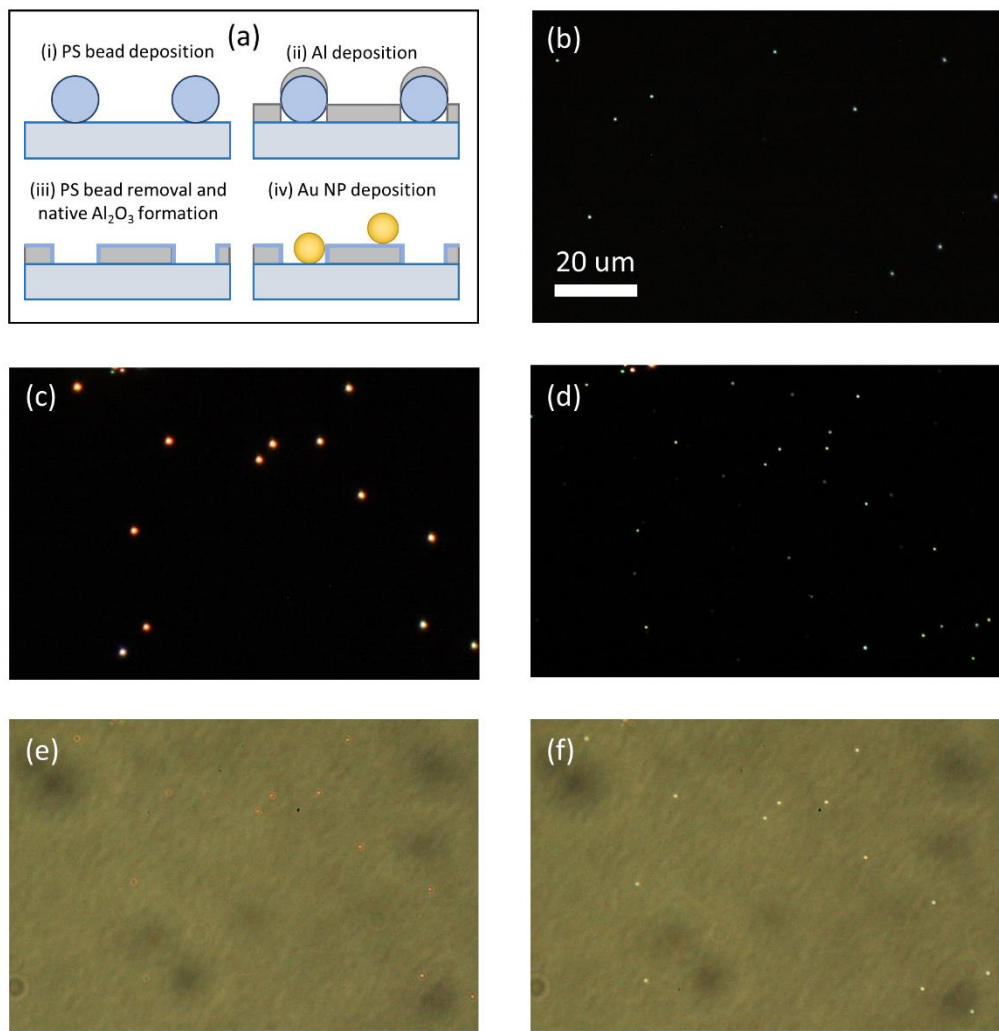


Figure D-1: (a) Fabrication process of the HiO structures using nanosphere lithography. (b) Darkfield microscopy image of the sample after fabrication step (i), showing scattering from polystyrene beads. (c and d) darkfield microscopy images taken from the same sample area after fabrication step (ii) and (iii), respectively. The Al caps in (c) were removed revealing nanoholes in (d). (e and f) Corresponding transmission microscopy images of (c and d).

D.2. Darkfield and SEM Images, Scattering Spectra, and Transmission Spectra of Additional HiO Structures

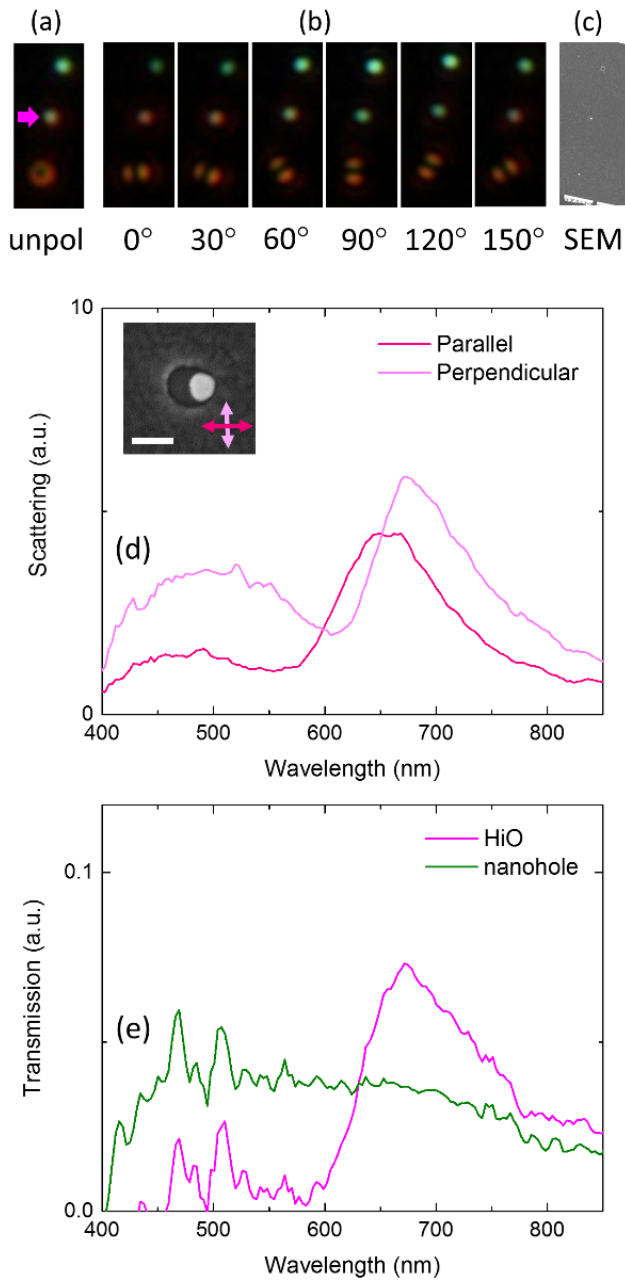


Figure D-2: (a) Darkfield microscopy image of a nanohole (top), a HiO structure (middle, marked by the magenta arrow), and a Au NP (bottom). (b) Darkfield microscopy image of the same structures but with a linear analyzer inserted in the collection path of the microscope. (c) Matching SEM image of the structures. The images in (a–c) are $\sim 2.5 \mu\text{m}$ wide. (d) Scattering spectra of the HiO structure collected at two analyzer angles, indicated respectively by the dark and light magenta double arrows in the SEM image of the HiO structure in the inset. The scale bar in the inset is 100 nm. (e) Transmission spectra of the HiO structure and a nearby nanohole.

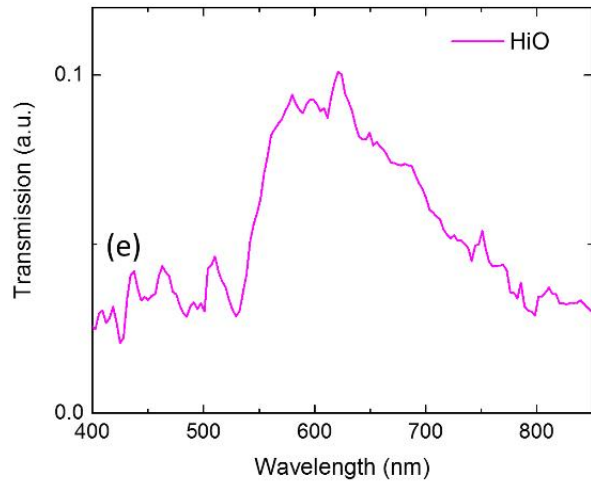
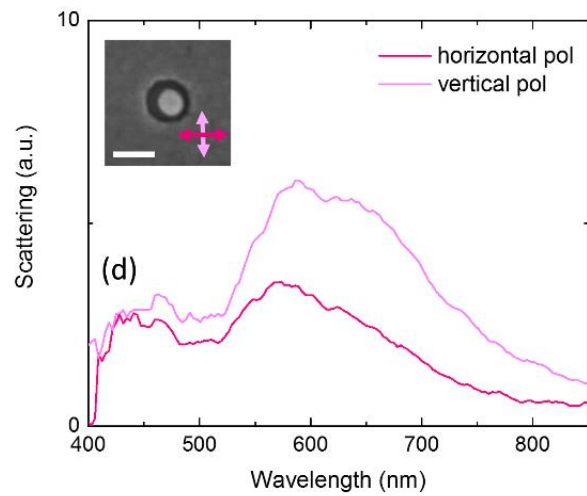
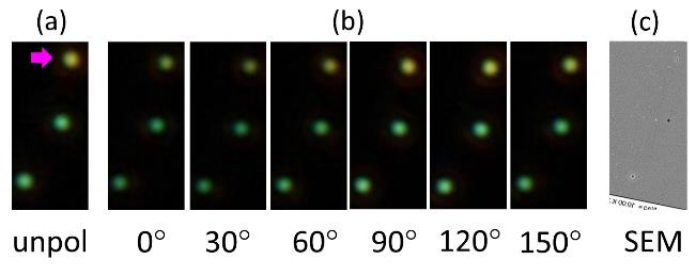


Figure D-3: (a) Darkfield microscopy image of a HiO structure (top, marked by a magenta arrow), and two nanoholes. Unlike most of the HiO structures observed in the experiment, this HiO has dried near the center of the nanohole which results in a different spectral response and relatively weak polarization dependence. (b) Darkfield microscopy image of the same structures but with a linear analyzer inserted in the collection path of the microscope. (c) Matching SEM image of the structures. The images in (a–c) are $\sim 2.5 \mu\text{m}$ wide. (d) Scattering spectra of the HiO structure collected at two analyzer angles, indicated respectively by the dark and light magenta double arrows in the SEM image of the HiO structure in the inset. The scale bar in the inset is 100 nm. (e) Transmission spectra of the HiO structure.

APPENDIX E: LIST OF PUBLICATIONS

- 1) C. Lumdee and P. G. Kik “Omnidirectional Excitation of Sidewall Gap-Plasmons in a hybrid Gold-Aluminum Nanopore Structure”, *submitted*.
- 2) S. Toroghi, C. Lumdee and P. G. Kik “Heterogeneous plasmonic trimers for enhanced nonlinear optical absorption” *Applied Physics Letters* 106 (10), 103102, 2015.
- 3) C. Lumdee, B. Yun, and P. G. Kik “Effect of surface roughness on substrate-tuned gold nanoparticle gap plasmon resonances” *Nanoscale* 7 (9), pp.4250–4255, 2015.
- 4) C. Lumdee, B. Yun, and P. G. Kik “Gap-Plasmon Enhanced Gold Nanoparticle Photoluminescence” *ACS Photonics* 1 (11), pp.1224–1230, 2014.
- 5) C. Lumdee, B. Yun, and P. G. Kik “Wide-band Spectral Control of Au Nanoparticle Plasmon Resonances on a Thermally and Chemically Robust Sensing Platform” *J. Phys. Chem. C* 117 (37), pp.19127–19133, 2013.
- 6) C. Lumdee, S. Toroghi, and P. G. Kik “Post-Fabrication Voltage Controlled Resonance Tuning of Nanoscale Plasmonic Antennas” *ACS Nano* 6 (7), pp.6301–6307, 2012.

REFERENCES

1. Jackson, J.D., *Classical Electrodynamics*. 1962, New York: Wiley.
2. Bohren, C.F. and D.R. Huffman, *Absorption and scattering of light by small particles*. 1983, New York: Wiley. xiv, 530 p.
3. Maier, S.A., *Plasmonics: Fundamentals and Applications*. 2007, New York: Springer.
4. Palik, E.D. and G. Ghosh, *Handbook of Optical Constants of Solids*. 1985, Orlando; London: Academic Press.
5. Ashcroft, N.W. and N.D. Mermin, *Solid state physics*. 1976, Philadelphia, PA: Saunders College. 826 S.
6. Doremus, R.H., *Optical Properties of Small Silver Particles*. Journal of Chemical Physics, 1965. **42**(1): p. 414-&.
7. Link, S. and M.A. El-Sayed, *Size and temperature dependence of the plasmon absorption of colloidal gold nanoparticles*. J. Phys. Chem. B, 1999. **103**(21): p. 4212-4217.
8. Mie, G., *Beiträge zur Optik trüber Medien, speziell kolloidaler Metallösungen*. Annalen der Physik, 1908. **330**(3): p. 377-445.
9. Schopper, H., *Die Untersuchung dünner absorbierender Schichten mit Hilfe der absoluten Phase*. Zeitschrift für Physik A Hadrons and Nuclei, 1951. **130**(5): p. 565-584.
10. Yamaguchi, S., *The Resonance Type Absorption of Very Thin Silver and Gold Films*. Journal of the Physical Society of Japan, 1960. **15**(Copyright (C) 1960 The Physical Society of Japan): p. 1577.

11. Hunderi, O. and H.P. Myers, *Optical-Absorption in Partially Disordered Silver Films*. Journal of Physics F-Metal Physics, 1973. **3**(4): p. 683-690.
12. Meessen, A., *The anomalous infra-red absorption of alkali metals and collective oscillations in small metal particles*. J. Phys. France, 1972. **33**(4): p. 371-381.
13. Selby, K., et al., *Surface Plasma Resonances in Free Metal-Clusters*. Physical Review B, 1989. **40**(8): p. 5417-5427.
14. Felidj, N., et al., *Optimized Surface-Enhanced Raman Scattering on Gold Nanoparticle Arrays*. Applied Physics Letters, 2003. **82**(18): p. 3095-3097.
15. Kuwata, H., et al., *Resonant light scattering from metal nanoparticles: Practical analysis beyond Rayleigh approximation*. Applied Physics Letters, 2003. **83**(22): p. 4625-4627.
16. Anderson, L.J.E., et al., *A Tunable Plasmon Resonance in Gold Nanobelts*. Nano Letters, 2011. **11**(11): p. 5034-5037.
17. Hulteen, J.C. and R.P. Vanduyne, *Nanosphere Lithography - a Materials General Fabrication Process for Periodic Particle Array Surfaces*. Journal of Vacuum Science & Technology a-Vacuum Surfaces and Films, 1995. **13**(3): p. 1553-1558.
18. Im, S.H., et al., *Large-scale synthesis of silver nanocubes: The role of HCl in promoting cube perfection and monodispersity*. Angewandte Chemie-International Edition, 2005. **44**(14): p. 2154-2157.
19. Sherry, L.J., et al., *Localized surface plasmon resonance spectroscopy of single silver nanocubes*. Nano Letters, 2005. **5**(10): p. 2034-2038.

20. Averitt, R.D., D. Sarkar, and N.J. Halas, *Plasmon resonance shifts of Au-coated Au₂S nanoshells: Insight into multicomponent nanoparticle growth*. Physical Review Letters, 1997. **78**(22): p. 4217-4220.
21. Halas, N.J., *Playing with plasmons. Tuning the optical resonant properties of metallic nanoshells*. Mrs Bulletin, 2005. **30**(5): p. 362-367.
22. McMahon, J.M., et al., *Gold nanoparticle dimer plasmonics: finite element method calculations of the electromagnetic enhancement to surface-enhanced Raman spectroscopy*. Analytical and Bioanalytical Chemistry, 2009. **394**(7): p. 1819-1825.
23. Genov, D.A., et al., *Resonant field enhancements from metal nanoparticle arrays*. Nano Letters, 2004. **4**(1): p. 153-158.
24. Oubre, C. and P. Nordlander, *Finite-difference time-domain studies of the optical properties of nanoshell dimers*. Journal of Physical Chemistry B, 2005. **109**(20): p. 10042-10051.
25. Li, W.Y., et al., *Dimers of Silver Nanospheres: Facile Synthesis and Their Use as Hot Spots for Surface-Enhanced Raman Scattering*. Nano Letters, 2009. **9**(1): p. 485-490.
26. Lamprecht, B., et al., *Metal nanoparticle gratings: Influence of dipolar particle interaction on the plasmon resonance*. Physical Review Letters, 2000. **84**(20): p. 4721-4724.
27. Meier, M., A. Wokaun, and P.F. Liao, *Enhanced Fields on Rough Surfaces - Dipolar Interactions among Particles of Sizes Exceeding the Rayleigh Limit*. Journal of the Optical Society of America B-Optical Physics, 1985. **2**(6): p. 931-949.
28. Maier, S.A., et al., *Observation of near-field coupling in metal nanoparticle chains using far-field polarization spectroscopy*. Physical Review B, 2002. **65**(19).

29. *CST MICROWAVE STUDIO®*, Computer Simulation Technology, Darmstadt, Germany.
30. Zhao, L.L., K.L. Kelly, and G.C. Schatz, *The extinction spectra of silver nanoparticle arrays: Influence of array structure on plasmon resonance wavelength and width*. Journal of Physical Chemistry B, 2003. **107**(30): p. 7343-7350.
31. Su, K.H., et al., *Interparticle coupling effects on plasmon resonances of nanogold particles*. Nano Letters, 2003. **3**(8): p. 1087-1090.
32. Nordlander, P., et al., *Plasmon hybridizaton in nanoparticle dimers*. Nano Letters, 2004. **4**(5): p. 899-903.
33. Alonso-Gonzalez, P., et al., *Real-Space Mapping of Fano Interference in Plasmonic Metamolecules*. Nano Letters, 2011. **11**(9): p. 3922-3926.
34. Frimmer, M., T. Coenen, and A.F. Koenderink, *Signature of a Fano Resonance in a Plasmonic Metamolecule's Local Density of Optical States*. Physical Review Letters, 2012. **108**(7).
35. Zhang, S., et al., *Plasmon-induced transparency in metamaterials*. Physical Review Letters, 2008. **101**(4).
36. Liu, N., et al., *Plasmonic analogue of electromagnetically induced transparency at the Drude damping limit*. Nature Materials, 2009. **8**(9): p. 758-762.
37. Antoniewicz, P.R., *Effective Polarizability of a Point Dipole near a Metal Surface with a Thomas-Fermi Response*. Journal of Chemical Physics, 1972. **56**(4): p. 1711-1714.
38. Takemori, T., M. Inoue, and K. Ohtaka, *Optical-Response of a Sphere Coupled to a Metal-Substrate*. Journal of the Physical Society of Japan, 1987. **56**(4): p. 1587-1602.

39. Ruppin, R., *Optical-Absorption by a Small Sphere above a Substrate with Inclusion of Nonlocal Effects*. Physical Review B, 1992. **45**(19): p. 11209-11215.
40. Sonnichsen, C., et al., *Spectroscopy of single metallic nanoparticles using total internal reflection microscopy*. Applied Physics Letters, 2000. **77**(19): p. 2949-2951.
41. Jiang, G.Q., et al., *Signal Enhancement and Tuning of Surface Plasmon Resonance in Au Nanoparticle/Polyelectrolyte Ultrathin Films*. Journal of Physical Chemistry C, 2007. **111**(50): p. 18687-18694.
42. Mock, J.J., et al., *Distance-Dependent Plasmon Resonant Coupling between a Gold Nanoparticle and Gold Film*. Nano Lett., 2008. **8**(8): p. 2245-2252.
43. Knight, M.W., et al., *Substrates Matter: Influence of an Adjacent Dielectric on an Individual Plasmonic Nanoparticle*. Nano Letters, 2009. **9**(5): p. 2188-2192.
44. Vernon, K.C., et al., *Influence of Particle-Substrate Interaction on Localized Plasmon Resonances*. Nano Letters, 2010. **10**(6): p. 2080-2086.
45. Du, C.L., et al., *Near-Field Coupling Effect between Individual Au Nanospheres and their Supporting SiO₂/Si Substrate*. Plasmonics, 2010. **5**(2): p. 105-109.
46. Hu, M., et al., *Single Particle Spectroscopy Study of Metal-Film-Induced Tuning of Silver Nanoparticle Plasmon Resonances*. Journal of Physical Chemistry C, 2010. **114**(16): p. 7509-7514.
47. Okamoto, T. and I. Yamaguchi, *Optical Absorption Study of the Surface Plasmon Resonance in Gold Nanoparticles Immobilized onto a Gold Substrate by Self-Assembly Technique*. Journal of Physical Chemistry B, 2003. **107**(38): p. 10321-10324.

48. Pinchuk, A., et al., *Substrate Effect on the Optical Response of Silver Nanoparticles*. Nanotechnology, 2004. **15**(12): p. 1890-1896.
49. Beams, R., et al., *Nanoscale Fluorescence Lifetime Imaging of an Optical Antenna with a Single Diamond NV Center*. Nano Letters, 2013. **13**(8): p. 3807-3811.
50. Pfeiffer, M., et al., *Enhancing the Optical Excitation Efficiency of a Single Self-Assembled Quantum Dot with a Plasmonic Nanoantenna*. Nano Letters, 2010. **10**(11): p. 4555-4558.
51. Fu, Y., J. Zhang, and J.R. Lakowicz, *Plasmon-Enhanced Fluorescence from Single Fluorophores End-Linked to Gold Nanorods*. Journal of the American Chemical Society, 2010. **132**(16): p. 5540-+.
52. Kneipp, K., et al., *Single molecule detection using surface-enhanced Raman scattering (SERS)*. Physical Review Letters, 1997. **78**(9): p. 1667-1670.
53. Nie, S.M. and S.R. Emery, *Probing single molecules and single nanoparticles by surface-enhanced Raman scattering*. Science, 1997. **275**(5303): p. 1102-1106.
54. Fleischmann, M., P.J. Hendra, and Mcquilla.Aj, *Raman-Spectra of Pyridine Adsorbed at a Silver Electrode*. Chemical Physics Letters, 1974. **26**(2): p. 163-166.
55. Jeanmaire, D.L. and R.P. Vanduyne, *Surface Raman Spectroelectrochemistry .1. Heterocyclic, Aromatic, and Aliphatic-Amines Adsorbed on Anodized Silver Electrode*. Journal of Electroanalytical Chemistry, 1977. **84**(1): p. 1-20.
56. Schlücker, S., *Surface enhanced Raman spectroscopy : analytical, biophysical and life science applications*. 2011, Weinheim, Germany: Wiley-VCH. xxii, 331 p.

57. Schwartzberg, A.M., et al., *Unique gold nanoparticle aggregates as a highly active surface-enhanced Raman scattering substrate*. Journal of Physical Chemistry B, 2004. **108**(50): p. 19191-19197.
58. Jackson, J.B. and N.J. Halas, *Surface-Enhanced Raman Scattering on Tunable Plasmonic Nanoparticle Substrates*. Proceedings of the National Academy of Sciences of the United States of America, 2004. **101**(52): p. 17930-17935.
59. Inoue, M. and K. Ohtaka, *Surface Enhanced Raman Scattering by Metal Spheres. I. Cluster Effect*. Journal of the Physical Society of Japan, 1983. **52**(Copyright (C) 1983 The Physical Society of Japan): p. 3853.
60. Banaee, M.G. and K.B. Crozier, *Gold nanorings as substrates for surface-enhanced Raman scattering*. Optics Letters, 2010. **35**(5): p. 760-762.
61. Kumar, J. and K.G. Thomas, *Surface-Enhanced Raman Spectroscopy: Investigations at the Nanorod Edges and Dimer Junctions*. Journal of Physical Chemistry Letters, 2011. **2**(6): p. 610-615.
62. Rycenga, M., et al., *Understanding the SERS Effects of Single Silver Nanoparticles and Their Dimers, One at a Time*. Journal of Physical Chemistry Letters, 2010. **1**(4): p. 696-703.
63. Xu, H. and M. Kall, *Polarization-dependent surface-enhanced Raman spectroscopy of isolated silver nanoaggregates*. Chemphyschem, 2003. **4**(9): p. 1001-5.
64. Etchegoin, P.G., C. Galloway, and E.C. Le Ru, *Polarization-dependent effects in surface-enhanced Raman scattering (SERS)*. Physical Chemistry Chemical Physics, 2006. **8**(22): p. 2624-2628.

65. Tian, Z.Q., et al., *Surface-enhanced Raman scattering from transition metals with special surface morphology and nanoparticle shape*. Faraday Discussions, 2006. **132**: p. 159-170.
66. Hill, R.T., et al., *Leveraging Nanoscale Plasmonic Modes to Achieve Reproducible Enhancement of Light*. Nano Letters, 2010. **10**(10): p. 4150-4154.
67. Zheng, J.W., et al., *Surface-enhanced Raman scattering of 4-aminothiophenol in assemblies of nanosized particles and the macroscopic surface of silver*. Langmuir, 2003. **19**(3): p. 632-636.
68. Orendorff, C.J., et al., *Surface-enhanced Raman spectroscopy of self-assembled monolayers: sandwich architecture and nanoparticle shape dependence*. Analytical Chemistry, 2005. **77**(10): p. 3261-6.
69. Lee, W., et al., *Self-Assembled SERS Substrates with Tunable Surface Plasmon Resonances*. Advanced Functional Materials, 2011. **21**(18): p. 3424-3429.
70. Mooradian, A., *Photoluminescence of Metals*. Physical Review Letters, 1969. **22**(5): p. 185-187.
71. Wilcoxon, J.P., et al., *Photoluminescence from nanosize gold clusters*. Journal of Chemical Physics, 1998. **108**(21): p. 9137-9143.
72. Mohamed, M.B., et al., *The 'lightning' gold nanorods: fluorescence enhancement of over a million compared to the gold metal*. Chemical Physics Letters, 2000. **317**(6): p. 517-523.
73. Varnavski, O.P., et al., *Relative enhancement of ultrafast emission in gold nanorods*. Journal of Physical Chemistry B, 2003. **107**(14): p. 3101-3104.
74. Dulkeith, E., et al., *Plasmon emission in photoexcited gold nanoparticles*. Physical Review B, 2004. **70**(20): p. 205424.

75. Varnavski, O.P., et al., *Femtosecond excitation dynamics in gold nanospheres and nanorods*. Physical Review B, 2005. **72**(23): p. 235405.
76. Brongersma, M.L., N.J. Halas, and P. Nordlander, *Plasmon-induced hot carrier science and technology*. Nature Nanotechnology, 2015. **10**(1): p. 25-34.
77. Clavero, C., *Plasmon-induced hot-electron generation at nanoparticle/metal-oxide interfaces for photovoltaic and photocatalytic devices*. Nature Photonics, 2014. **8**(2): p. 95-103.
78. Knight, M.W., et al., *Photodetection with Active Optical Antennas*. Science, 2011. **332**(6030): p. 702-704.
79. Zhou, X.M., et al., *Surface plasmon resonance-mediated photocatalysis by noble metal-based composites under visible light*. Journal of Materials Chemistry, 2012. **22**(40): p. 21337-21354.
80. Hou, W.B. and S.B. Cronin, *A Review of Surface Plasmon Resonance-Enhanced Photocatalysis*. Advanced Functional Materials, 2013. **23**(13): p. 1612-1619.
81. Long, R., et al., *Coupling Solar Energy into Reactions: Materials Design for Surface Plasmon-Mediated Catalysis*. Small, 2015.
82. Ding, I.K., et al., *Plasmonic Dye-Sensitized Solar Cells*. Advanced Energy Materials, 2011. **1**(1): p. 52-57.
83. Sheehan, S.W., et al., *Plasmonic Enhancement of Dye-Sensitized Solar Cells Using Core-Shell-Shell Nanostructures*. Journal of Physical Chemistry C, 2013. **117**(2): p. 927-934.
84. Jang, Y.H., et al., *Plasmonic dye-sensitized solar cells incorporated with Au-TiO₂ nanostructures with tailored configurations*. Nanoscale, 2014. **6**(3): p. 1823-1832.

85. Thomann, I., et al., *Plasmon Enhanced Solar-to-Fuel Energy Conversion*. Nano Letters, 2011. **11**(8): p. 3440-3446.
86. Liu, Z.W., et al., *Plasmon Resonant Enhancement of Photocatalytic Water Splitting Under Visible Illumination*. Nano Letters, 2011. **11**(3): p. 1111-1116.
87. Silva, C.G., et al., *Influence of Excitation Wavelength (UV or Visible Light) on the Photocatalytic Activity of Titania Containing Gold Nanoparticles for the Generation of Hydrogen or Oxygen from Water*. Journal of the American Chemical Society, 2011. **133**(3): p. 595-602.
88. Xu, P., et al., *Mechanistic understanding of surface plasmon assisted catalysis on a single particle: cyclic redox of 4-aminothiophenol*. Scientific Reports, 2013. **3**.
89. Su, R., et al., *Designer Titania-Supported Au-Pd Nanoparticles for Efficient Photocatalytic Hydrogen Production*. Acs Nano, 2014. **8**(4): p. 3490-3497.
90. Honda, M., et al., *Plasmon-enhanced UV photocatalysis*. Applied Physics Letters, 2014. **104**(6).
91. Mukherjee, S., et al., *Hot-Electron-Induced Dissociation of H-2 on Gold Nanoparticles Supported on SiO2*. Journal of the American Chemical Society, 2014. **136**(1): p. 64-67.
92. Zhang, X.M., et al., *Plasmonic photocatalysis*. Reports on Progress in Physics, 2013. **76**(4).
93. Kohlgraf-Owens, D.C. and P.G. Kik, *Structural Control of Nonlinear Optical Absorption and Refraction in Dense Metal Nanoparticle Arrays*. Optics Express, 2009. **17**(17): p. 15032-15042.

94. Toroghi, S. and P.G. Kik, *Cascaded Plasmonic Metamaterials for Phase-Controlled Enhancement of Nonlinear Absorption and Refraction*. Physical Review B, 2012. **85**(4): p. 045432.
95. Moran, A.M., et al., *Second Harmonic Excitation Spectroscopy of Silver Nanoparticle Arrays*. Journal of Physical Chemistry B, 2005. **109**(10): p. 4501-4506.
96. Palomba, S., M. Danckwerts, and L. Novotny, *Nonlinear Plasmonics with Gold Nanoparticle Antennas*. Journal of Optics a-Pure and Applied Optics, 2009. **11**(11).
97. Utikal, T., et al., *Towards the Origin of the Nonlinear Response in Hybrid Plasmonic Systems*. Physical Review Letters, 2011. **106**(13).
98. Sperling, R.A., et al., *Biological Applications of Gold Nanoparticles*. Chemical Society Reviews, 2008. **37**(9): p. 1896-1908.
99. Willets, K.A. and R.P. Van Duyne, *Localized Surface Plasmon Resonance Spectroscopy and Sensing*. Annual Review of Physical Chemistry, 2007. **58**: p. 267-297.
100. Word, R.C., T. Dornan, and R. Konenkamp, *Photoemission from Localized Surface Plasmons in Fractal Metal Nanostructures*. Applied Physics Letters, 2010. **96**(25).
101. Wang, F.M. and N.A. Melosh, *Plasmonic Energy Collection through Hot Carrier Extraction*. Nano Letters, 2011. **11**(12): p. 5426-5430.
102. Pillai, S., et al., *Surface plasmon enhanced silicon solar cells*. Journal of Applied Physics, 2007. **101**(9).
103. Atwater, H.A. and A. Polman, *Plasmonics for improved photovoltaic devices*. Nature Materials, 2010. **9**(3): p. 205-213.

104. Chan, G.H., et al., *Localized surface plasmon resonance spectroscopy of triangular aluminum nanoparticles*. Journal of Physical Chemistry C, 2008. **112**(36): p. 13958-13963.
105. Noguez, C., *Surface Plasmons on Metal Nanoparticles: The Influence of Shape and Physical Environment*. Journal of Physical Chemistry C, 2007. **111**(10): p. 3806-3819.
106. Kuhn, H., *Classical Aspects of Energy Transfer in Molecular Systems*. Journal of Chemical Physics, 1970. **53**(1): p. 101-108.
107. Stuart, H.R. and D.G. Hall, *Enhanced Dipole-Dipole Interaction between Elementary Radiators near a Surface*. Physical Review Letters, 1998. **80**(25): p. 5663-5666.
108. Murray, W.A., J.R. Suckling, and W.L. Barnes, *Overlayers on Silver Nanotriangles: Field Confinement and Spectral Position of Localized Surface Plasmon Resonances*. Nano Letters, 2006. **6**(8): p. 1772-1777.
109. Chen, S.Y., et al., *Gold Nanoparticles on Polarizable Surfaces as Raman Scattering Antennas*. Acs Nano, 2010. **4**(11): p. 6535-6546.
110. Diggle, J.W., T.C. Downie, and C.W. Goulding, *Anodic Oxide Films on Aluminum*. Chemical Reviews, 1969. **69**(3): p. 365-405.
111. Campbell, T., et al., *Dynamics of Oxidation of Aluminum Nanoclusters using Variable Charge Molecular-Dynamics Simulations on Parallel Computers*. Physical Review Letters, 1999. **82**(24): p. 4866-4869.
112. Langhammer, C., et al., *Localized Surface Plasmon Resonances in Aluminum Nanodisks*. Nano Letters, 2008. **8**(5): p. 1461-1471.

113. Hutchins, G.A. and C.T. Chen, *The Amorphous to Crystalline Transformation of Anodic Aluminum-Oxide during Anodization in an Ammonium Citrate Electrolyte*. Journal of the Electrochemical Society, 1986. **133**(7): p. 1332-1337.
114. Lichtenstein, T., *Handbook of Thin Film Materials*. 1979, Rochester, New York.
115. Johnson, P.B. and R.W. Christy, *Optical Constants of the Noble Metals*. Phys. Rev. B, 1972. **6**(12): p. 4370-4379.
116. Haynes, C.L. and R.P. Van Duyne, *Plasmon-sampled surface-enhanced Raman excitation spectroscopy*. Journal of Physical Chemistry B, 2003. **107**(30): p. 7426-7433.
117. Haes, A.J. and R.P. Van Duyne, *A Nanoscale Optical Biosensor: Sensitivity and Selectivity of an Approach based on the Localized Surface Plasmon Resonance Spectroscopy of Triangular Silver Nanoparticles*. Journal of the American Chemical Society, 2002. **124**(35): p. 10596-604.
118. Lal, S., et al., *Light Interaction between Gold Nanoshells Plasmon Resonance and Planar Optical Waveguides*. Journal of Physical Chemistry B, 2002. **106**(22): p. 5609-5612.
119. Xia, Y.N. and N.J. Halas, *Shape-controlled synthesis and surface plasmonic properties of metallic nanostructures*. Mrs Bulletin, 2005. **30**(5): p. 338-344.
120. Elechiguerra, J.L., J. Reyes-Gasga, and M.J. Yacaman, *The role of twinning in shape evolution of anisotropic noble metal nanostructures*. Journal of Materials Chemistry, 2006. **16**(40): p. 3906-3919.
121. Qin, L.D., et al., *On-wire lithography*. Science, 2005. **309**(5731): p. 113-115.

122. Osberg, K.D., et al., *Dispersible Gold Nanorod Dimers with Sub-5 nm Gaps as Local Amplifiers for Surface-Enhanced Raman Scattering*. Nano Letters, 2012. **12**(7): p. 3828-3832.
123. Haynes, C.L. and R.P. Van Duyne, *Nanosphere lithography: A versatile nanofabrication tool for studies of size-dependent nanoparticle optics*. Journal of Physical Chemistry B, 2001. **105**(24): p. 5599-5611.
124. Tran, M.L., et al., *Control of Surface Plasmon Localization via Self-Assembly of Silver Nanoparticles along Silver Nanowires*. Journal of the American Chemical Society, 2008. **130**(51): p. 17240-17241.
125. Lim, D.K., et al., *Nanogap-engineerable Raman-active nanodumbbells for single-molecule detection*. Nature Materials, 2010. **9**(1): p. 60-67.
126. Nordlander, P. and E. Prodan, *Plasmon hybridization in nanoparticles near metallic surfaces*. Nano Letters, 2004. **4**(11): p. 2209-2213.
127. Lei, D.Y., et al., *Revealing Plasmonic Gap Modes in Particle-on-Film Systems Using Dark-Field Spectroscopy*. Acs Nano, 2012. **6**(2): p. 1380-1386.
128. Mubeen, S., et al., *Plasmonic Properties of Gold Nanoparticles Separated from a Gold Mirror by an Ultrathin Oxide*. Nano Lett., 2012. **12**(4): p. 2088-2094.
129. Le, F., et al., *Plasmons in the metallic nanoparticle - Film system as a tunable impurity problem*. Nano Letters, 2005. **5**(10): p. 2009-2013.
130. Lumdee, C., S. Toroghi, and P.G. Kik, *Post-fabrication Voltage Controlled Resonance Tuning of Nanoscale Plasmonic Antennas*. Acs Nano, 2012. **6**(7): p. 6301-6307.

131. Mock, J.J., et al., *Probing Dynamically Tunable Localized Surface Plasmon Resonances of Film-Coupled Nanoparticles by Evanescent Wave Excitation*. Nano Lett., 2012. **12**(4): p. 1757-1764.
132. Muskens, O.L., et al., *Strong enhancement of the radiative decay rate of emitters by single plasmonic nanoantennas*. Nano Letters, 2007. **7**(9): p. 2871-2875.
133. Bek, A., et al., *Fluorescence enhancement in hot spots of AFM-designed gold nanoparticle sandwiches*. Nano Letters, 2008. **8**(2): p. 485-490.
134. Fu, Y., J. Zhang, and J.R. Lakowicz, *Largely Enhanced Single-Molecule Fluorescence in Plasmonic Nanogaps Formed by Hybrid Silver Nanostructures*. Langmuir, 2013. **29**(8): p. 2731-2738.
135. Gulbransen, E.A. and W.S. Wysong, *Thin oxide films on aluminum*. J Phys Colloid Chem, 1947. **51**(5): p. 1087-1103.
136. Chen, H.J., et al., *Effect of the Dielectric Properties of Substrates on the Scattering Patterns of Gold Nanorods*. Acs Nano, 2011. **5**(6): p. 4865-4877.
137. King, N.S., et al., *Angle- and Spectral-Dependent Light Scattering from Plasmonic Nanocups*. Acs Nano, 2011. **5**(9): p. 7254-7262.
138. David, C. and F.J.G. de Abajo, *Spatial Nonlocality in the Optical Response of Metal Nanoparticles*. Journal of Physical Chemistry C, 2011. **115**(40): p. 19470-19475.
139. Ciraci, C., et al., *Probing the Ultimate Limits of Plasmonic Enhancement*. Science, 2012. **337**(6098): p. 1072-1074.
140. Stiles, P.L., et al., *Surface-Enhanced Raman Spectroscopy*. Annual Review of Analytical Chemistry, 2008. **1**: p. 601-626.

141. Le Ru, E.C. and P.G. Etchegoin, *Rigorous justification of the [E](4) enhancement factor in Surface Enhanced Raman Spectroscopy*. Chemical Physics Letters, 2006. **423**(1-3): p. 63-66.
142. de Abajo, F.J.G., *Nonlocal Effects in the Plasmons of Strongly Interacting Nanoparticles, Dimers, and Waveguides*. Journal of Physical Chemistry C, 2008. **112**(46): p. 17983-17987.
143. Mao, L., et al., *Effects of quantum tunneling in metal nanogap on surface-enhanced Raman scattering*. Applied Physics Letters, 2009. **94**(24): p. 243102.1-243102.3.
144. Zuloaga, J., E. Prodan, and P. Nordlander, *Quantum Description of the Plasmon Resonances of a Nanoparticle Dimer*. Nano Letters, 2009. **9**(2): p. 887-891.
145. Esteban, R., et al., *Bridging quantum and classical plasmonics with a quantum-corrected model*. Nature Communications, 2012. **3**: p. 825.1-825.9.
146. Kuhlicke, A., et al., *In Situ Observation of Plasmon Tuning in a Single Gold Nanoparticle during Controlled Melting*. Nano Letters, 2013. **13**(5): p. 2041-2046.
147. Li, L., et al., *Single molecule SERS and detection of biomolecules with a single gold nanoparticle on a mirror junction*. Analyst, 2013. **138**(16): p. 4574-4578.
148. Lumdee, C., B. Yun, and P.G. Kik, *Wide-Band Spectral Control of Au Nanoparticle Plasmon Resonances on a Thermally and Chemically Robust Sensing Platform*. J. Phys. Chem. C, 2013. **117**(37): p. 19127-19133.
149. Lee, K.S. and M.A. El-Sayed, *Gold and silver nanoparticles in sensing and imaging: Sensitivity of plasmon response to size, shape, and metal composition*. J. Phys. Chem. B, 2006. **110**(39): p. 19220-19225.

150. Mock, J.J., et al., *Shape effects in plasmon resonance of individual colloidal silver nanoparticles*. J. Chem. Phys., 2002. **116**(15): p. 6755-6759.
151. Kossyrev, P.A., et al., *Electric field tuning of plasmonic response of nanodot array in liquid crystal matrix*. Nano Letters, 2005. **5**(10): p. 1978-1981.
152. Hajisalem, G., et al., *Effect of surface roughness on self-assembled monolayer plasmonic ruler in nonlocal regime*. Optics Express, 2014. **22**(8): p. 9604-9610.
153. Sauer, G., G. Brehm, and S. Schneider, *Preparation of SERS-active gold film electrodes via electrocrystallization: their characterization and application with NIR excitation*. J. Raman Spectrosc., 2004. **35**(7): p. 568-576.
154. Khan, M.A., T.P. Hogan, and B. Shanker, *Surface-enhanced Raman scattering from gold-coated germanium oxide nanowires*. J. Raman Spectrosc., 2008. **39**(7): p. 893-900.
155. Ulman, A., *Formation and structure of self-assembled monolayers*. Chem. Rev., 1996. **96**(4): p. 1533-1554.
156. Hegner, M., P. Wagner, and G. Semenza, *Ultralarge Atomically Flat Template-Stripped Au Surfaces for Scanning Probe Microscopy*. Surf. Sci., 1993. **291**(1-2): p. 39-46.
157. Huang, J.S., et al., *Atomically flat single-crystalline gold nanostructures for plasmonic nanocircuitry*. Nat. Commun., 2010. **1**.
158. Boyd, G.T., Z.H. Yu, and Y.R. Shen, *Photoinduced Luminescence from the Noble-Metals and Its Enhancement on Roughened Surfaces*. Physical Review B, 1986. **33**(12): p. 7923-7936.

159. Beversluis, M.R., A. Bouhelier, and L. Novotny, *Continuum generation from single gold nanostructures through near-field mediated intraband transitions*. Physical Review B, 2003. **68**(11): p. 115433.
160. Bouhelier, A., et al., *Surface plasmon characteristics of tunable photoluminescence in single gold nanorods*. Physical Review Letters, 2005. **95**(26): p. 267405.
161. Steiner, M., et al., *Plasmon-enhanced emission in gold nanoparticle aggregates*. Journal of Physical Chemistry C, 2008. **112**(8): p. 3103-3108.
162. Fang, Y., et al., *Plasmon Emission Quantum Yield of Single Gold Nanorods as a Function of Aspect Ratio*. Acs Nano, 2012. **6**(8): p. 7177-7184.
163. Hu, H.L., et al., *Plasmon-Modulated Photoluminescence of Individual Gold Nanostructures*. Acs Nano, 2012. **6**(11): p. 10147-10155.
164. Tcherniak, A., et al., *One-Photon Plasmon Luminescence and Its Application to Correlation Spectroscopy as a Probe for Rotational and Translational Dynamics of Gold Nanorods*. Journal of Physical Chemistry C, 2011. **115**(32): p. 15938-15949.
165. Yorulmaz, M., et al., *Luminescence Quantum Yield of Single Gold Nanorods*. Nano Letters, 2012. **12**(8): p. 4385-4391.
166. Shahbazyan, T.V., *Theory of Plasmon-Enhanced Metal Photoluminescence*. Nano Letters, 2013. **13**(1): p. 194-198.
167. Tittl, A., et al., *Plasmonic smart dust for probing local chemical reactions*. Nano Letters, 2013. **13**(4): p. 1816-1821.

168. Christopher, P., et al., *Singular characteristics and unique chemical bond activation mechanisms of photocatalytic reactions on plasmonic nanostructures*. Nature Materials, 2012. **11**(12): p. 1044-1050.
169. Ciraci, C., et al., *Film-coupled nanoparticles by atomic layer deposition: Comparison with organic spacing layers*. Applied Physics Letters, 2014. **104**(2): p. 023109.
170. Landau, L., *On the vibration of the electronic plasma*. J. Phys. USSR, 1946. **10**: p. 25-34.
171. Apell, P., R. Monreal, and S. Lundqvist, *Photoluminescence of Noble-Metals*. Physica Scripta, 1988. **38**(2): p. 174-179.
172. Romaniello, P. and P.L. de Boeij, *The role of relativity in the optical response of gold within the time-dependent current-density-functional theory*. Journal of Chemical Physics, 2005. **122**(16): p. 164303.
173. Kubo, W. and S. Fujikawa, *Au Double Nanopillars with Nanogap for Plasmonic Sensor*. Nano Letters, 2011. **11**(1): p. 8-15.
174. Hoffmann, J.M., et al., *Enhanced infrared spectroscopy using small-gap antennas prepared with two-step evaporation nanosphere lithography*. Optics Express, 2014. **22**(12): p. 14425-14432.
175. Mann, S.A. and E.C. Garnett, *Resonant Nanophotonic Spectrum Splitting for Ultrathin Multijunction Solar Cells*. Acs Photonics, 2015. **2**(7): p. 816-821.
176. Park, H.I., et al., *High Performance Organic Photovoltaics with Plasmonic-Coupled Metal Nanoparticle Clusters*. Acs Nano, 2014. **8**(10): p. 10305-10312.

177. Mahmoud, M.A. and M.A. El-Sayed, *Enhancing Catalytic Efficiency of Hollow Palladium Nanoparticles by Photothermal Heating of Gold Nanoparticles Added to the Cavity: Palladium-Gold Nanorattles*. *Chemcatchem*, 2014. **6**(12): p. 3540-3546.
178. Oulton, R.F., et al., *Plasmon lasers at deep subwavelength scale*. *Nature*, 2009. **461**(7264): p. 629-632.
179. Lu, Y.J., et al., *All-Color Plasmonic Nanolasers with Ultralow Thresholds: Autotuning Mechanism for Single-Mode Lasing*. *Nano Letters*, 2014. **14**(8): p. 4381-4388.
180. Ding, T., et al., *Controllable Tuning Plasmonic Coupling with Nanoscale Oxidation*. *Acs Nano*, 2015. **9**(6): p. 6110-6118.
181. Wei, H., et al., *Individual nanometer hole-particle pairs for surface-enhanced Raman scattering*. *Small*, 2008. **4**(9): p. 1296-1300.
182. Jahr, N., et al., *Spectroscopy on Single Metallic Nanoparticles Using Subwavelength Apertures*. *Journal of Physical Chemistry C*, 2013. **117**(15): p. 7751-7756.
183. Cecchini, M.P., et al., *Rapid Ultrasensitive Single Particle Surface-Enhanced Raman Spectroscopy Using Metallic Nanopores*. *Nano Letters*, 2013. **13**(10): p. 4602-4609.
184. Lumdee, C., B.F. Yun, and P.G. Kik, *Gap-Plasmon Enhanced Gold Nanoparticle Photoluminescence*. *Acs Photonics*, 2014. **1**(11): p. 1224-1230.
185. Cui, Y., et al., *Integration of colloidal nanocrystals into lithographically patterned devices*. *Nano Letters*, 2004. **4**(6): p. 1093-1098.
186. Fan, J.A., et al., *Plasmonic Mode Engineering with Templated Self-Assembled Nanoclusters*. *Nano Letters*, 2012. **12**(10): p. 5318-5324.

187. Levene, M.J., et al., *Zero-mode waveguides for single-molecule analysis at high concentrations*. Science, 2003. **299**(5607): p. 682-686.
188. Samiee, K.T., et al., *Zero mode waveguides for single-molecule spectroscopy on lipid membranes*. Biophysical Journal, 2006. **90**(9): p. 3288-3299.
189. Moran-Mirabal, J.M. and H.G. Craighead, *Zero-mode waveguides: Sub-wavelength nanostructures for single molecule studies at high concentrations*. Methods, 2008. **46**(1): p. 11-17.
190. Larkin, J., et al., *Reversible Positioning of Single Molecules inside Zero-Mode Waveguides*. Nano Letters, 2014. **14**(10): p. 6023-6029.
191. Brolo, A.G., et al., *Nanohole-enhanced Raman scattering*. Nano Letters, 2004. **4**(10): p. 2015-2018.
192. Nie, B., C.L. He, and L.J. Liu, *Surface-enhanced Raman scattering within silver-nanoparticle-decorated nanometric apertures*. Journal of Raman Spectroscopy, 2013. **44**(11): p. 1512-1517.